
NUMERICAL SIMULATIONS OF FILAMENTARY CLOUDS

Seamus D. C. H. Clarke

A THESIS SUBMITTED TO
CARDIFF UNIVERSITY
FOR THE DEGREE OF
DOCTOR OF PHILOSOPHY

DECEMBER 2016

ABSTRACT

Filamentary structures are observed to be common over a wide range of spatial scales and are strongly linked to star formation. In this thesis I present the results of a range of numerical simulations which investigate the stability, collapse and fragmentation of filaments.

The global longitudinal collapse timescale for filaments is found to be considerably longer than for equally dense spheres, allowing sufficient time for local collapse to occur, and to solely occur via the distinctive end-dominated mode. A new free-fall timescale equation for filaments is presented, as well as a semi-analytic model of longitudinal collapse.

The fragmentation of accreting filaments is found to be more complicated than that of equilibrium filaments, and is dominated by the behaviour of longitudinal gravo-acoustic oscillations. This results in the fastest growing perturbation mode being independent of filament width. The non-equilibrium model presented here allows observers to estimate the age of a fragmenting filament and the mass accretion rate.

Simulations of filaments accreting from an inhomogeneous, turbulent medium show that turbulence has a large impact on the fragmentation of a filament. When the turbulence is sub-sonic, a filament fragments in a two-tiered hierarchical manner. As the energy in the turbulent field increases, the filament fragments into elongated fibre-like sub-structures. The formation of these fibre-like structures is intimately linked to the vorticity of the velocity field in the filament and the accretion onto the filament.

In addition, I present synthetic C^{18}O observations and show that the fibre-like sub-structures appear as velocity-coherent structures, well separated in velocity space, similar to the fibres observed by Hacar & Tafalla (2011).

CONTENTS

List of Figures	4
1 Introduction	13
1.1 Star formation	13
1.2 The interstellar medium	14
1.2.1 Molecular clouds	14
1.2.2 Cores	17
1.2.3 Filaments	18
1.3 Feedback	25
1.4 Aim of this thesis	25
1.4.1 Thesis plan	26
2 SPH	27
2.1 Numerical hydrodynamics	27
2.1.1 Eulerian grid codes	28
2.1.2 SPH codes	28
2.1.3 Moving-mesh codes	29
2.2 Basic principles of SPH	29
2.2.1 Smoothing kernel	30
2.3 Smoothing length	31
2.4 The hydrodynamical equations in SPH	32
2.4.1 Equation of state	33
2.5 Artificial viscosity	34
2.5.1 Time-dependent artificial viscosity	35
2.6 Gravity	35
2.6.1 Tree gravity	36
2.6.2 Kernel-softened gravity	37
2.6.3 Periodic gravity	37
2.7 Integration schemes	38
2.8 Timesteps	39
2.9 Sinks	39
2.9.1 Sink creation	40
2.9.2 Accretion onto sinks	41
2.10 Resolution	42
2.11 Summary	43

3	Global Collapse	45
3.1	Introduction	47
3.2	Numerical Setup	48
3.3	Results	49
3.4	Discussion	51
	3.4.1 Semi-Analytical Model	54
	3.4.2 Observational evidence of end-dominated collapse	65
3.5	Summary	68
4	Perturbation Growth	71
4.1	Introduction	72
4.2	Numerical Setup	73
4.3	Results	76
4.4	Discussion	77
	4.4.1 Multi-wavelength perturbations	84
4.5	Summary	89
5	Turbulent Accretion	91
5.1	Introduction	92
5.2	Numerical Setup	93
	5.2.1 Turbulent velocity fields	95
5.3	Results	95
5.4	Discussion	100
	5.4.1 Initially subsonic turbulence	100
	5.4.2 Initially transonic turbulence	104
	5.4.3 Initially supersonic turbulence	104
	5.4.4 Dendrograms	108
	5.4.5 The formation of fibre-like structures	111
	5.4.6 Accretion driven turbulence	120
5.5	Conclusions	123
6	Synthetic Images	129
6.1	Introduction	129
6.2	Numerical Setup	132
6.3	Results	133
	6.3.1 Synthetic Observations	133
6.4	Discussion	136
6.5	Conclusions	142
7	Summary	147
7.1	Global collapse of filaments	147
7.2	Perturbation growth in accreting filaments	148
7.3	Fragmentation of filaments accreting from a turbulent medium	148
7.4	Synthetic images of fragmenting filaments	149
7.5	Future work	149
	7.5.1 Global collapse and dynamics	150

7.5.2	Filament fragmentation	150
7.5.3	Filaments and feedback	152

Bibliography		153
---------------------	--	------------

LIST OF FIGURES

- 1.1 A Herschel column density map of the Taurus L1495 cloud taken from Marsh et al. (2016). There exists substantial sub-structure in the cloud, mainly in the form of filaments. The green circles show the unbound starless cores, the blue diamonds show the prestellar cores. Note that the prestellar cores are found predominately within the filaments. . . . 15
- 3.1 (a) The volume-density profile, and (b) the velocity profile, along the z -axis at time $t = 0.55$ Myr, from the simulations of filaments having $\mu_{\text{O}} = 10 M_{\odot} \text{pc}^{-1}$, $R_{\text{O}} = 0.1 \text{pc}$ and $A_{\text{O}} = 3$ (blue lines) or $A_{\text{O}} = 10$ (green lines). The signatures of end-dominated collapse are clearly seen in both, viz. strong density peaks and supersonic inwards motions at the extremes, representing the end-clumps that dominate the dynamics. The horizontal red line in figure (a) is the initial volume density; interior material is relatively unaffected by the collapse until the density peaks reach it. 50
- 3.2 The filled circles show values of the collapse time, t_{COL} , obtained when (a) the aspect ratio, A_{O} , is varied and μ_{O} and R_{O} are fixed at their fiducial values; (b) the line-density, μ_{O} , is varied and A_{O} and R_{O} are fixed at their high aspect ratio fiducial values; (c) the radius, R_{O} , is varied and A_{O} and μ_{O} are fixed at their high aspect ratio fiducial values. The high aspect ratio fiducial values are $A_{\text{O}} = 10$, $\mu_{\text{O}} = 10 M_{\odot} \text{pc}^{-1}$, and $R_{\text{O}} = 0.1 \text{pc}$. The blue continuous lines are the predictions of Eqn. (3.4). The red and green lines are the predictions from Pon et al. (2012) (Eqns. 3.1 and 3.3 respectively) 52
- 3.3 The filled circles show values of the collapse time, t_{COL} , obtained with different aspect ratios, A_{O} , when the radius, R_{O} , is fixed at 0.1pc , and the line-density is fixed at $\mu_{\text{O}} = 35 M_{\odot} \text{pc}^{-1}$ or $\mu_{\text{O}} = 50 M_{\odot} \text{pc}^{-1}$. The continuous lines are the predictions of Eqn. 3.4 with $\rho_{\text{O}} = \mu_{\text{O}}/\pi R_{\text{O}}^2$ 53

- 3.4 The velocity of the $z > 0$ end-clump as a function of time for filaments with initial line-density $\mu_o = 10 M_\odot \text{pc}^{-1}$, radius $R_o = 0.1 \text{pc}$, and different initial aspect ratios, $A_o = 3, 5, 10,$ and 20 . In the high aspect ratio simulations the end-clump accelerates inwards for the first $\sim 1 \text{Myr}$, but then approaches a terminal velocity, which is only weakly dependent on A_o . The sudden increase in the negative velocity at the end of each profile is due to the two end-clumps becoming so close that the motion is dominated by their mutual gravitational attraction; there is essentially no gas left in between them to sweep up. 55
- 3.5 (a) The gas velocity along the z -axis at time $t = 1.2 \text{Myr}$, for the filament with $A_o = 10$, $\mu_o = 10 M_\odot \text{pc}^{-1}$ and $R_o = 0.1 \text{pc}$. The gas just interior to the converging end-clumps is moving outwards, thereby increasing the ram-pressure that this gas delivers to the end-clump when it is swept up. (b) The density profile of the same filament at the same point in time. The density peaks (i.e the end-clumps) are at the same position as the velocity peaks. Note the uniformity of the interior density, it has remained roughly constant and uniform since the start of the simulation. 56
- 3.6 The total kinetic energy and the work done on the gas plotted against time for both the high and the low aspect ratio fiducial cases ($\mu_o = 10 M_\odot \text{pc}^{-1}$, $R_o = 0.1 \text{pc}$ and $A_o = 10$ or $A_o = 3$). For the $A_o = 10$ case, the end-clumps approach their terminal velocity, around 1Myr ; thereafter, the *rate* at which work is done exceeds the *rate* of increase of the kinetic energy. This is not seen in the $A_o = 3$ case due to the filament collapsing before terminal velocity is reached; the abrupt shift in energies at $\sim 1.1 \text{Myr}$ is due to the end-clumps meeting at $z = 0$. . 57
- 3.7 The z -velocity of the gas just interior to the $z > 0$ end-clump as a function of time. At early times, this gas flows inward with the end-clump, but at later times, it is attracted gravitationally to the end-clump and moves outwards to meet it. Close to the end of the collapse, the interior material begins to be gravitationally attracted by the $z < 0$ end-clump resulting in the velocity maximum at $\sim 2.2 \text{Myr}$ 60
- 3.8 The mass of the $z > 0$ simulated end-clump is compared with the end-clump mass expected if the interior material was stationary, $M(t) = \mu_o(Z_o - z(t))$. The masses are within $\sim 10\%$ over the course of the simulation. 61
- 3.9 A comparison between simulation data and the semi-analytic model for a filament characterised by $\mu_o = 10 M_\odot \text{pc}^{-1}$, $R_o = 0.1 \text{pc}$ and either $A_o = 10$ or $A_o = 3$. (a) The position of the end-clump as a function of time. It starts at $t = 0.2 \text{Myr}$ when the end-clumps are clearly established. (b) The velocity of the end-clump as a function of time. The velocity of the $A_o = 3$ end clump has been shifted downwards by 0.1km s^{-1} for clarity. Simulation and model profiles fit reasonably well for both initial aspect ratios. 63

- 3.10 A test of the validity of equation 3.8; $\log_{10}(dz/dt - dz_1/dt)$ is plotted against $\log_{10}(Z_o - z(t))$ for the high aspect ratio fiducial case. The simulation data are well fit by a straight line with a gradient of 0.64, close to the expected 0.5. The oscillations around the linear fit show that once the terminal velocity is approached, the dynamics is stable. 64
- 3.11 A 3.2mm continuum image of the IRDC 18223 filament, figure 2 in Beuther et al. (2015). The most notable feature of this cloud are the two massive cores at either end of the filament, cores 2 and 11. These two cores could be the end-clumps formed due to global collapse. . . . 66
- 3.12 The time evolution of the ratio between the density of gas in the end-clumps and gas in the interior material. The evolution of this ‘contrast’ ratio is independent of the initial aspect ratio of the filament (the blue and green lines.) It is solely dependent on the initial density of the filament, as seen when comparing the red and the green lines. This dependence is characterised by a stretching in the x -axis by a factor of $\rho_o^{-1/2}$ 67
- 3.13 The time evolution of the contrast ratio for IRDC 18223 assuming number densities of $n = 10^5 \text{ cm}^{-3}$ and $n = 10^4 \text{ cm}^{-3}$. Using the observed column densities in Beuther et al. (2015), the contrast ratio is found to be $\sim 5-6$. This leads to a timescale in the range $0.4 \pm 0.25 \text{ Myr}$. 67
- 4.1 The column density projected onto the x - z plane for the fiducial case (i.e. $A = 0.2$, $\lambda = 0.2 \text{ pc}$, $T_o = 40 \text{ K}$ and $\dot{\mu} = 70 M_\odot \text{ pc}^{-1} \text{ Myr}^{-1}$) at two different times. On the left, at $t = 0.15 \text{ Myr}$, the filament has formed on the z axis, it is sub-critical and confined by the ram pressure of the accreting gas. On the right, at $t = 0.55 \text{ Myr}$, the filament has become supercritical and is contracting radially; at the same time the seeded perturbations have become sites of local collapse. Created using the visualisation tool SPLASH (Price, 2007). 74
- 4.2 The time evolution of the full width half maximum (FWHM) of the filament’s longitudinal and azimuthally averaged radial density profile for the simulations with $T_o = 40 \text{ K}$, $\dot{\mu} = 70 M_\odot \text{ pc}^{-1} \text{ Myr}^{-1}$, $A = 0.2$ and $\lambda = 0.1 \text{ pc}$. One can see that the diameter is in range $0.05-0.12 \text{ pc}$ for much of the filament’s evolution. 78
- 4.3 The dispersion relation between perturbation wavelength and perturbation growth rate for $T_o = 40 \text{ K}$, $\dot{\mu} = 70 M_\odot \text{ pc}^{-1} \text{ Myr}^{-1}$ and $A = 0.2$ (the fiducial case) and also with $A = 0.1$. There no longer exists a single local maximum at 4 times the filament’s diameter, instead there exists a series of peaks and troughs. The initial amplitude of the perturbations does not affect the shape of the dispersion relation, rather it only affects the magnitude of the growth rate. 79

- 4.4 The dispersion relation between perturbation wavelength and normalised growth rate for the fiducial case ($\dot{\mu} = 70 M_{\odot} \text{ pc}^{-1} \text{ Myr}^{-1}$), and for the case with $\dot{\mu} = 100 M_{\odot} \text{ pc}^{-1} \text{ Myr}^{-1}$. The normalised growth rate is defined as $\hat{g}_{\lambda} = g_{\lambda}/g_{0.05\text{pc}}$. The fiducial case (solid blue line) and the case with a higher accretion rate (dashed red line) are out of phase, the peaks in the dispersion relation do not line up. The higher accretion rate has caused the relation to be squeezed in the x-direction. The green dotted line is the result of stretching the high accretion line assuming the dispersion relation takes the form $g_{\lambda} = f(\lambda/\tau_{\text{CRIT}})$, where τ_{CRIT} is the time at which the filament becomes supercritical. The peaks in the stretched dispersion relation now line up with those from the fiducial case. 80
- 4.5 The dispersion relation between perturbation wavelength and normalised growth rate for the fiducial case ($T_{\text{O}} = 40 \text{ K}$), and for the case with $T_{\text{O}} = 10 \text{ K}$. The normalised growth rate is defined as $\hat{g}_{\lambda} = g_{\lambda}/g_{0.05\text{pc}}$. The fiducial case (solid blue line) and the case with the lower temperature (dashed red line) are out of phase. The lower temperature has caused the relation to be squeezed in the x-direction. The green dotted line is the result of stretching the $T_{\text{O}} = 10 \text{ K}$ line assuming the dispersion relation takes the form $g_{\lambda} = f'(\lambda/a_{\text{O}})$, where a_{O} is the isothermal sound speed. The peaks in the stretched dispersion relation now line up with those from the fiducial case. 81
- 4.6 The normalised volume-density profile, $\rho / \langle \rho \rangle$, along the z -axis for the fiducial case at two different times, $t = 0.05 \text{ Myr}$ (blue solid line) and $t = 0.30 \text{ Myr}$ (green dashed line). A standing gravo-acoustic wave is set up along the filament's length; the locations of the initial density peaks are the anti-nodes of the wave. The density peaks and trough switch after 0.25 Myr has passed, i.e. half an oscillation period. . . . 82
- 4.7 The longitudinal density (blue solid line) and velocity (green dashed line) profiles at $t = 0.45 \text{ Myr}$ for the simulation with $\lambda = 0.2 \text{ pc}$, $T_{\text{O}} = 40 \text{ K}$, $\dot{\mu} = 70 M_{\odot} \text{ pc}^{-1} \text{ Myr}^{-1}$ and $A = 0.2$. This is the time at which the perturbations are just becoming self-gravitating and the filament is close to becoming globally super-critical. The red dotted line is the $v = 0 \text{ km/s}$ line, which is included to help the reader see the converging and diverging regions along the filament. The velocity field is out of phase with the density field, and the main converging flows are positioned where the troughs of the density profile are. Because of this the majority of the gas is moving away from the density peaks just as radial collapse is about to begin. There are small converging flows at the central density peaks because these regions have just become self-gravitating. 85
- 4.8 The longitudinal density profile for one of the $\alpha = -1.6$ simulations at $t = 0.05 \text{ Myr}$ (top) and $t = 0.56 \text{ Myr}$ (bottom). The density peaks (cores) at $t = 0.56 \text{ Myr}$, are roughly periodically spaced, having an average separation of 0.24 pc 86

- 4.9 Histograms showing the distribution of core spacings in a set of 30 simulations. The blue line shows the core spacings for the ten simulations where $\alpha = -1.6$, the green line shows the core spacings from the ten simulations where $\alpha = -1.3$ and the red line shows the core spacing for the ten simulations where $\alpha = -1.9$. Spacings below 0.05 pc were removed; in a number of simulations a few cores form very close together, ~ 0.02 pc, these clusters are then separated by much greater distances. The change in power index does not affect the distribution, all three distributions are strongly peaked at ~ 0.3 pc. Considering all 30 simulations together, a sample of 114 spacings, the distribution has a mean of 0.296 pc and a standard deviation of 0.070 pc 87
- 5.1 The volume density profile along the z -axis at $t = 0.4$ Myr showing density perturbations on many different scales. The turbulent field has a natural mix of compressive and solenoidal modes, $\delta_{\text{sol}} = 2/3$, and a subsonic velocity dispersion, $\sigma_{3\text{D}} = 0.1$ km/s. 97
- 5.2 Histograms showing the distribution of core separation distances for the set of simulations initialized with a natural mix of turbulence, $\delta_{\text{sol}} = 2/3$, for (a) $\sigma_{3\text{D}} = 0.1$ km/s, (b) $\sigma_{3\text{D}} = 0.4$ km/s and (c) $\sigma_{3\text{D}} = 1$ km/s. Figures a, b and c have 58, 41 and 23 separations respectively. The sub-sonic case (a) has an inset to show the distribution of small scale separations (< 0.3 pc) in more detail. Note that a separation of 3 pc is recorded when the filament has only produced one core. 98
- 5.3 Histograms showing the distribution of core separation distances for the set of simulations initialized with purely compressive turbulence, $\delta_{\text{sol}} = 0$, for (a) $\sigma_{3\text{D}} = 0.1$ km/s, (b) $\sigma_{3\text{D}} = 0.4$ km/s and (c) $\sigma_{3\text{D}} = 1$ km/s. Figures a, b and c have 56, 25 and 36 separations respectively. The sub-sonic case (a) has an inset to show the distribution of small scale separations (< 0.3 pc) in more detail. Note that a separation of 3 pc is recorded when the filament has only produced one core. 99
- 5.4 Average velocity dispersion as a function of time for the subsonic (solid blue), transonic (dot-dashed green) and supersonic (dashed red) for (top) natural mix turbulence simulations and (bottom) purely compressive turbulence simulations. In all 6 cases the velocity dispersion tends to stabilise at a roughly transonic level, $\sim 0.4 \pm 0.15$ km/s. . . . 101
- 5.5 Ratio of the number of large scale core separations (> 0.3 pc) over the number of small scale core separations (< 0.3 pc) as a function of time for subsonic natural mix turbulence simulations. Large scale separations dominate at early times, but small scale separations become more common very quickly, on the order of a tenth of a megayear. . . 103
- 5.6 Column density maps at $t = 0.5$ Myr for two of the filaments with initially supersonic turbulence, $\sigma_{3\text{D}} = 1$ km/s but different types of turbulence. On the left, (a), is the natural mix case, $\delta_{\text{sol}} = 2/3$, which shows numerous elongated sub-structures. On the right, (b), is the purely compressive turbulence, $\delta_{\text{sol}} = 0$, which is more ‘clumpy’ but still shows elongated sub-structure. 105

- 5.7 A map of the velocity component perpendicular to the plane, the ‘line-of-sight’ velocity v_y , at $y = 0$ pc with density contours overlaid for an initially supersonic natural mix turbulence simulation at $t = 0.5$ Myr. The density contours are at $2, 4, 6, 8, 10 \times 10^{-20}$ g/cm $^{-3}$. One can see that the dense elongated structures exhibit smooth and small variations in velocity. Those regions that show large variations are in the diffuse gas, outside the density contours, or in the high density cores which are undergoing collapse. 107
- 5.8 Dendrograms constructed using the three-dimensional volume density cubes of (top) a simulations with a natural mix of turbulence, and (bottom) a simulations with purely compressive turbulence. One can see that a natural mix of turbulence produces greater sub-structure, and that sub-structure is more hierarchical, than the simulations with purely compressive turbulence. 109
- 5.9 Dendrograms constructed using the two-dimensional column density maps of (top) a simulations with a natural mix of turbulence, and (bottom) a simulations with purely compressive turbulence. One can see that there is not a significant difference in either the amount of sub-structure, or hierarchical the sub-structure is. 110
- 5.10 A section of the column density plot in figure 5.6 with a diagram highlighting a hub network. The circled region is the hub in which a star forms. This hub is at the intersection of numerous filamentary sub-structures. The hub network is a true structure in three dimensions and can be seen in the volume density contours in figure 5.12. 112
- 5.11 The normalised distributions of the magnitude of the three vorticity components, ω_x , ω_y and ω_z , for an initially supersonic turbulent filament at $t = 0.5$ Myr. The distribution of the vorticity parallel to the longitudinal axis of the filament, ω_z , shows a significant wing at large magnitudes. 112
- 5.12 (Left) A map of the vorticity component parallel to the longitudinal axis of the filament, the z -axis, at $y = 0$ pc with density contours overlaid for an initially supersonic natural mix turbulence simulation. (Right) A map of the divergence of the velocity field in the filament, at $y = 0$ pc with the same density contours. The density contours are at $2, 4, 6, 8, 10 \times 10^{-20}$ g/cm $^{-3}$. One can see that the density structures follow the regions in which there exists a large vorticity gradient in the x -direction, i.e. where there are lines of blue and red/yellow next to each other. The divergence is seen to trace the accretion shock onto the main filament, but does not correlate well with the dense structures. 113
- 5.13 Plots showing volume density against the velocity quantities listed in table 5.1. One can see that the relationship between $|\omega_z|$ and $|\delta\omega_z/\delta x|$, and density is both tighter and steeper than the link between the other velocity quantities and density. 116

- 5.14 A map of the vorticity component parallel to, on the left, the x -axis and, on the right, the component parallel to the y -axis at $y = 0$ pc with density contours overlaid for an initially supersonic natural mix turbulence simulation. The density contours are at $2, 4, 6, 8, 10 \times 10^{-20} \text{ g/cm}^{-3}$. Neither plot shows a strong correlation between vorticity and the density structure. 117
- 5.15 (Left) A map of the mass-weighted vorticity component parallel to the longitudinal axis of the filament, the z -axis, at $y = 0$ pc with density contours overlaid for an initially supersonic natural mix turbulence simulation. (Right) A map of the mass-weighted divergence of the velocity field in the filament, at $y = 0$ pc with the same density contours. The density contours are at $2, 4, 6, 8, 10 \times 10^{-20} \text{ g/cm}^{-3}$. One can see regions with high values of mass-weighted divergence/vorticity lie within the highest density contours, this is due to the fact the density varies by a few orders of magnitude while divergence/vorticity only vary by a single order of magnitude. 118
- 5.16 A face down view illustrating how two nearby sites with anti-parallel vorticity vectors can produce regions of higher density. The two flows are able to bring gas into the centre from both direction where it can be held together by self-gravity and form a fibre-like structure. 119
- 5.17 Column density plots of two natural-mix, initially supersonic turbulence simulations which have the same initial conditions, (top) shows the simulation with self-gravity, (bottom) shows the simulation without self-gravity. One can see that both simulations show the same elongated sub-structure, but the sub-structures are more well defined when self-gravity is included. Thus the velocity field is the dominant mechanism for the formation of these fibre-like structures, gravity acts against dispersal but is not necessary for their formation. 120
- 5.18 Analytically estimated velocity dispersion due to driving by accretion for the subsonic natural mix turbulence simulations (equation 5.9). A driving efficiency between 5% and 10% is necessary to produce a velocity dispersion $\sim 0.4 \text{ km/s}$ as seen in the simulations. 121
- 5.19 (a) The azimuthally and longitudinally averaged radial volume density profiles for the three natural mix turbulent cases, initially sub-, tran- and supersonic velocity dispersions, at the end of the simulations when the filaments have line-densities $\sim 1.3 \mu_{\text{CRIT}}$. (b) The longitudinally averaged radial column density profiles for the same simulations. The error bars show the inter-quartile range around the median. 122
- 6.1 The probability density function of a cell's radius and density at the end of a simulation. The red line shows the Jeans length at 10 K for the entire density range. One can see that the Jeans length is well resolved over a wide range of densities. 131
- 6.2 Column density map for a filament with (top) natural mix turbulence and (bottom) purely compressive turbulence. Both show sub-structure but the natural mix simulation shows numerous elongated sub-structures. 134

6.3	Integrated emission map of C ¹⁸ O for a natural mix turbulence simulation just before the first sink particle forms. The contours show the true H ₂ column density from the simulation with levels: 0.5, 0.7, 2, 4, 5, 7, 20 × 10 ²² cm ⁻²	137
6.4	Intensity-weighted mean velocity of C ¹⁸ O for a natural mix turbulence simulation just before the first sink particle forms. The contours show the true H ₂ column density from the simulation with levels: 0.5, 0.7, 2, 4, 5, 7, 20 × 10 ²² cm ⁻²	138
6.5	Intensity-weighted velocity dispersion of C ¹⁸ O for a natural mix turbulence simulation just before the first sink particle forms. The contours show the true H ₂ column density from the simulation with levels: 0.5, 0.7, 2, 4, 5, 7, 20 × 10 ²² cm ⁻²	139
6.6	C ¹⁸ O spectra at 5 separate pixel locations. The positions of the pixels are shown with the black circles on the integrated intensity map, with the top circle showing the position of the top spectrum and so forth. One can see that there are a number of locations which have multiple velocity components along the line of sight.	140
6.7	Longitudinal stripes taken from the integrated emission map and viewed in position-velocity space, where the leftmost stripe corresponds to the leftmost PV diagram and so forth. One can see what appears to be a single filament in integrated emission is found to be several smaller velocity-coherent sub-filaments which are well separated in velocity, i.e. fibres.	143
6.8	Horizontal stripes taken from the integrated emission map and viewed in position-velocity space, where the uppermost stripe corresponds to the uppermost PV diagram and so forth. The fibres are well separated in velocity space, ~ 1 km/s, even though they are only separated by ~ 0.1 pc in the radial direction.	144
6.9	On the left are the same 5 spectra seen in figure 6.6, on the right is the density along the line of sight for those spectra. The colours show the gas that is contributing to the same colour peak in emission. Line of sight confusion is evident in a number of cases, where multiple separated peaks in density are blended into single peaks in emission, and where numerous peaks in emission are not coming from separated regions in PPP space.	145

CHAPTER 1

INTRODUCTION

1.1 STAR FORMATION

The study of stars has been central to astronomy since the field began. Over the centuries astronomers have managed to categorise and study a wide variety of stars, from brown dwarfs to blue supergiants. Our understanding of stellar evolution, epitomised by the famous Hertzsprung-Russell diagram, has progressed tremendously over the last century. However, the field of star formation is less developed due to the technical difficulty of observing young stellar objects (YSOs). The progress made in infra-red and sub-millimetre astronomy during the previous fifty years has only relatively recently allowed us to probe the dense dark clouds in which new stars form.

The star formation problem is one that spans twenty orders of magnitude in density, eight orders of magnitude in length-scale and six orders of magnitude in temperature. The physical processes involved, such as gravity and hydrodynamics, are non-linear and can only be solved analytically for the simplest of configurations. The advent of powerful computers has given theorists the ability to model the complex gas dynamics that lead to the formation of stars, and to provide a framework against which to interpret the observations from infra-red and sub-millimetre telescopes.

Recent observations by the Herschel Space Observatory have revealed that filamentary structures are prevalent within molecular clouds and that star-forming cores are often embedded within them. The aim of this thesis is to perform numerical simulations of filaments so that we may better understand their role in the star formation process.

1.2 THE INTERSTELLAR MEDIUM

The interstellar medium (ISM) is the name given to the gas and dust that resides between the stars, accounting for 10 – 15% of the baryonic mass in the Milky Way (Tavakoli, 2012; Roman-Duval et al., 2016). McKee & Ostriker (1977) put forward a three phase model of the ISM: a cold dense phase with temperatures less than 300K, consisting mainly of atomic and molecular hydrogen; a warm phase with temperatures $\sim 10^4$ K, predominately ionized hydrogen; and a very hot phase, $T \sim 10^6$ K, which has been heated by supernovae shocks and is the largest component of the ISM by volume. Within a galaxy, gas is continually moving between the different phases. In some locations, it cools and becomes more dense until molecular gas forms and gravitational collapse leads to the formation of YSOs. The massive stars produce strong feedback effects in the form of stellar winds (Leitherer, Robert & Drissen, 1992; Lopez et al., 2011), supernova explosions (Hill et al., 2012; Walch & Naab, 2015) and ionizing radiation (Dale et al., 2005; Walch et al., 2012), heating and dispersing the gas so that it returns to the warm and hot phases.

1.2.1 MOLECULAR CLOUDS

Molecular clouds are extended regions of dense cold atomic and molecular gas, thought to be formed due to the turbulent nature of the ISM and the galactic potential (Vazquez-Semadeni, Passot & Pouquet, 1995; Blitz & Rosolowsky, 2005; Stark & Lee, 2005). Molecular clouds have masses ranging from 10^2 to $10^6 M_{\odot}$ and diameters between 1 pc and 100 pc. Clouds with masses greater than $10^4 M_{\odot}$ are categorised as giant molecular clouds (GMCs).

Molecular clouds become molecular due to their high column densities allowing dust to adequately shield the gas from UV photons in the interstellar radiation field (ISRF). As the abundance of molecular hydrogen increases it can self-shield, further increasing the molecular gas fraction. As well as molecular hydrogen, more complicated molecular species, e.g. HCO^+ , CO, NH_3 can also form due to shielding and the high volume densities. The presence of CO allows the gas in molecular clouds to cool efficiently and the gas typically reaches an equilibrium temperature of ~ 10 K (Bergin & Tafalla, 2007). Even without the presence of CO, cooling due to C^+ and O fine structure lines can allow gas to reach 20 K in well-shielded regions (Glover & Clark, 2012b).

Although the main component of molecular clouds is molecular hydrogen, it cannot be used to observe molecular clouds. This is because molecular hydrogen is a homo-nuclear molecule, and as such it does not have a permanent dipole moment and

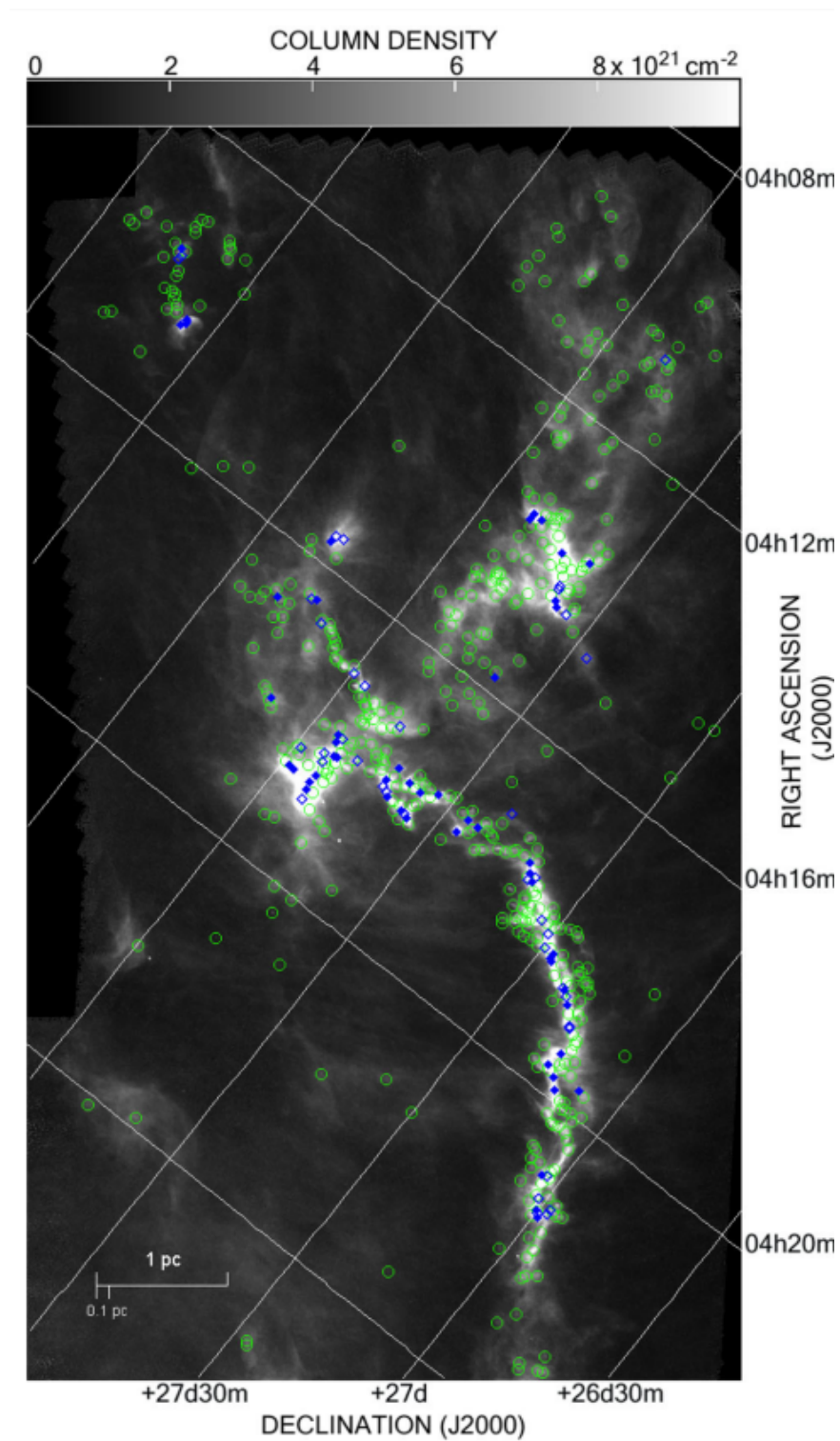


Figure 1.1. A Herschel column density map of the Taurus L1495 cloud taken from Marsh et al. (2016). There exists substantial sub-structure in the cloud, mainly in the form of filaments. The green circles show the unbound starless cores, the blue diamonds show the prestellar cores. Note that the prestellar cores are found predominately within the filaments.

its rotational transitions are weak. Moreover, its lowest energy rotational transition is too energetic to be excited at the low temperatures typical in molecular clouds. Thus the structure and kinematics of molecular clouds are inferred using indirect tracers, dust and other molecular lines. Dust is typically used as a tracer for column density as the continuum emission from dust is usually optically thin at sub-millimetre wavelengths (Motte, Andre & Neri, 1998; André et al., 2010). Molecular lines may also be used to estimate column densities but this is harder because the lines may be optically thick, the species involved may not have the same relative abundances everywhere, and there may be variations in excitation temperature along the line of sight. Typically molecular line studies are used to investigate the kinematics of the molecular cloud; the centroid velocity can tell one about the flows inside the molecular cloud, and the line width about the amount of the disorder in the flow (Ballesteros-Paredes, 2006; Hacar & Tafalla, 2011; Ragan et al., 2014; Beuther et al., 2015; Kainulainen et al., 2016a).

Molecular clouds are not single smooth structures, rather they exhibit a high level of sub-structure, typically in the form of filaments (André et al., 2010). Figure 1.1 shows the significant amount of sub-structure found in the Taurus L1495 cloud. The high density gas exists in filaments and clumps, the green and blue symbols denote the locations of the cores. Furthermore, the sub-structure present in molecular clouds can be quantified using fractals; this allows objective comparisons of fragmentation in different clouds (Blitz & Williams, 1999, Jaffa et al. submitted).

The presence of a substantial amount of sub-structure is ascribed to turbulence, as evidenced by significant non-thermal line widths in molecular line emission (Larson, 1981). This turbulence is likely to be caused by gravity as well as various feedback effects on the local scale, e.g. ionizing radiation, stellar winds and jets (Leitherer, Robert & Drissen, 1992; Gritschneider et al., 2009; Drabek-Maunder et al., 2016), and energy cascading down from large scale effects such as supernovae, galactic flows and galactic accretion (Heitsch et al., 2008; Dib et al., 2009; Klessen & Hennebelle, 2010).

It was long thought that molecular clouds were long-lived structures, i.e structures that survived much longer than their dynamical crossing time (McKee et al., 1993; Blitz & Williams, 1999). This requires a supporting mechanism to act against gravity; magnetic fields were considered the most likely mechanism (Crutcher, 1999). New evidence suggests that molecular clouds are not long-lived, rather they only survive a few free-fall times (Elmegreen, 2000; Ballesteros-Paredes, 2006). Molecular clouds are not necessarily globally bound; instead turbulence promotes fragmentation and the development of sub-structure which leads to high density regions collapsing

locally (Clark & Bonnell, 2004, 2005; Clark et al., 2005).

1.2.2 CORES

Cores are dense condensations of gas in molecular clouds (Motte, Andre & Neri, 1998; Simpson, Nutter & Ward-Thompson, 2008; Lomax, Whitworth & Cartwright, 2013), and are considered the smallest unit of star formation. It is within cores that stars are formed. Cores have radii in the range 0.01 – 0.1 pc, and masses between $0.1 M_{\odot}$ and $10 M_{\odot}$. They may be divided into two categories, proto-stellar and starless. Proto-stellar cores contain a YSO, starless cores do not. Starless cores are often further divided into prestellar, i.e. those that are gravitationally bound, and unbound cores which are thought to be either transient structures or a precursor to prestellar cores.

Prestellar cores are distinguished from unbound cores by considering the Jeans mass. For a spherically symmetric non-rotating core with mean density ρ , temperature T and mean gas particle mass \bar{m} to collapse, its mass must be greater than the Jeans mass (Jeans, 1902) as given by

$$M_J = \left(\frac{375}{4\pi} \right)^{1/2} \frac{a_o^3}{G^{3/2} \rho^{1/2}}, \quad (1.1)$$

where a_o is the isothermal sound speed

$$a_o = \sqrt{\frac{k_B T}{\bar{m}}}. \quad (1.2)$$

Cores are typically observed with transonic non-thermal line widths; many interpret this as turbulent support. This changes equation 1.1 to

$$M_J = \left(\frac{375}{4\pi} \right)^{1/2} \frac{\sigma^3}{G^{3/2} \rho^{1/2}}, \quad (1.3)$$

where $\sigma = \sqrt{\sigma_{NT}^2 + a_o^2}$, and σ_{NT} is the observed non-thermal velocity dispersion.

Observed prestellar cores have density profiles similar to that of a Bonnor-Ebert spheroid that is confined by an external pressure (Alves, Lada & Lada, 2001; Tafalla et al., 2004). However, this does not necessarily imply that prestellar cores are in hydrostatic equilibrium, Bonnor-Ebert-esque density profiles also appear in dynamically evolving cores (Ballesteros-Paredes, Klessen & Vázquez-Semadeni, 2003).

Prestellar cores will initially collapse quasi-isothermally as the gas is optically

thin and gravitational energy can be efficiently radiated away. The core collapses non-homologously and produces a centrally condensed object and a power law envelope, $\rho \propto r^{-2}$ (Larson, 1969). This collapse occurs over a few free-fall times, τ_{ff} , where

$$\tau_{ff} = \sqrt{\frac{3\pi}{32G\rho}}. \quad (1.4)$$

Gas is not directly accreted onto the central protostar as the prestellar cores have angular momentum. As the core collapses, the initial angular velocity of the gas increases as it moves closer to the protostar due to conservation of angular momentum. This rotation results in an accretion disc. The accretion disc allows angular momentum to be transported outwards and material inwards, adding mass to the protostar.

Once the central protostar reaches density of roughly $10^{-13} \text{ g cm}^{-3}$, the gas becomes optically thick to its own dust emission. Further collapse is halted and the central object is known as the first hydrostatic core (FHC), typical radius $\sim 5 \text{ au}$ and typical mass of $\sim 5 \times 10^{-3} M_{\odot}$. The gas in the FHC is heated via Kelvin-Helmholtz contraction as well as accretion shocks at its surface. When the FHC reaches a density of $\sim 10^{-8} \text{ g cm}^{-3}$, the gas reaches a temperature of around 2000 K. At this temperature the molecular hydrogen dissociates. This is followed by the ionization of the gas. These processes are endothermic and allow the gas to become quasi-isothermal and collapse rapidly. A second hydrostatic core (SHC) forms once all of the molecular hydrogen is dissociated at $\rho \sim 10^{-4} \text{ g cm}^{-3}$ and $T \sim 5000 \text{ K}$. The SHC continues to accrete until it reaches stellar densities, $\rho \sim 1 \text{ g cm}^{-3}$ (Larson, 1969; Masunaga & Inutsuka, 2000; Commerçon et al., 2011; Bate, Tricco & Price, 2014).

1.2.3 FILAMENTS

Filaments have been known to play a role in the star formation process for many decades (Barnard, 1910; Schneider & Elmegreen, 1979), however, the recent observations by the Herschel Space Observatory revealed that filaments are prevalent within molecular clouds and act as an intermediate step between molecular clouds and cores; protostellar and prestellar cores are preferentially embedded within filaments, see figure 1.1 (André et al., 2010; Könyves et al., 2015; Marsh et al., 2016).

Filaments are not only prevalent inside molecular clouds, some GMCs are filamentary (Jackson et al., 2010; Beuther et al., 2015; Kainulainen et al., 2016a) and filaments have been observed in cores (Pineda et al., 2015). They can range in length from 0.025 pc to 80 pc and in mass from $1 M_{\odot}$ to $10^5 M_{\odot}$. Observations using Herschel

suggest that those filaments found in molecular clouds have a near universal width of 0.1 pc, independent of a filament's central density (Arzoumanian et al., 2011). Recent work has shown that some high mass GMC filaments also share this characteristic width (André et al., 2016).

Stability and collapse

For an isothermal self-gravitating cylinder of gas in hydrostatic equilibrium there exists a critical line-density given by

$$\mu_{\text{CRIT}} = \frac{2a_o^2}{G}, \quad (1.5)$$

where a_o is the isothermal sound speed (Ostriker, 1964). Above this critical line-density a filament becomes radially unstable and collapses, similar to the Jeans mass for a sphere. Below the critical line-density there always exist a radial density profile which can act against gravity and the external pressure. At 10 K and solar metallicity, typical conditions of molecular clouds, the critical line density is $\sim 16 M_\odot \text{pc}^{-1}$.

Equation 1.5 assumes that thermal pressure is the only supporting mechanism. It is readily generalised to include the transonic line-widths seen in filaments,

$$\mu_{\text{CRIT}} = \frac{2\sigma^2}{G}, \quad (1.6)$$

where $\sigma = \sqrt{\sigma_{NT}^2 + a_o^2}$. This assumes that all non-thermal velocity dispersion is supportive, i.e. that the velocity dispersion is due to turbulence on scales much smaller than the size of the clouds. There are numerous configurations in which this is not the case, e.g. radial collapse, macro-turbulence.

Ostriker (1964) find that for isothermal filaments in hydrostatic equilibrium, i.e. filaments with line-densities less than the critical value, the radial profile is Plummer-like,

$$\rho(r) = \frac{\rho_c}{[1 + (r/r_{\text{FLAT}})^2]^{p/2}}, \quad (1.7)$$

where ρ_c is the density at the centre of the filament, r_{FLAT} is the radius of the flat inner region, and p is the power-law exponent at large radii (Whitworth & Ward-Thompson, 2001). Ostriker (1964) find that $p = 4$ for the equilibrium case; however, observations with Herschel show that $p \approx 2$ (Arzoumanian et al., 2011; Palmeirim et al., 2013). This value is often found in simulations as well (Gómez & Vázquez-Semadeni, 2014; Smith, Glover & Klessen, 2014; Seifried & Walch, 2015). Fischera & Martin (2012) show that pressure-confined filaments which are in equilibrium have

flatter power-law tails than the traditional Ostriker (1964) case. Federrath (2016) argues for a more dynamical explanation. In a turbulent medium filaments will form at the intersection of two planar shocks; as the density profile of post shock gas goes as λ^{-1} , where λ is the post shock thickness, and shock collisions are multiplicative in density (Vázquez-Semadeni, 1994), the collision of two planar shocks will produce a $\rho \propto \lambda^{-2}$ density profile.

As well as collapsing radially, filaments can collapse longitudinally along their main axis. This is normally termed global collapse. It has been shown that lower dimensional structures, such as filaments and sheets, have longer global collapse timescales than equally dense spheres (Burkert & Hartmann, 2004; Pon et al., 2012). This has been corroborated by simulations (Bastien, 1983; Vázquez-Semadeni et al., 2007). Moreover, the same authors have shown that filaments collapse longitudinally via two separate modes: roughly homologously, or via an end-dominated mode in which clumps form at either end and move inwards sweeping up material as they go. This is significantly different to the global collapse of a sphere as described above in section 1.2.2.

Filament formation

Filaments, like sheets, are natural products of supersonic turbulence. This has been shown in numerous simulations that include turbulence, with and without gravity (Porter, Pouquet & Woodward, 1994; Ballesteros-Paredes, Hartmann & Vázquez-Semadeni, 1999; Padoan et al., 2001; Bonnell, Bate & Vine, 2003; Tilley & Pudritz, 2004; Krumholz, Klein & McKee, 2007; Gómez & Vázquez-Semadeni, 2014; Smith, Glover & Klessen, 2014).

Turbulence is modelled as an ensemble of plane waves, with an amplitude governed by a power-law in k -space and random phases. As the collision of two planar waves is a line it follows that filaments are readily produced. Another feature of turbulent velocity fields is that they contain regions with high velocity shear, this has been put forward as a prominent method to form filaments in a turbulent medium (Hennebelle, 2013). Shear may also be an important factor on galactic scales; the rotation of an extended condensate around the galactic centre will cause the region to stretch and become filamentary (Dobbs, 2015). Padoan et al. (2001) put forward the idea that filaments are due to the stagnation regions in a turbulent medium, thus without gravity they are transient objects. The addition of a magnetic field means that low density gas flows along field lines; therefore flows in a turbulent medium are preferentially aligned parallel to magnetic field, leading to large scale convergent

flows forming filaments perpendicular to the magnetic field as seen in observations (Basu et al., 2009; Li et al., 2010; Palmeirim et al., 2013; Planck Collaboration et al., 2016; Cox et al., 2016).

Another method of forming filaments independent of turbulence is the fragmentation of a self-gravitating sheet. Sheets are unstable to perturbations with wavelengths greater than a few times the sheet's thickness (Miyama, Narita & Hayashi, 1987; Whitworth, 2016). The aspect ratio of these perturbations is found to increase with time, leading to the formation of filaments. These sheets could form from a convergent flow in a turbulent field or due to compression from an expanding HII region, a supernova shock or the collision of two clouds. Myers (2009) suggests the numerous 'hub-filament' systems observed resemble the fragmentation of a self-gravitating sheet. Such fragmentation leading to the formation of 'hub-filament' systems has been seen in simulations (Van Loo, Keto & Zhang, 2014; Balfour et al., 2015)

Characteristic filament width

The reason for the observed characteristic width is so far unclear. It is often remarked that 0.1 pc is the length scale at which the Larson (1981) law linking linewidth and length scale breaks down and turbulent gas motion changes from supersonic to subsonic. This suggests that the characteristic width is due to turbulence and is set by the sonic scale which governs the transition to 'coherence' (Federrath, 2016). However, the densest filaments, those that are self-gravitating, are expected to contract radially and become narrower over time. Arzoumanian et al. (2013) posit that as filaments are not isolated structures, but rather interact with their surroundings, accretion drives turbulence inside the filament. Heitsch (2013) shows that this acts as a supporting mechanism and produces a filament width of about 0.1 pc over wide range of peak column densities, but there is still a dependence on peak column density. Hennebelle & André (2013) show that if accretion-driven turbulence is allowed to dissipate due to ion-neutral friction, the filament width is comparable to observations and only has a slight dependence on peak column density.

The characteristic width is only seen when studying dust continuum data. Panopoulou et al. (2014), who use ^{13}CO line data, show that the filaments in Taurus have a broad distribution of widths, peaked at 0.4 pc. Furthermore, when limited to velocity-coherent filaments Panopoulou et al. (2014) find a peak in the width distribution at 0.2 pc. The difference is due to fake filamentary structures appearing when analysing the integrated emission map, a problem that may be common in dust emission which does not include velocity information. However, ^{13}CO can suffer from

two effects that may widen the observed peaks: freeze-out and high optical depth at high density.

Observations using other tracers such as C^{18}O , N_2H^+ and NH_3 , have revealed a different picture. What appear to be filaments in the plane of the sky become a set of velocity coherent sub-filaments (Hacar et al., 2013; Fehér et al., 2016). These sub-filaments are typically narrower than those seen in dust emission. Their narrowness may be real or could be due to the low abundance of such tracers in the low density wings of the filament. The presence of velocity coherent sub-filaments masquerading as larger continuous filaments when seen in integrated emission or dust continuum means that discussing the width of Herschel filaments may be misleading.

The problem of line-of-sight confusion is avoided in simulations. Simulations of filaments have found it difficult to recover a characteristic width of 0.1 pc. The dense star-forming filaments contract and have widths much less than 0.1 pc. Federrath (2016) present simulations that involve various combinations of gravity, turbulence, magnetic fields and jets, they determine that simulations that include turbulence produce 0.1 pc filaments over a wide range of peak column densities. However, they only fit the density profile within 0.1 pc of the filament spine. Smith, Glover & Klessen (2014) find that the width measurement is highly dependent on the fitting range, smaller ranges lead to smaller widths and vice versa. Thus it is unclear if the results presented in Federrath (2016) are robust. The simulations presented in Smith, Glover & Klessen (2014), which included turbulence and gravity, show a mean width of 0.2 pc when data within 0.35 pc of the filament spine is fitted, as is the case in most observations, and that the mean width is not constant with peak density. Seifried & Walch (2015) show that only the presence of a magnetic field can reproduce the observed width for both starless and star-forming filaments, as long as the magnetic field is oriented parallel to the filament's long axis. However, observations have shown that magnetic fields are typically aligned perpendicular to the filament's main axis (Palmeirim et al., 2013; Planck Collaboration et al., 2016; Cox et al., 2016).

A recent re-analysis of the Herschel data has cast doubt on the existence of a characteristic width. Panopoulou et al. (2016) show that the characteristic width found in earlier work is due to the methodology used. The narrowness of the filament width distribution produced by Arzoumanian et al. (2011) is found to be a consequence of averaging the filament width over the filament's entire length. This methodology also produces a peaked width distribution when used to measure the widths of artificial scale-free filaments. Panopoulou et al. (2016) show that the observed filament width distribution can be modelled as a truncated power-law distribution which has been sampled with uncertainties of ~ 0.036 pc; this is able to

produce a peak in the observed distribution even when the underlying distribution is scale-free.

Fragmentation

Due to their long global collapse timescales, filaments are more prone to fragmentation than spheres. By considering the local and global collapse timescales, Pon, Johnstone & Heitsch (2011) show that density perturbations in a sphere must have high amplitudes ($A \equiv \Delta\rho/\rho > 5$) for fragmentation to occur before global collapse halts it. However, filaments can readily fragment with only small amplitude perturbations, $A > 0.1$. Filaments are therefore likely to play a key role in the formation of cores within molecular clouds.

Previous theoretical work has studied how such perturbations grow in the linear and non-linear regimes and has shown a clear difference between filaments and spheres. For spherical clouds, the growth rate increases monotonically with the perturbation wavelength; thus the fastest growing mode is the largest mode, i.e. global collapse. It is for this reason that only very large amplitude density perturbations have time to collapse in spheres. Inutsuka & Miyama (1992) performed an analytic perturbation analysis for unmagnetised isothermal and polytropic equilibrium filaments. They find that perturbation growth is determined by the filament's diameter. Only perturbations with wavelengths greater than roughly 2 times the diameter are unstable and grow. Moreover, unlike a sphere the fastest growing perturbation is not the one with the largest wavelength, rather the most unstable wavelength is roughly 4 times the diameter. Fischera & Martin (2012) expand this to pressure-confined filaments with sub-critical line-densities and find the same dispersion relation linking perturbation wavelength and growth rate.

Inutsuka & Miyama (1997) find that super-critical filaments are unlikely to fragment without the presence of an initial large perturbation. Thus, the fragmentation of such a filament is determined when the filament becomes sufficiently dense that it transitions from being isothermal to roughly adiabatic. This transition causes the filament to stop radially contracting. The resulting fragmentation is thought to depend on the density perturbation power spectrum at the adiabatic stage (Inutsuka, 2001).

The effects of magnetic fields have also been considered (Nagasawa, 1987; Fiege & Pudritz, 2000). An axial magnetic field acts as a stabilising mechanism, the critical line-density increases as well as the wavelength of the fastest growing mode. Helical fields can also act to stabilise the filament, increasing the wavelength

of the fastest growing mode and decreasing the growth rate. However, there is a transition between gravity-driven fragmentation and magnetohydrodynamics-driven fragmentation. When the ratio of toroidal to poloidal field is less than 2, gravity dominates the fragmentation process; above 2 fragmentation is dominated by an MHD ‘sausage’ instability. This ‘sausage’ instability causes the fastest growing mode to occur at smaller wavelengths, and the growth rate to increase dramatically.

Filaments may also fragment due to spatial perturbations (Gritschneider, Heigl & Burkert, 2016). A radially stable filament with initially uniform density may be made to fragment by bending it. This has been termed geometrical fragmentation. A bent filament oscillates and material accumulates at the anti-nodes. The concentration of higher density gas leads to collapse and the formation of cores. Thus, a filament may be made to fragment at any length scale. Geometrical fragmentation can occur on timescales comparable to the growth timescales calculated for density perturbations. It is therefore unclear which mechanism is dominant.

Observations also show prolific fragmentation; Herschel observations have found that $> 75\%$ of low-mass prestellar and protostellar cores are embedded within filaments (Könyves et al., 2015; Marsh et al., 2016). Moreover, those filaments which contain cores are found to be close to, or just above, the critical line density. This suggests that rather than playing only a minor role in star-formation, filaments are central to our understanding of it. Filaments form in the diffuse ISM due to turbulence; gravity then causes the densest of these filaments to grow in mass until they reach the critical line-density; at this point the filament then fragments into a chain of cores which go on to form stars. An understanding of the fragmentation process is key to understanding the properties of cores and the stars they form.

Unfortunately previous theoretical work has been limited to equilibrium and near-equilibrium cases, unlikely to be the case if one considers the dynamic formation of filaments. This limitation has become apparent with observations of median core spacing in filaments. Herschel observations show a core spacing that is a factor of 4 smaller than the spacing predicted by considering 0.1 pc wide equilibrium self-gravitating filaments (André et al., 2014). Moreover, recent observations of filamentary infra-red dark clouds (IRDCs) have shown a lack of clear periodicity in the core separation (Contreras et al., 2016), or that fragmentation occurs on multiple scales (Kainulainen et al., 2013; Teixeira et al., 2016; Kainulainen et al., 2016a).

1.3 FEEDBACK

The stars formed within molecular clouds have a dramatic effect on their surroundings via a number of different mechanisms. Krumholz et al. (2014) divide feedback mechanisms into three groups: momentum feedback, where the gas is able to rapidly radiate away energy and so the feedback mechanism works by injecting momentum into the system, e.g. protostellar outflows; explosive feedback, where the mechanism heats the gas so quickly that it is unable to cool on a dynamical timescale, and so the hot over-pressured gas expands and does work on the surrounding cloud, e.g. supernovae; and thermal feedback, where the mechanism changes the temperature profile of the surrounding gas without driving large scale flows, e.g. non-ionizing radiation from YSOs.

Explosive mechanisms, such as supernovae, winds and photo-ionizing radiation, impart sufficient energy into the cloud that the gas is dispersed and returns to the warm and hot phases of the ISM. Photo-ionizing radiation is thought to be the most efficient at terminating star formation and destroying the cloud (Whitworth, 1979; Franco, Tenorio-Tagle & Bodenheimer, 1990; Krumholz, 2006; Goldbaum et al., 2011). Recent simulations have shown that even for clouds with significant substructure, ionization is able to disperse the cloud (Walch et al., 2012). However, ionizing radiation may not be able to destroy the most massive clouds, those with escape velocities greater than $\sim 10 \text{ km s}^{-1}$ (Dale & Bonnell, 2011; Dale, Ercolano & Bonnell, 2013). For those clouds supernovae may be necessary to disperse the gas. In this scenario, other feedback processes regulate star formation until the first massive star explodes, depositing 10^{44} J of energy into the cloud and dispersing it (Walch, 2016). Krumholz & Matzner (2009) show radiation pressure is able to drive H II regions more effectively than ionized gas for high escape velocity molecular clouds, and suggest that as supernovae take many dynamical timescales to occur, that radiation-driven H II regions are the dominant feedback mechanism in such clouds.

Whatever the dominant mechanism, feedback plays an important role in regulating star formation and returning gas to the diffuse hot ISM.

1.4 AIM OF THIS THESIS

A valuable technique in modelling is to perform numerous numerical experiments over a wide parameter space. I use the term numerical experiment to refer to a simplified setup designed to study a single problem, as opposed to large scale simulations with numerous physical processes involved. Numerical experiments have

several advantages. The main advantage is that due to their smaller scale one is able to run hundreds of simulations over a wide parameter space in the time it would take to run only a handful of large scale simulations. This is especially important for simulations that include random processes such as turbulence, as the more realisations the better the statistics. The smaller scale of the simulations also means that the resolution of the simulations is better, allowing one to study more detailed sub-structure. Moreover, the simplified setup allows one to more easily disentangle the causes of the effects seen. This technique also has disadvantages: the initial setup may be unrealistic and the formation of structures, such as filaments, may not occur as self-consistently as it would in a larger scale simulation.

This thesis aims to use a series of numerical experiments to investigate:

- How does the global collapse of a filament differ from that of a sphere, and can one produce a free-fall time equation for a filament?
- How is the filamentary fragmentation process influenced by accretion and the fact that the filament is not in equilibrium?
- How does a turbulent velocity field affect the density perturbations within a filament, and the subsequent fragmentation of the filament?

1.4.1 THESIS PLAN

In chapter 2, I give a brief outline of the technique used to perform the majority of the numerical simulations presented here, Smoothed Particle Hydrodynamics (SPH). In chapter 3, I present simulations studying the global longitudinal collapse of filaments, and compare and contrast to previous theoretical work by Pon et al. (2012). In chapter 4, I present a numerical perturbation analysis of accreting filaments, and discuss the resulting dispersion relation in the context of filamentary fragmentation. In chapter 5, I present results from a set of simulations of fragmenting filaments accreting from a turbulent medium, and compare to the results in chapter 4. In chapter 6, I present synthetic images of simulations of accreting filaments and study the fibrous sub-structure. In chapter 7, I summarise the conclusions from this thesis and present plans for future work.

CHAPTER 2

SMOOTHED PARTICLE HYDRODYNAMICS

In this chapter I give a brief overview of numerical hydrodynamics and describe the method used to produce the majority of the simulations presented in this thesis, Smoothed Particle Hydrodynamics (SPH). SPH solves the equations of self-gravitating hydrodynamics by representing a continuous fluid as a set of kernel-smoothed particles. It is a good method for studying the dynamics of self-gravitating gas over a range of densities and length scales, due to its self-adapting spatial resolution and inherent conservation of energy, and linear and angular momentum. I describe the implementation of SPH used by the GANDALF code, which includes gravity and hydrodynamics.

2.1 NUMERICAL HYDRODYNAMICS

Fluids, such as the interstellar medium, are governed by the equations of hydrodynamics. If one considers only hydrodynamical forces and an inviscid fluid, these equations are

$$\frac{d\rho}{dt} \equiv \frac{\partial\rho}{\partial t} + \underline{v} \cdot \nabla\rho = -\rho\nabla \cdot \underline{v}, \quad \text{Continuity equation;} \quad (2.1)$$

$$\rho \frac{d\underline{v}}{dt} \equiv \frac{\partial\rho\underline{v}}{\partial t} + \rho\underline{v} \cdot \nabla\underline{v} = -\nabla P, \quad \text{Momentum equation;} \quad (2.2)$$

$$\frac{du}{dt} \equiv \frac{\partial u}{\partial t} + \underline{v} \cdot \nabla u = -\frac{P}{\rho} \nabla \cdot \underline{v}, \quad \text{Energy equation.} \quad (2.3)$$

This set of equations describes the time evolution of a fluid's density, ρ , velocity, \underline{v} , and specific internal energy, u , at all points in space. Additionally, an equation of state linking the gas' pressure and internal energy with density is needed to solve these equations.

Due to their complexity the hydrodynamical equations can only be solved analytically for a set of very specific flows. Thus, numerical methods must be used if one is to study the behaviour of a non-linear system such as a star formation region. There are numerous different approaches to solving these equations, and many different implementations of each approach. In this chapter I will briefly outline the different approaches used by the star formation community, and then describe the method used to produce the majority of the simulations in this thesis, Smoothed Particle Hydrodynamics (SPH).

2.1.1 EULERIAN GRID CODES

The oldest approach to solving the equations of hydrodynamics is to consider a fluid which moves in a static reference frame. The computational domain is split into a fixed position grid, at each grid point the Eulerian derivatives (i.e. $\partial\rho/\partial t$, $\partial\rho v/\partial t$ and $\partial u/\partial t$) are calculated and integrated. This approach has many advantages: the use of high-order Riemann solvers means that this method quickly converges; shocks are accurately captured without substantial dissipation, and it is able to model hydrodynamical instabilities well. However, there are some disadvantages to using a grid code: such codes cannot adaptively increase the spatial resolution in selected regions of a simulation; angular momentum is not conserved; there exists a preferred direction of travel due to the grid's axes, and there exists an advection error when fluids with large gradients move across grid cells. A solution to the problem of constant resolution everywhere was put forward by Berger & Colella (1989), who introduce a method which adaptively adds and modifies finer grids in regions which require higher spatial resolution. This has become known as adaptive mesh refinement (AMR) and is now used in all major hydrodynamical grid codes.

2.1.2 SPH CODES

An approach developed independently by Lucy (1977) and Gingold & Monaghan (1977) is to use a Lagrangian formulation of the hydrodynamical equations. This assumes a reference frame which moves with a fluid parcel. As such, the fluid is divided into a finite number of discrete particles, each with its own value of density, velocity and specific internal energy. The Lagrangian derivatives (i.e. $d\rho/dt$, $\rho dv/dt$ and du/dt) are calculated and integrated at each particle's position to evolve the fluid. SPH has many advantages, especially when applied to star formation: as the particles are free to move they are not bound to a fixed geometry as grids are; due

to adaptive smoothing lengths the spatial resolution automatically increases in regions of high density, and SPH offers exact and simultaneous conservations of energy as well as linear and angular momentum. There are some disadvantages to using a particle based method: SPH is technically a second order method but if particles are not smoothly distributed its order is reduced; artificial viscosity is needed to handle discontinuities such as shocks due to particle interpenetration, however, it causes excessive diffusion on length scales comparable to the smoothing length; and there exists a "surface-tension" error which suppresses fluid mixing.

2.1.3 MOVING-MESH CODES

Moving-mesh, or tessellation, codes are more recent inventions which inherit many of the advantages of both grid and particle codes. Moving-mesh codes use particles to represent the fluid, as in SPH, and then build a Voronoi tessellation around these particles, creating a non-regular grid system, which determines how neighbouring fluid cells interact. Thus, these codes are quasi-Lagrangian and so adaptively increase resolution in high density regions, and they do not have a fixed geometry or preferred directions like grid codes. Due to the fact they use a finite-volume Godunov method, like standard grid codes, they capture shocks and other fluid instabilities well, and do not need artificial diffusion terms. However, because of the novelty of moving-mesh codes, the disadvantages are yet to be fully determined. This method does not conserve angular momentum, and mesh-deformation (i.e. highly irregular grid shapes in complicated flows) is likely to lead to reduced convergence and possibly increased errors in such regions.

2.2 BASIC PRINCIPLES OF SPH

As mentioned above, SPH represents a fluid by using a finite number, \mathcal{N} , of particles with mass m_i . The properties of each particle are smoothed over a kernel so that all quantities are continuous. Thus the value of a continuous property, A , at a point \underline{r} is given by

$$\langle A(\underline{r}) \rangle = \int_V A(\underline{r}') W(\underline{r} - \underline{r}', h) dV, \quad (2.4)$$

where W is the kernel function which has a length scale of h , the smoothing length. Any function may be used as the kernel function as long as it satisfies two conditions. First, the smoothing kernel must be normalised such that its volume integral is equal to unity,

$$\int_V W(\underline{r} - \underline{r}', h) dV = 1. \quad (2.5)$$

Second, the kernel must tend towards a Dirac function as the smoothing length tends towards zero,

$$\lim_{h \rightarrow 0} W(\underline{r} - \underline{r}', h) = \delta(\underline{r} - \underline{r}'). \quad (2.6)$$

As SPH consists of discrete particles, the integral in equation 2.4 is replaced with a summation over the N particles within the smoothing kernel,

$$\langle A(\underline{r}_i) \rangle = \sum_{j=1}^N \frac{m_j}{\rho_j} A_j W(\underline{r}_{ij}, h), \quad (2.7)$$

where $\underline{r}_{ij} \equiv \underline{r}_i - \underline{r}_j$. The gradient of the scalar A is given by

$$\langle \nabla A(\underline{r}_i) \rangle = \sum_{j=1}^N \frac{m_j}{\rho_j} A_j \nabla W(\underline{r}_{ij}, h). \quad (2.8)$$

One can extend this to vector quantities. The divergence of the vector \underline{B} is given by

$$\langle \nabla \cdot \underline{B}(\underline{r}_i) \rangle = \sum_{j=1}^N \frac{m_j}{\rho_j} \underline{B}_j \cdot \nabla W(\underline{r}_{ij}, h). \quad (2.9)$$

And the curl is given by

$$\langle \nabla \times \underline{B}(\underline{r}_i) \rangle = \sum_{j=1}^N \frac{m_j}{\rho_j} \underline{B}_j \times \nabla W(\underline{r}_{ij}, h). \quad (2.10)$$

This is useful as the commonly used kernel functions have well-known analytical functions as their gradients, reducing the computational cost.

Note that the volume element, dV , in equation 2.4 has been replaced with the approximation m_j/ρ_j in equations 2.7-2.10. This is not the only choice one can make, Saitoh & Makino (2013) use U_j/q_j , where U_j is the internal energy of the particle and q_j is the energy density. For the remainder of the chapter I will use the traditional density term as this is the default in GANDALF.

2.2.1 SMOOTHING KERNEL

Many kernels have been used since the invention of SPH, the original formulation by Lucy (1977) used a Gaussian smoothing kernel. The most widely used

kernel for modern SPH codes, and the one used in this work, is the M4 spline kernel (Monaghan & Lattanzio, 1985). In three dimensions it is given by

$$W(s) = \frac{1}{\pi h^3} \begin{cases} 1 - \frac{3}{2}s^2 + \frac{3}{4}s^3 & \text{if } 0 \leq s \leq 1; \\ \frac{1}{4}(2-s)^3 & \text{if } 1 \leq s \leq 2; \\ 0 & \text{if } s > 2 \end{cases}, \quad (2.11)$$

where $s \equiv |r_{ij}|/h$. The first spatial derivative is

$$\frac{dW}{dr}(s) = \frac{1}{\pi h^4} \begin{cases} 3s - \frac{9}{4}s^2 & \text{if } 0 \leq s \leq 1; \\ \frac{3}{4}(2-s)^2 & \text{if } 1 \leq s \leq 2; \\ 0 & \text{if } s > 2 \end{cases}. \quad (2.12)$$

The M4 kernel is popular because it is compact, it only extends out to $2h$; this is an improvement over the first Gaussian smoothing kernels which have an infinite extent. Gas properties such as pressure or density are local properties and should not be smoothed over the whole fluid as they are with infinite kernels. Moreover, it is computationally expensive to sum over the contributions from every particle in the simulation.

2.3 SMOOTHING LENGTH

The choice of smoothing length, h , is very important as it affects the resolution of the simulation as well as the accuracy of the equations. Features smaller than the smoothing length will be smoothed out and diluted, thus the smoothing length is in effect the resolution limit in SPH. Furthermore, the smoothing length controls the number of particles within the smoothing kernel, a larger smoothing length means more ‘neighbours’ and less noise as the summation (equation 2.7) better approximates the continuum integral (equation 2.4). Unfortunately, large smoothing lengths can lead to the ‘pair instability’. SPH particles are kept from coming too close to each other due to pressure; however, the inner region of the smoothing kernel has a very small gradient which leads to particles becoming ‘trapped’ if they are very close each other. Price (2012) show that for the M4 spline kernel, one can not exceed ~ 65 neighbours in three dimensions without pairing occurring. Thus one wishes to have a smoothing length small enough to resolve density structures, large enough so as not to cause excessive noise but not too large as to cause the ‘pair instability’ to occur.

The first SPH simulations used global smoothing lengths based on the average particle spacing. This was unsatisfactory as it did not adequately resolve dense,

collapsing regions and overly resolved diffuse regions. Monaghan (2002) suggests that each particle should have an individual smoothing length and that it should be a function of density,

$$h_i = \eta \left(\frac{m_i}{\rho_i} \right)^{1/3}. \quad (2.13)$$

The value of η is used to determine the average number of neighbours per particle, using the M4 kernel in three dimensions, the default value $\eta = 1.2$ leads to an average particle having 58 neighbours (Price & Monaghan, 2004).

The particle density, ρ_i , is given by equation 2.7 and is therefore dependent on the smoothing length. Thus the value of h_i is found by iteration; given an initial estimate of h_i a density is found, this density is put into equation 2.13 to find a new smoothing length. This is repeated until the change in h_i is less than $\sim 1\%$. The use of an adaptive smoothing length linked to density means that one has higher resolution in the high density collapsing regions, useful for star formation simulations.

2.4 THE HYDRODYNAMICAL EQUATIONS IN SPH

The equations of hydrodynamics, given in section 2.1, are written in their continuum form. These must be converted into a "smoothed" version using SPH quantities. An SPH equivalent for the continuity equation (equation 2.1) is unnecessary as SPH automatically conserves mass due to the use of fixed-mass particles. The SPH equivalents of the momentum and energy equations must be symmetric such that the forces between a pair of particles are equal and opposite and momentum and energy are simultaneously conserved. This can be done by substituting the identity

$$\frac{\nabla A}{\rho} = \nabla \left(\frac{A}{\rho} \right) + \frac{A}{\rho^2} \nabla \rho, \quad (2.14)$$

and equation 2.7 into the momentum equation (2.2) to give

$$\frac{dv_i}{dt} = - \sum_{j=1}^N m_j \left(\frac{P_i}{\rho_i^2} + \frac{P_j}{\rho_j^2} \right) \nabla_i W(r_{ij}, h_i). \quad (2.15)$$

The energy equation is calculated by substituting the continuity equation (equation 2.1) into equation 2.3, which gives

$$\frac{du_i}{dt} = \frac{P_i}{\rho_i^2} \frac{d\rho_i}{dt}, \quad (2.16)$$

or,

$$\frac{du_i}{dt} = \frac{P_i}{\rho_i^2} \sum_{j=1}^N m_j \underline{v}_{ij} \cdot \nabla_i W(\underline{r}_{ij}, h_i), \quad (2.17)$$

where $\underline{v}_{ij} \equiv \underline{v}_i - \underline{v}_j$.

2.4.1 EQUATION OF STATE

To fully simulate the interstellar medium (ISM) one must include radiation transport. The ISM is heated by numerous mechanisms, e.g. the background interstellar radiation field, heating from nearby stars, compressional heating, molecule formation heating and cosmic rays. It is also cooled by radiative de-excitation of atoms, ions and molecules as well as dust radiation. Modelling these processes is computationally expensive and so one often approximates the thermal properties of the gas by using an equation of state. The equation of state of a fluid links the pressure and the temperature to the density and internal energy.

Gas in the ISM is optically thin over a wide range of densities. This allows the gas to reach an equilibrium temperature, predominately set by the background radiation and the emission of the gas. Thus one can write an isothermal equation of state

$$T(\rho, u) = T_{\text{O}}, \quad P(\rho, u) = \frac{\rho k_B T_{\text{O}}}{\bar{m}}, \quad (2.18)$$

where \bar{m} is the mean gas particle mass. From observations it has been determined that $T_{\text{O}} \sim 10$ K.

However, the isothermal equation of state is only true when the gas is optically thin and can rapidly radiate away the energy it gains from heating processes. As gas gravitationally collapses and its density increases the gas becomes optically thick and switches to being approximately adiabatic. Thus one can write a barotropic equation of state

$$T(\rho, u) = T_{\text{O}} \left(1 + \left(\frac{\rho}{\rho_{\text{BARO}}} \right)^{2/3} \right), \quad P(\rho, u) = \frac{\rho k_B T_{\text{O}}}{\bar{m}} \left(1 + \left(\frac{\rho}{\rho_{\text{BARO}}} \right)^{2/3} \right), \quad (2.19)$$

where $\rho_{\text{BARO}} \sim 10^{-13} \text{ g cm}^{-3}$ is the density at which the gas switches from being approximately isothermal to approximately adiabatic (Masunaga, Miyama & Inutsuka, 1998; Masunaga & Inutsuka, 2000).

2.5 ARTIFICIAL VISCOSITY

The equations laid out above are completely inviscid. The lack of a viscous term causes post-shock oscillations to occur behind a shock front, an unphysical feature. Moreover, in a high Mach-number flow the particles may penetrate each other and pass through, unaffected by the shock. Thus, SPH requires an artificial viscosity term to ensure that shocks are adequately captured. Monaghan (1997) introduces a viscosity based term to the momentum equation,

$$\left. \frac{d\mathbf{v}_i}{dt} \right|_{\text{VISC}} = - \sum_{j=1}^N m_j \Pi_{ij} \nabla_i \bar{W}(\mathbf{r}_{ij}, h_i, h_j), \quad (2.20)$$

where

$$\bar{W}(\mathbf{r}_{ij}, h_i, h_j) = \frac{W(\mathbf{r}_{ij}, h_i) + W(\mathbf{r}_{ij}, h_j)}{2}, \quad (2.21)$$

and

$$\Pi_{ij} = \begin{cases} -\frac{\alpha v_{\text{SIG}} \mathbf{v}_{ij} \cdot \mathbf{r}_{ij}}{\bar{\rho}_{ij} |\mathbf{r}_{ij}|} & \text{if } \mathbf{v}_{ij} \cdot \mathbf{r}_{ij} \leq 0; \\ 0 & \text{if } \mathbf{v}_{ij} \cdot \mathbf{r}_{ij} > 0. \end{cases} \quad (2.22)$$

Here $\bar{\rho}_{ij} = (\rho_i + \rho_j)/2$ and v_{SIG} is the signal velocity given by

$$v_{\text{SIG}} = c_i + c_j - \beta \frac{\mathbf{v}_{ij} \cdot \mathbf{r}_{ij}}{|\mathbf{r}_{ij}|}, \quad (2.23)$$

where c_i is the isothermal sound speed of particle i .

This viscosity term will cause the dissipation of kinetic energy and so heats the gas, adding a term to the energy equation

$$\left. \frac{du_i}{dt} \right|_{\text{VISC}} = \sum_{j=1}^N m_j \Lambda_{ij} \hat{\mathbf{r}} \cdot \nabla_i \bar{W}(\mathbf{r}_{ij}, h_i, h_j), \quad (2.24)$$

where

$$\Lambda_{ij} = \begin{cases} -\frac{\alpha v_{\text{SIG}} (\mathbf{v}_{ij} \cdot \mathbf{r}_{ij})^2}{2\bar{\rho}_{ij} |\mathbf{r}_{ij}|^2} & \text{if } \mathbf{v}_{ij} \cdot \mathbf{r}_{ij} \leq 0; \\ 0 & \text{if } \mathbf{v}_{ij} \cdot \mathbf{r}_{ij} > 0. \end{cases} \quad (2.25)$$

This introduces two terms, α and β which handle artificial viscosity in low and high Mach-number regions respectively. Monaghan (1997) suggests the values of $\alpha = 1$ and $\beta = 2$. Morris & Monaghan (1997) reduce the parameters by setting $\beta \equiv 2\alpha$, this simplification is used in this work.

2.5.1 TIME-DEPENDENT ARTIFICIAL VISCOSITY

The Monaghan (1997) artificial viscosity term works well with planar shocks but also generates an additional shear viscosity which can transport angular momentum in an unphysical manner. Morris & Monaghan (1997) develop a time-dependent artificial viscosity scheme to mitigate the problem of artificial shear viscosity.

Each SPH particle is assigned its own viscosity parameter α_i , instead of the global value, $\alpha = 1$. For each particle, α_i evolves according to

$$\frac{d\alpha_i}{dt} = \frac{\alpha_{\text{MIN}} - \alpha_i}{\tau_i} + S_i, \quad (2.26)$$

where α_{MIN} is the user specified minimum value of α_i , τ_i is the timescale on which α_i decays defined as $\tau_i \equiv 10h_i/c_i$ and S_i is a source term. Rosswog et al. (2000) give the source term as

$$S_i = (\alpha_{\text{MAX}} - \alpha_{\text{MIN}}) \begin{cases} -\nabla \cdot \underline{v}_i & \text{if } \nabla \cdot \underline{v}_i \leq 0; \\ 0 & \text{if } \nabla \cdot \underline{v}_i > 0. \end{cases} \quad (2.27)$$

This scheme ensures that in shocked regions $\alpha_i \rightarrow \alpha_{\text{MAX}} = 1$ and in pre/post-shocked regions $\alpha_i \rightarrow \alpha_{\text{MIN}} = 0.1$. The value of α used in equations 2.20 and 2.24 is replaced by $\alpha_{ij} = (\alpha_i + \alpha_j)/2$.

2.6 GRAVITY

Self-gravitating fluids require an additional term to be added to the momentum equation (equation 2.15) which describes the gravitational acceleration due to the other particles

$$\left. \frac{d\underline{v}_i}{dt} \right|_{\text{GRAV}} = - \sum_{j=1}^{\mathcal{N}} \frac{Gm_j \hat{\underline{r}}_{ij}}{|\underline{r}_{ij}|^2}. \quad (2.28)$$

Unlike hydrodynamical forces which are local and whose contributions are calculated only for those particles which lie inside the smoothing kernel, gravity has an infinite range and so requires a summation over all \mathcal{N} particles in the simulation. This is computationally expensive for the large number of particles in modern simulations, and therefore modern codes use a tree to determine which particles must be considered exactly and which may be approximated.

2.6.1 TREE GRAVITY

Most SPH codes use either the Barnes-Hut octal tree (Barnes & Hut, 1986) or a binary tree to efficiently calculate the gravitational acceleration experienced by each particle. Trees are data structures that consist of cells, these cells contain information as well as pointers to *child* cells. In the context of SPH simulations, the cells are spatial regions of the computational domain and contain the IDs of the particles which lie inside them; the children that a cell points to are the regions which the parent cell may be divided into. Construction of a binary tree begins by considering the entire computational domain as the *root cell* of the tree. The root cell is divided into two child cells which contain an equal number of particles. This division is continued until the number of particles in a cell is less than some pre-defined maximum. When a cell does not need to be divided it is called a *leaf* cell. Thus construction stops when all particles are contained within a leaf cell. This leads to dense regions of the fluid containing spatially small cells, while diffuse regions contain spatially large cells.

The total gravitational acceleration on a particle is calculated using a process called ‘walking the tree’, this reduces the direct summation that scales as $\mathcal{O}(\mathcal{N}^2)$ to a process that scales as $\mathcal{O}(\mathcal{N} \log \mathcal{N})$. Walking the tree means that instead of considering the contribution from each individual particle one considers the contribution from each cell in the tree. If a cell is sufficiently far away from a particle, then its contribution to the gravitational acceleration may be approximated by replacing all the particles within the cell with a point mass, equal to the sum of the particle masses, at the centre of mass of the cell. If the cell is too close then it is ‘opened’ and its child cells are considered. If a leaf cell is reached and it can not be approximated as a point mass then the particles inside the leaf cell are considered individually. For a cell to be approximated as a point mass, the angle it subtends must be smaller than a pre-defined opening angle, θ_{MAX} . If a cell has a size, s , and is at a distance, d , from the particle then the cell may be approximated as a point mass if

$$\frac{s}{d} \leq \theta_{\text{MAX}}. \quad (2.29)$$

The smaller the maximum opening angle the more cells will be opened and the acceleration calculated by walking the tree will approach the exact acceleration (equation 2.28).

The centre of mass approximation may be improved by considering the quadrupole tensor of the cell,

$$\mathbf{Q}_{ab} = \sum_{j=1}^{\mathcal{M}} m_j (3r_{a,j}r_{b,j} - r_j^2 \delta_{ab}), \quad (2.30)$$

where \mathcal{M} is the number of particles in the cell, \underline{r} is the position vector with an origin at the cell's centre of mass, and δ is the Kronecker delta. The gravitational acceleration felt by particle i due to cell k is given then by

$$\underline{a}_{\text{GRAV}} = -\frac{Gm_k}{|\underline{R}_{ik}|^2}\hat{R}_{ik} + \frac{G}{|\underline{R}_{ik}|^4}\mathbf{Q}_k \cdot \hat{R}_{ik} - \frac{5G(\hat{R}_{ik} \cdot \mathbf{Q}_k \cdot \hat{R}_{ik})}{2|\underline{R}_{ik}|^4}\hat{R}_{ik}, \quad (2.31)$$

where \underline{R}_{ik} is the distance between particle i and the centre of mass of cell k .

2.6.2 KERNEL-SOFTENED GRAVITY

When the gravitational acceleration is calculated between neighbours the fact that the particles are smoothed must be taken into account. If a pair of neighbouring particles are a distance r apart, then only the mass interior to r must be considered. The mass interior to r is given by

$$M(< r) = \int_0^r 4\pi r'^2 \rho(r') dr' = m \int_0^r 4\pi r'^2 W(r', h) dr' = mW'(r/h) \quad (2.32)$$

For the M4 spline, $W'(r/h)$ is

$$W'(s) = \begin{cases} \frac{4}{3}s^3 - \frac{6}{5}s^5 + \frac{1}{2}s^6 & \text{if } 0 \leq s \leq 1; \\ \frac{8}{3}s^3 - 3s^4 + \frac{6}{5}s^5 - \frac{1}{6}s^6 - \frac{1}{15} & \text{if } 1 \leq s \leq 2; \\ 1 & \text{if } s > 2, \end{cases} \quad (2.33)$$

where $s \equiv r/h$. Thus the gravitational acceleration of particle i due to the neighbouring particle j is given by

$$\underline{a}_{\text{GRAV},ij} = -\frac{Gm_j W'(r_{ij}, h_{ij})}{|\underline{r}_{ij}|^2} \hat{r}_{ij} \quad (2.34)$$

Whitworth (1998) show that a useful consequence of kernel-softened gravity is that it prevents the creation of sub-Jeans condensations due to numerical effects as long as the Jeans mass is resolved.

2.6.3 PERIODIC GRAVITY

It is common to simulate a small portion of an infinite or extended medium by assuming that the whole medium consists of an infinite number of replicas of the computational domain. This is achieved by using periodic wrapping at the boundaries

of the computational domain to calculate the local hydrodynamic forces, and by using the Ewald method to determine the gravitational acceleration due to particles in the replicated computational domains (Hernquist, Bouchet & Suto, 1991; Klessen, 1997). If the computational domain is a cube with sides of length L , the gravitational acceleration on particle i due to all of the infinite replicas of particle j is

$$\underline{a}_{\text{EWALD},j} = -Gm_j \left(\underline{f}(\underline{r}_{ij}) + \frac{\hat{\underline{r}}_{ij}}{|\underline{r}_{ij}|^2} \right), \quad (2.35)$$

where

$$\begin{aligned} \underline{f}(\underline{r}) = & - \sum_{\underline{n}} \frac{\underline{r} - \underline{n}L}{|\underline{r} - \underline{n}L|^3} \left[\text{erfc}(\alpha|\underline{r} - \underline{n}L|) + \frac{2\alpha}{\sqrt{\pi}} |\underline{r} - \underline{n}L| \exp(-\alpha^2|\underline{r} - \underline{n}L|^2) \right] \\ & - \frac{1}{L^3} \sum_{\underline{k}} \frac{4\pi\underline{k}}{|\underline{k}|^2} \exp\left(-\frac{|\underline{k}|^2}{4\alpha^2}\right) \sin(\underline{k} \cdot \underline{r}) \end{aligned} \quad (2.36)$$

and $\alpha = 2/L$. The first summation of equation 2.36 is a summation over all replicas in all physical space (\underline{n} -space), and the second summation is over all replicas in all phase space (\underline{k} -space). For computational reasons, the correction function \underline{f} is computed for a wide range of separations, \underline{r} , and stored in a look-up table before the start of the simulation. GANDALF also includes a modified version of the Ewald method as described in Wunsch et al. in prep. This modified Ewald method allows one to include periodic effects in only one direction of a three dimensional simulation.

2.7 INTEGRATION SCHEMES

The equations of hydrodynamics (equations 2.15 and 2.17) with the additional gravitational and viscosity terms (equations 2.28 and 2.20) are numerically integrated each timestep. If one uses an equation of state then the energy equation (equation 2.17) does not need to be integrated. This work uses the the second-order Leapfrog drift-kick-drift (DKD) scheme as its integrator. The Leapfrog scheme is symplectic and so conserves energy, a desirable property for simulations of self-gravitating material, as orbits would otherwise drift over time.

Advancing particle i from the n^{th} timestep to the $(n+1)^{\text{th}}$ timestep using Leapfrog DKD is given by

$$\underline{r}_i^{n+1/2} = \underline{r}_i^n + \frac{1}{2} \underline{v}_i^n \Delta t_i, \quad (2.37)$$

$$\underline{v}_i^{n+1/2} = \underline{v}_i^n + \frac{1}{2} \frac{d\underline{v}_i}{dt}^{n-1/2} \Delta t_i, \quad (2.38)$$

$$\underline{v}_i^{n+1} = \underline{v}_i^n + \frac{d\underline{v}_i}{dt}^{n+1/2} \Delta t_i, \quad (2.39)$$

$$\underline{r}_i^{n+1} = \underline{r}_i^n + \frac{1}{2}(\underline{v}_i^n + \underline{v}_i^{n+1})\Delta t_i, \quad (2.40)$$

where Δt_i is the time interval separating the two timesteps. This is computationally efficient as it requires only one acceleration calculation per integration timestep.

2.8 TIMESTEPS

The timestep, Δt_i , for each particle must be chosen such that its associated quantities do not change too rapidly and the integrator become unstable. Particle i must have a timestep less than or equal to that given by

$$\Delta t_{\text{MAX},i} = \gamma \text{MIN} \left[\frac{h_i}{h_i |\nabla \cdot \underline{v}_i| + c_i}, \sqrt{\frac{h_i}{|\underline{a}_i| + \epsilon}}, \frac{h_i}{(1 + 1.2\alpha_i)c_i + (1 + 1.2\beta_i)h_i |\nabla \cdot \underline{v}_i|} \right]. \quad (2.41)$$

The first term is the classic Courant-Friedrichs-Lewy (CFL) condition applied to SPH. The second term is to ensure that the speed of the particle does not change significantly between timesteps (ϵ is a small non-zero number used to avoid singularities). The third term is a modified CFL conditions that takes into account artificial viscosity. A value of $\gamma = 0.1$ ensures that timesteps are sufficiently small.

Most modern codes, including GANDALF, use multiple particle timesteps to assign an appropriate timestep to each particle. This is done to reduce computational cost; when using a single global timestep those particles which have a maximum timestep greater than the global timestep will be integrated more times than necessary. Codes such as GANDALF use a binary hierarchy to efficiently give each particle its optimal timestep. A binary hierarchy creates a system of timestep levels; each level has a timestep twice that of the level below it. The lowest level has a timestep equal to the smallest maximum timestep, Δt_{MAX} , in the simulation. Particles are allocated the largest timestep in the heirarchy that is smaller than their maximum timestep given by equation 2.41.

2.9 SINKS

In simulations of self-gravitating gas, regions may become gravitationally unstable and begin to collapse. This leads to very high densities, velocities and accelerations, necessitating very small timesteps. Thus it becomes computational impractical to continue to follow a simulation after the formation of the first dense object. To

overcome this, Bate, Bonnell & Price (1995) introduce the concept of sink particles which replace a dense, gravitationally collapsing region with an unsmoothed point mass. Sink particles experience gravitational forces but do not interact hydrodynamically with the surrounding SPH particles. A sink particle can accrete SPH particles that fall into its accretion radius and are gravitationally bound to it. This significantly improves the computational speed of a simulation and allows one to continue the simulation after the first dense, bound region forms.

2.9.1 SINK CREATION

A number of criteria must be satisfied for a sink particle to be placed in the simulation, this is to ensure that only a gravitationally bound dense region is replaced. If an SPH particle fulfils these criteria it and its neighbours are replaced with a sink particle. Different codes use different criteria to check a region is bound, here I will describe those suggested by Hubber, Walch & Whitworth (2013) as they are the default options in GANDALF, and are well converged.

- The candidate SPH particle must have a density greater than a pre-defined sink creation density, ρ_{SINK} .
- The candidate SPH particle must have the lowest gravitational potential of all of its neighbours, i.e. be the local gravitational potential minimum.
- The candidate SPH particle's smoothing kernel must not overlap with existing sink particles's accretion radii. This prevents overlapping sink particle's forming.
- The candidate SPH particle must have a density greater than ρ_{HILL} , which is given by

$$\rho_{\text{HILL}} = -\frac{3(\underline{r}_{ij} \cdot \underline{a}_{ij})}{\pi G |\underline{r}_{ij}|^2}, \quad (2.42)$$

where \underline{r}_{ij} is the position vector between the candidate SPH particle i and an already existing sink particle j , and \underline{a}_{ij} is the acceleration vector between the two. This criterion allows an extended condensate which already has a sink particle in it to fragment only if the candidate SPH particle is a density peak that dominates the local gravitational field.

I have also developed an additional criterion which mitigates the over-production of sink particles in well-resolved lumpy accretion flows onto an existing sink particle.

To understand this additional criterion, consider a region in an accretion flow that is gravitationally bound, and an SPH particle, i , in it may satisfy all of the standard sink creation criteria. However, if this region is moving towards an existing sink particle, j , it may be accreted by sink j before the region's free-fall time has elapsed. If such a region is replaced with a new sink particle, one would end up with two smaller sink particles where there ought to be only one large sink particle. Thus, a candidate SPH particle's free-fall time must be less than the accretion timescale if it is to be replaced by a sink,

$$\tau_{ff,i} < \frac{|r_{ij}|}{\hat{r}_{ij} \cdot \underline{v}_{ij}}, \quad (2.43)$$

$$\rho_i > \frac{3\pi}{32G} \left(\frac{\hat{r}_{ij} \cdot \underline{v}_{ij}}{|r_{ij}|} \right)^2. \quad (2.44)$$

2.9.2 ACCRETION ONTO SINKS

Traditional sink particles immediately accrete SPH particles that enter their accretion radius. However, this causes two problems. Firstly, the lack of SPH particles inside the accretion radius leads to a steep negative pressure gradient towards the sink, adding an artificial hydrodynamical force. Secondly, sink particles act as sinks of both mass and angular momentum, when an SPH particle is accreted its orbital angular momentum is transferred to the sink particle as spin angular momentum, the sink particle accumulates so much spin that it would never collapse to stellar densities.

Hubber, Walch & Whitworth (2013) propose a method of smooth or regulated accretion which sets out to address these problems. When an SPH particle enters the accretion zone of a sink particle it is not immediately accreted, instead it may be accreted over numerous timesteps. The timescale for accretion is given by

$$\tau_{\text{ACC}} = \tau_{\text{RAD}}^{(1-f)} \tau_{\text{DISC}}^f, \quad (2.45)$$

where

$$f = \text{MIN} \left[\frac{2E_{\text{ROT}}}{|E_{\text{GRAV}}|}, 1 \right]. \quad (2.46)$$

Here E_{ROT} and E_{GRAV} are the net rotational and gravitational energies of all the SPH particles inside the accretion zone. Equation 2.45 comes about by considering the two limiting cases, spherically symmetric purely radial accretion, and purely disc accretion. If the SPH particles in the accretion zone are rotationally supported then $2E_{\text{ROT}}/|E_{\text{GRAV}}| \rightarrow 1$ and $\tau_{\text{ACC}} \rightarrow \tau_{\text{DISC}}$. Conversely if there is little rotation then $2E_{\text{ROT}}/|E_{\text{GRAV}}| \rightarrow 0$ and $\tau_{\text{ACC}} \rightarrow \tau_{\text{RAD}}$.

The amount of mass accreted onto the sink at the end of a timestep of length Δt is

$$\Delta M = M_{\text{SPH}} \left[1 - \exp \left(-\frac{\Delta t}{\tau_{\text{ACC}}} \right) \right], \quad (2.47)$$

where M_{SPH} is the net mass of all the SPH particles in the accretion zone. The accreted mass, ΔM , is removed from the SPH particle which is closest to the sink particle. If the mass of the SPH particle is less than ΔM then the remainder is removed from the second closest SPH particle. This is continued until ΔM is removed from the SPH particles in the accretion zone. This slow leaching of mass from the SPH particles ensures that there are always SPH particles inside the sink's accretion zone, and therefore there are much milder gradients across the accretion radius.

To mitigate the problem of sink particles acting as angular momentum sinks, angular momentum is transferred from the sink particle to the SPH particles in the accretion zone at the end of every timestep. Each SPH particle in the accretion zone is given an impulse proportional to its distance from the rotational axis of the sink particle and the sink particle receives a counter-acting impulse to conserve linear and angular momentum. This simulates the transfer of angular momentum to the material outside the sink due to viscous torques in an accretion disc.

2.10 RESOLUTION

To accurately model star formation one must be able to resolve the Jeans instability (Jeans, 1902). Burkert & Bodenheimer (1993) suggest that the minimum mass that can be resolved in SPH is $M_{\text{MIN}} = \gamma N m$, where N is the mean number of neighbours, m is the mass of a single SPH particle and γ is a numerical factor in the range of 1 – 2. Thus for the Jeans instability to be resolvable, the Jeans mass must be greater than M_{MIN} ,

$$M_{\text{J}} = \sqrt{\frac{\pi^3 a_{\text{o}}^3}{36 G^3 \rho}} \geq \gamma N m = M_{\text{MIN}}. \quad (2.48)$$

If one uses an isothermal equation of state with $T_{\text{o}} = 10 \text{ K}$, and a sink creation density of $\rho_{\text{SINK}} = 10^{-12} \text{ g cm}^{-3}$, then for the Jeans mass to be resolvable at all densities the mass of a single SPH particle must be less than or equal to $\sim 2 \times 10^{-5} M_{\odot}$. If one uses a barotropic equation of state then the minimum Jeans mass will occur at ρ_{BARO} , typically set at $10^{-13} \text{ g cm}^{-3}$, this results in the requirement $m \lesssim 6 \times 10^{-5} M_{\odot}$ if $T_{\text{o}} = 10 \text{ K}$.

2.11 SUMMARY

In this chapter I have given a brief overview of the methods used in the star formation community to solve the equations of hydrodynamics, as well as compare their advantages and disadvantages. I have outlined the principles of Smoothed Particle Hydrodynamics (SPH) and explained how the hydrodynamical, viscous and gravitational forces are calculated in GANDALF's implementation of SPH. I have introduced the concept of sink particles and their uses in numerical star formation.

CHAPTER 3

INVESTIGATING THE GLOBAL COLLAPSE OF FILAMENTS *

In this chapter I present Smoothed Particle Hydrodynamic simulations of cold, uniform-density, self-gravitating filaments, for the purpose of investigating their global longitudinal collapse timescales. These timescales are important because they determine the time available for a filament to fragment locally into cores. A filament is initially characterised by its line-mass, μ_{O} , its radius, R_{O} (or equivalently its density $\rho_{\text{O}} = \mu_{\text{O}}/\pi R_{\text{O}}^2$), and its aspect ratio, A_{O} ($\equiv Z_{\text{O}}/R_{\text{O}}$, where Z_{O} is its half-length). The gas is only allowed to contract longitudinally, i.e. parallel to the symmetry axis of the filament (the z -axis). Pon et al. (2012) have previously considered the global dynamics of such filaments analytically. They conclude that short filaments ($A_{\text{O}} < 5$) collapse along the z -axis more-or-less homologously, on a time-scale $t_{\text{HOM}} \sim 0.44 A_{\text{O}} (G\rho_{\text{O}})^{-1/2}$; in contrast, longer filaments ($A_{\text{O}} > 5$) undergo end-dominated collapse, i.e. two dense clumps form at the ends of the filament and converge on the centre sweeping up mass as they go, on a time-scale $t_{\text{END}} \sim 0.98 A_{\text{O}}^{1/2} (G\rho_{\text{O}})^{-1/2}$.

My simulations do not corroborate these predictions. First, for all $A_{\text{O}} > 2$, the collapse time satisfies a single equation

$$t_{\text{COL}} \sim (0.49 + 0.26A_{\text{O}})(G\rho_{\text{O}})^{-1/2},$$

which for large A_{O} is much longer than the Pon et al. prediction. Second, for all $A_{\text{O}} > 2$, the collapse is end-dominated. Third, before being swept up, the gas immediately ahead of an end-clump is actually accelerated outwards by the gravitational attraction of the approaching clump, resulting in a significant ram pressure on the clumps. For

*The work presented here is published in Clarke & Whitworth, 2015, MNRAS, 449, 1819

high aspect ratio filaments the end-clumps approach an asymptotic inward speed, due to the fact that they are doing work both accelerating and compressing the gas they sweep up.

3.1 INTRODUCTION

The ubiquity of non-spherical structures in molecular clouds (e.g. Schneider & Elmegreen, 1979; Lada, Alves & Lada, 1999; Myers, 2009; André et al., 2010) has led to many papers on the effects of dimensionality on global collapse (e.g. Bastien, 1983; Bastien et al., 1991; Burkert & Hartmann, 2004; Pon, Johnstone & Heitsch, 2011; Toalá, Vázquez-Semadeni & Gómez, 2012; Pon et al., 2012). It has been shown analytically that non-spherical structures collapse on longer timescales than spherical clouds of the same density (e.g. Burkert & Hartmann, 2004; Pon et al., 2012); and this has been corroborated by simulations (e.g. Bastien, 1983; Vázquez-Semadeni et al., 2007). In filaments there are two possible longitudinal collapse modes (i.e. collapse modes parallel to the symmetry axis of the filament): a filament may collapse approximately homologously (hereafter homologous collapse), or clumps may form at the ends and move inwards sweeping up material as they go (hereafter end-dominated collapse; Bastien, 1983).

Recently, Pon et al. (2012) have explored analytically the effect that these two modes have on the freefall collapse time for a uniform filament. During homologous collapse the density of a filament remains approximately uniform but changes with time, so all points within the filament have approximately the same collapse timescale. Pon et al. (2012) calculate that the homologous collapse timescale is

$$t_{\text{HOM}} \simeq 0.44 A_{\text{O}} (G\rho_{\text{O}})^{-1/2}. \quad (3.1)$$

Here ρ_{O} is the initial volume density of the filament, A_{O} is the initial aspect ratio defined as $A_{\text{O}} \equiv Z_{\text{O}}/R_{\text{O}}$, Z_{O} and R_{O} are the filament's half-length and radius respectively.

The exact equation describing the longitudinal acceleration inside a filament is non-linear:

$$a_z = -2\pi G\rho \left(2z - \sqrt{R_{\text{O}}^2 + (Z_{\text{O}} + z)^2} + \sqrt{R_{\text{O}}^2 + (Z_{\text{O}} - z)^2} \right), \quad (3.2)$$

where z is the position along the z -axis. As one can see the non-linear terms become very important at the ends of a filament. Consequently the ends of the filament are accelerated to much greater speeds than in homologous collapse, causing them to sweep up interior matter as they overtake it. Pon et al. (2012) calculate that in this case the collapse time is

$$t_{\text{END}} \simeq 0.98 A_{\text{O}}^{1/2} (G\rho_{\text{O}})^{-1/2}. \quad (3.3)$$

Since the collapse times for the two modes depend on A_o in different ways, Pon et al. (2012) conclude that filaments collapse on whichever is the shorter timescale, i.e. short filaments collapse approximately homologously, on a time-scale given by Eqn. (3.1), and long ones collapse via the end-dominated mode, on a timescale given by Eqn. (3.3). Comparing Eqns. (3.1) and (3.3), they infer that the switch occurs at $A_o \sim 5$.

The two modes should be distinguishable by their kinematics. A short filament collapsing homologously has an approximately linear velocity profile along its long axis, while a long filament collapsing via the end-mode has low inward velocities except at its ends, where the inward velocity increases dramatically.

In this chapter I present numerical simulations of initially uniform filaments, to evaluate their freefall time-scales, and to investigate the collapse-mode dichotomy presented in Pon et al. (2012). In §3.2 I detail the simulation setup and the initial conditions used; in §3.3 I present the results of these simulations; in §3.4 I discuss their significance and support the discussion with a semi-analytical model of the system dynamics; and in §3.5 I summarise my conclusions.

3.2 NUMERICAL SETUP

The simulations presented in this chapter are performed using the smoothed particle hydrodynamics (SPH) code GANDALF (Hubber et al. in prep). The simulations invoke both gravity and hydrodynamics, with an isothermal equation of state. Grad-h SPH (Price & Monaghan, 2004) is implemented, with $\eta = 1.2$, so that a typical particle has ~ 58 neighbours. Although I am interested in freefall collapse, the gas is given a non-zero temperature, $T = 1$ K, in order to capture shocks, and to stop artificial clumping of SPH particles. For molecular gas with solar composition, this results in an isothermal sound speed of 0.07 km s^{-1} . Running identical simulations at different low temperatures produces only small variations in the collapse times, so I am satisfied that $T = 1$ K gives a reasonable approximation to free-fall.

The code is modified so that radial motions are suppressed, i.e. $v_x = v_y = 0$ for all particles. Thus, the longitudinal collapse of a cylindrical cloud with super-critical line mass can be simulated without it collapsing radially. Such a constraint has no effect on the longitudinal motion of the gas and allows the simulations to conform to the constant radius condition adopted by Pon et al. (2012).

The boundary conditions are open in all directions. This has no effect in the radial direction as it is ensured that $v_x = v_y = 0$. It has little effect in the longitudinal direction due to the very low temperature causing very little outward pressure.

A hexagonal close-packed grid of particles is used to produce a uniform density. The grid is rotated around the 3 axes by random angles to ensure that the grid's symmetry axes are not aligned with the Cartesian axes, and a cylindrical filament is then cut from this grid. The initial conditions are characterised by

- A_o , the aspect ratio of the filament;
- μ_o , the mass per unit length of the filament; and
- R_o , the radius of the filament.

A_o is varied between 1 and 20. A filament is defined as a structure with an aspect ratio of at least 3 (e.g. Panopoulou et al., 2014); aspect ratios below this value are only simulated for completeness. μ_o is varied between $2 M_\odot \text{ pc}^{-1}$ and $50 M_\odot \text{ pc}^{-1}$. R_o is varied between 0.05 pc and 0.15 pc. This results in a range of initial volume densities, from $2 \times 10^{-21} \text{ g cm}^{-3}$ to $4 \times 10^{-19} \text{ g cm}^{-3}$.

Much of our discussion will consider two fiducial cases: a high aspect ratio case characterised by $A_o = 10$, $\mu_o = 10 M_\odot \text{ pc}^{-1}$ and $R_o = 0.1 \text{ pc}$ and a low aspect ratio case characterised by $A_o = 3$, $\mu_o = 10 M_\odot \text{ pc}^{-1}$ and $R_o = 0.1 \text{ pc}$.

The simulations are all run with the same initial volume-density of SPH particles, $n_{\text{SPH}} \simeq 800,000 \text{ pc}^{-3}$, to ensure that they have comparable spatial resolution, $\sim 0.01 \text{ pc}$; the mass resolution therefore varies between $0.008 M_\odot$ and $0.20 M_\odot$. For reference, a volume-density of SPH particles of $n_{\text{SPH}} \simeq 800,000 \text{ pc}^{-3}$ means that the high aspect ratio fiducial simulation has $\sim 50,000$ particles. Having comparable spatial resolution (rather than comparable mass resolution) is appropriate since I am concerned here with the longitudinal density- and velocity-profiles (rather than fragmentation into condensations). To check convergence, I repeated three simulations with $n_{\text{SPH}} \simeq 2,400,000 \text{ pc}^{-3}$; the resulting collapse times, density- and velocity-profiles differ by $< 1\%$. I therefore believe that $n_{\text{SPH}} \simeq 800,000 \text{ pc}^{-3}$ delivers sufficiently high resolution. I also simulate the high aspect fiducial case ($A_o = 10$, $\mu_o = 10 M_\odot \text{ pc}^{-1}$, $R_o = 0.1 \text{ pc}$) using a different SPH code (SEREN; Hubber et al., 2011), and obtain almost identical results, so I am confident in the fidelity of the simulations.

3.3 RESULTS

For all aspect ratios, $2 < A_o < 20$, all line-densities, $2 M_\odot \text{ pc}^{-1} < \mu_o < 50 M_\odot \text{ pc}^{-1}$, and all radii, $0.05 \text{ pc} < R_o < 0.15 \text{ pc}$, the global collapse of the filament is end-dominated. The ends experience the highest acceleration, and this leads to the formation of end-clumps which then converge on the centre, sweeping up material as

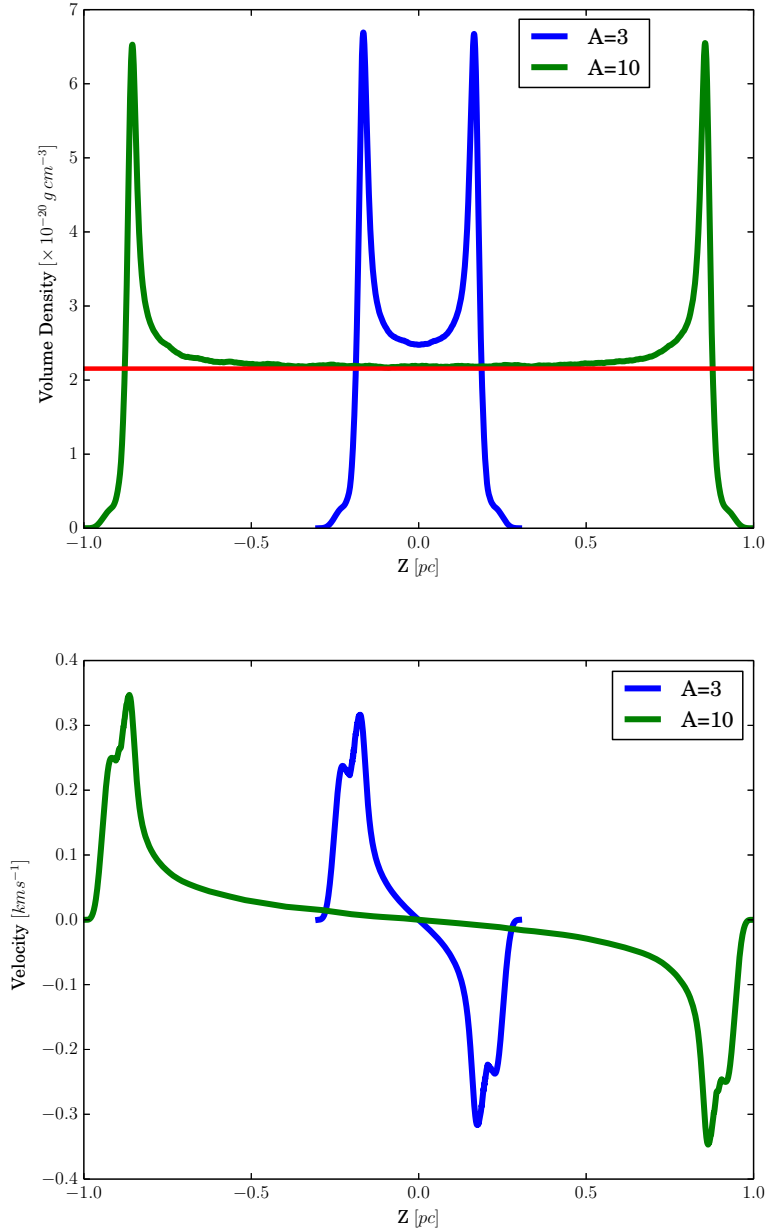


Figure 3.1. (a) The volume-density profile, and (b) the velocity profile, along the z -axis at time $t = 0.55$ Myr, from the simulations of filaments having $\mu_{\text{O}} = 10 M_{\odot} \text{ pc}^{-1}$, $R_{\text{O}} = 0.1$ pc and $A_{\text{O}} = 3$ (blue lines) or $A_{\text{O}} = 10$ (green lines). The signatures of end-dominated collapse are clearly seen in both, viz. strong density peaks and supersonic inwards motions at the extremes, representing the end-clumps that dominate the dynamics. The horizontal red line in figure (a) is the initial volume density; interior material is relatively unaffected by the collapse until the density peaks reach it.

they go. Fig. 3.1 shows the density and velocity profiles along the z -axis, for both the high and low aspect ratio fiducial cases. The dense end-clumps and their supersonic inward velocities are clearly seen.

In all the simulations, I estimate the collapse time, t_{COL} , by identifying the moment when the two converging end-clumps merge, i.e. when there is a single central density maximum at $z = 0$. This is comparable to definition of the collapse time in Pon et al. (2012). They define the collapse time as the time it takes for material that is initially at the filament's end, Z_{O} , reaches $z = 0$.

The filled circles on Fig. 3.2a show values of t_{COL} obtained with different A_{O} , when μ_{O} and R_{O} are fixed at their fiducial values. The filled circles on Fig. 3.2b show values of t_{COL} obtained with different μ_{O} , when A_{O} and R_{O} are fixed at their high aspect ratio fiducial values. The filled circles on Fig. 3.2c show values of t_{COL} obtained with different R_{O} , when A_{O} and μ_{O} are fixed at their high aspect ratio fiducial values. The blue continuous curves show that all these results are well fitted with

$$t_{\text{COL}} = (0.49 + 0.26A_{\text{O}}) (G\rho_{\text{O}})^{-1/2}, \quad (3.4)$$

where $\rho_{\text{O}} = \mu_{\text{O}}/\pi R_{\text{O}}^2$ — and hence they are not well fitted with the relations derived by Pon et al. (2012) (i.e. Eqn. 3.1 for $A_{\text{O}} < 5$, and Eqn. 3.3 for $A_{\text{O}} > 5$).

Equation 3.4 is found using a least-square fitting algorithm on the high aspect ratio data. The fitting parameters have errors: 0.49 ± 0.03 and 0.26 ± 0.00 to 2 significant figures.

Figure 3.3 compares the collapse times obtained from simulations with $R_{\text{O}} = 0.1 \text{ pc}$, $\mu_{\text{O}} = 35 \text{ M}_{\odot} \text{ pc}^{-1}$ or $\mu_{\text{O}} = 50 \text{ M}_{\odot} \text{ pc}^{-1}$, and a range of values for A_{O} (filled circles) with the predictions of Eqn. (3.4; continuous green and blue lines). Again the agreement is very good.

3.4 DISCUSSION

The gravitational acceleration felt by particles off the symmetry axis is lower than that felt by those on the axis, an effect I discuss below in §3.4.1. This results in a curved end-clump, the portion of the end-clump on the axis being roughly 0.01 pc ahead of the end-clump off axis. To determine the velocity of the end-clump, we locate the highest-density SPH particle that is at least 0.04 pc off axis, and then average the velocity of all the SPH particles within $z \pm 0.02 \text{ pc}$ of this particle. By selecting a SPH particle off axis we are able to avoid the atypical central region and locate the end-clump more accurately. The resulting velocity is insensitive to the precise choice

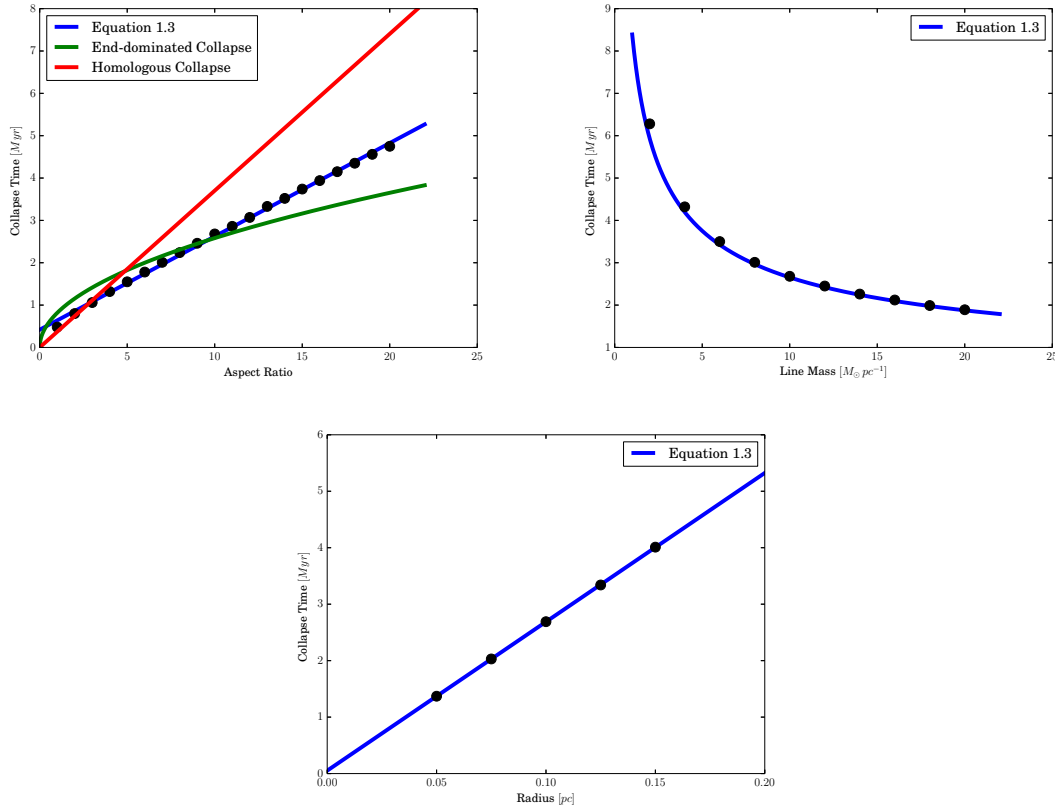


Figure 3.2. The filled circles show values of the collapse time, t_{COL} , obtained when (a) the aspect ratio, A_{O} , is varied and μ_{O} and R_{O} are fixed at their fiducial values; (b) the line-density, μ_{O} , is varied and A_{O} and R_{O} are fixed at their high aspect ratio fiducial values; (c) the radius, R_{O} , is varied and A_{O} and μ_{O} are fixed at their high aspect ratio fiducial values. The high aspect ratio fiducial values are $A_{\text{O}} = 10$, $\mu_{\text{O}} = 10 M_{\odot} \text{pc}^{-1}$, and $R_{\text{O}} = 0.1 \text{pc}$. The blue continuous lines are the predictions of Eqn. (3.4). The red and green lines are the predictions from Pon et al. (2012) (Eqns. 3.1 and 3.3 respectively)

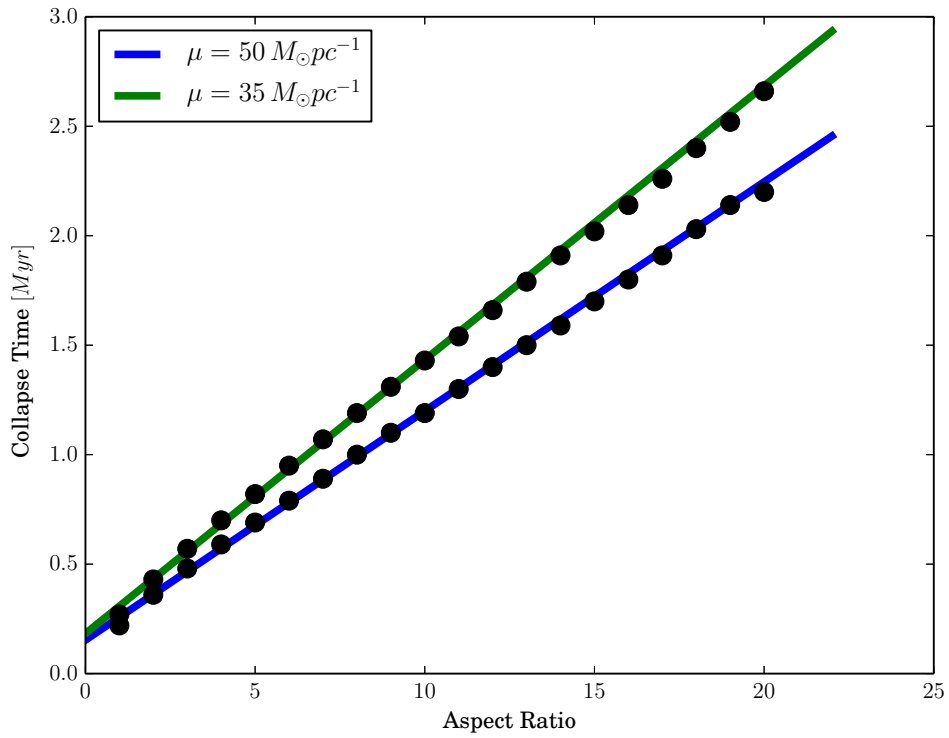


Figure 3.3. The filled circles show values of the collapse time, t_{COL} , obtained with different aspect ratios, A_{O} , when the radius, R_{O} , is fixed at 0.1 pc , and the line-density is fixed at $\mu_{\text{O}} = 35 M_{\odot} \text{ pc}^{-1}$ or $\mu_{\text{O}} = 50 M_{\odot} \text{ pc}^{-1}$. The continuous lines are the predictions of Eqn. 3.4 with $\rho_{\text{O}} = \mu_{\text{O}}/\pi R_{\text{O}}^2$.

of ± 0.02 pc and of 0.04 pc as the off axis requirement.

Fig. 3.4 shows the velocity of the $z > 0$ end-clump as a function of time, for the four filaments with initial line-density $\mu_o = 10 M_\odot \text{pc}^{-1}$, radius $R_o = 0.1$ pc and initial aspect ratios, $A_o = 3, 5, 10,$ and 20 . The velocity profiles are roughly independent of aspect ratio. For large values of A_o a terminal velocity is reached before the filament has time to fully collapse.

A terminal velocity arises because, once an end-clump becomes sufficiently massive, it starts to dominate the gravitational field experienced by the gas just ahead of it, and so this gas flows outwards to meet the end-clump (see Fig. 3.5a). This means that more work has to be done reversing the velocity of the swept-up gas, *and* the swept-up gas is more strongly compressed, so more work is done on it. The upshot is that less gravitational potential energy gets converted into kinetic energy, basically just enough to accelerate the newly swept-up gas up to the terminal velocity. This is illustrated in Fig. 3.6, where I plot, for the simulations with the high and low aspect ratio fiducial parameters ($R_o = 0.1$ pc, $\mu_o = 10 M_\odot \text{pc}^{-1}$ and $A_o = 3$ or $A_o = 10$), the evolution of the net kinetic energy and the net work done. At early times, the kinetic energy grows fastest, but once the terminal velocity has been reached for the $A_o = 10$ case, around ~ 1 Myr, work done takes over, and the kinetic energy increases roughly linearly with time, due to the roughly linear increase in the mass of the end-clumps as they sweep in at constant velocity. One can see this acceleration in growth of work done for the $A_o = 3$ case, but it is overshadowed by the sudden increase at ~ 1.1 Myr when the end-clumps merge in the centre. The same dynamics are present, the end-clump gains enough mass to dominate the gravitational field in its vicinity and the gas just ahead of it begins to move outwards to meet it.

3.4.1 SEMI-ANALYTICAL MODEL

As well as considering the system in terms of energy, one can also develop a semi-analytical model on the basis of the forces involved. A terminal velocity is reached, for high aspect ratio filaments, because the gravitational force on the end-clump is approximately balanced by the force of ram-pressure due to the end-clump sweeping up the outward moving interior material. The net acceleration of the end-clump is therefore

$$\frac{d^2z}{dt^2} = -\alpha (2\pi G \rho_o R_o) + \frac{\rho_o \Delta v_{\text{REL}}^2 \pi R_o^2}{M(t)}. \quad (3.5)$$

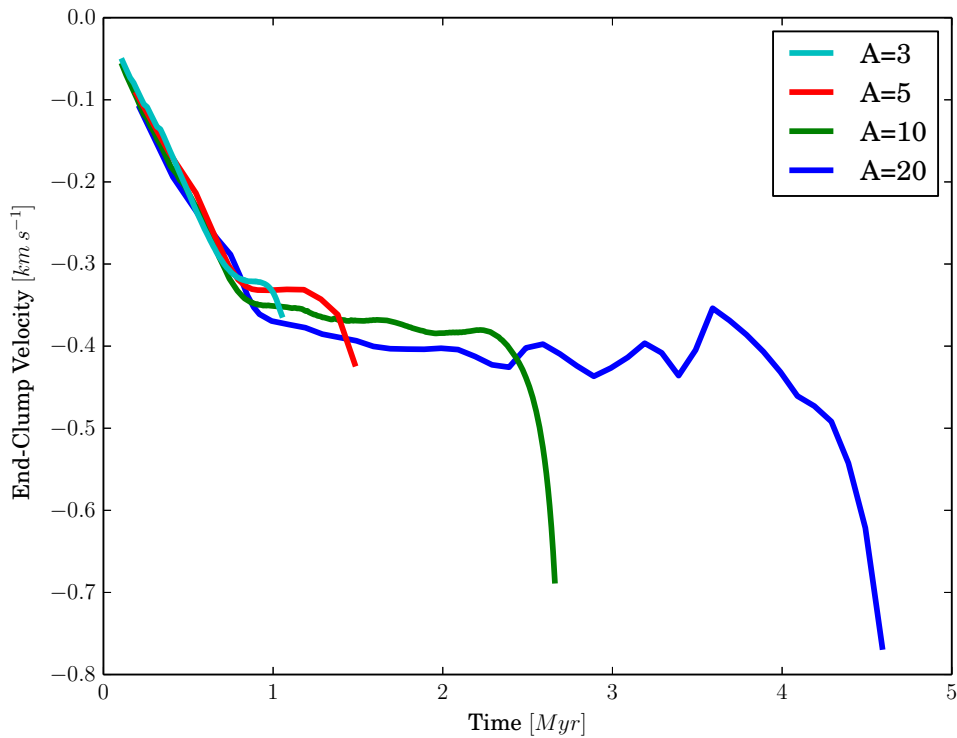


Figure 3.4. The velocity of the $z > 0$ end-clump as a function of time for filaments with initial line-density $\mu_{\odot} = 10 M_{\odot} \text{pc}^{-1}$, radius $R_{\odot} = 0.1 \text{pc}$, and different initial aspect ratios, $A_{\odot} = 3, 5, 10,$ and 20 . In the high aspect ratio simulations the end-clump accelerates inwards for the first $\sim 1 \text{Myr}$, but then approaches a terminal velocity, which is only weakly dependent on A_{\odot} . The sudden increase in the negative velocity at the end of each profile is due to the two end-clumps becoming so close that the motion is dominated by their mutual gravitational attraction; there is essentially no gas left in between them to sweep up.

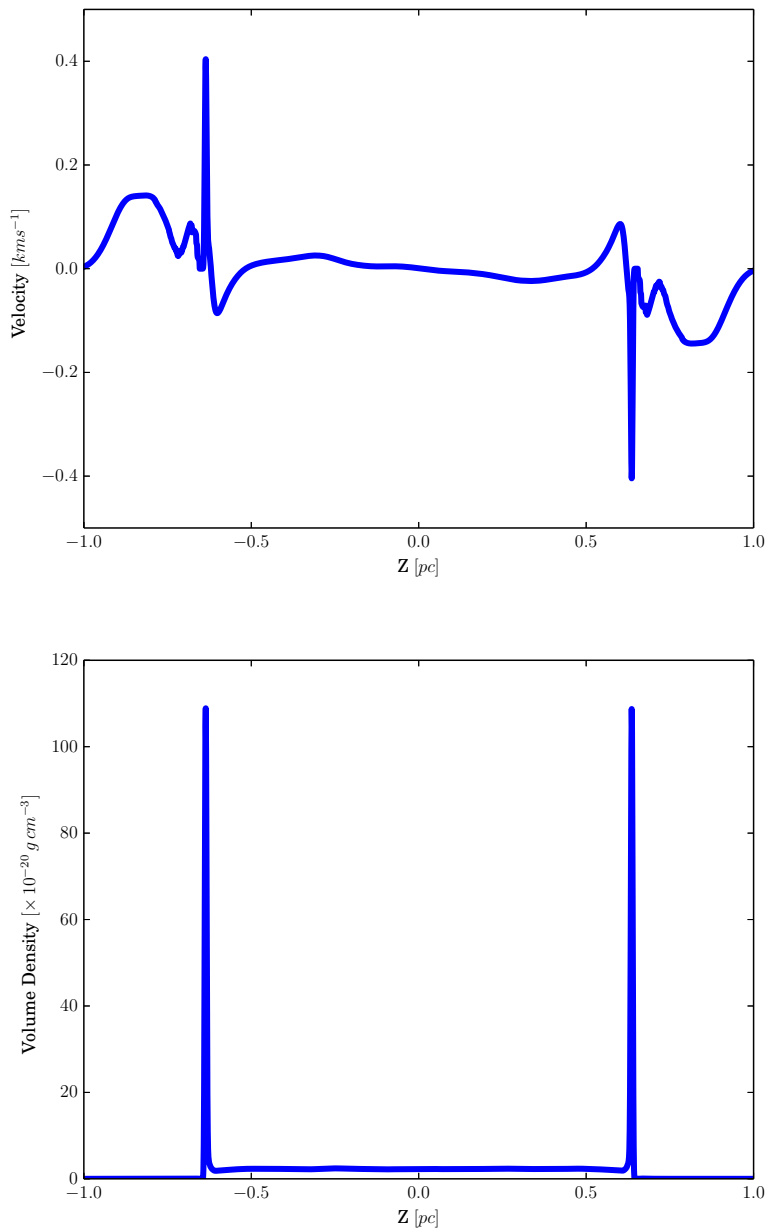


Figure 3.5. (a) The gas velocity along the z -axis at time $t = 1.2 \text{ Myr}$, for the filament with $A_o = 10$, $\mu_o = 10 M_\odot \text{ pc}^{-1}$ and $R_o = 0.1 \text{ pc}$. The gas just interior to the converging end-clumps is moving outwards, thereby increasing the ram-pressure that this gas delivers to the end-clump when it is swept up. (b) The density profile of the same filament at the same point in time. The density peaks (i.e the end-clumps) are at the same position as the velocity peaks. Note the uniformity of the interior density, it has remained roughly constant and uniform since the start of the simulation.

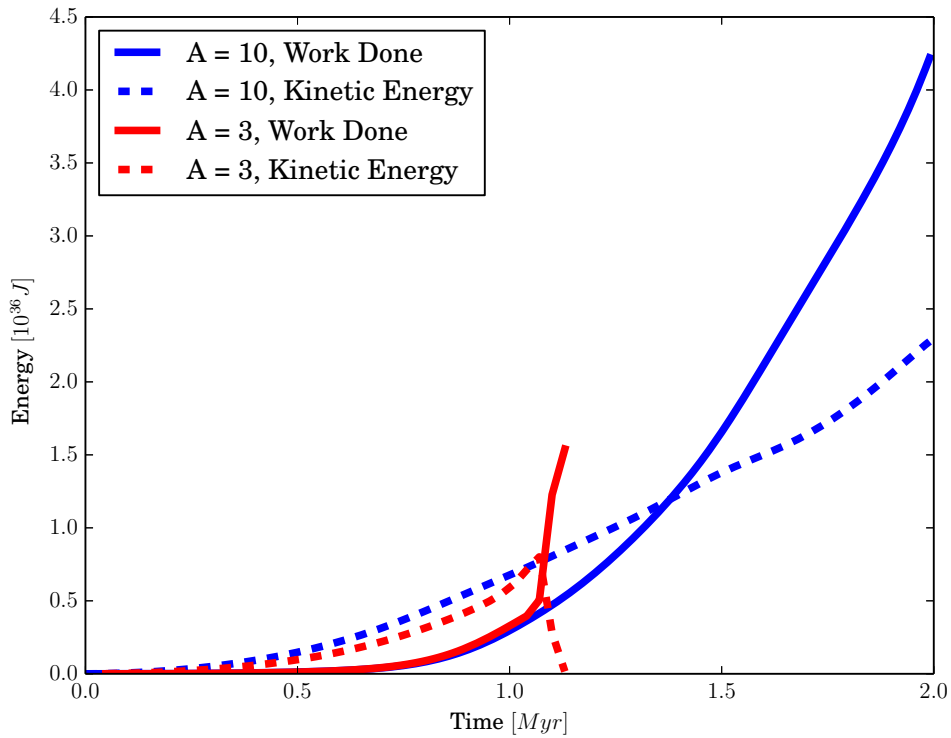


Figure 3.6. The total kinetic energy and the work done on the gas plotted against time for both the high and the low aspect ratio fiducial cases ($\mu_{\odot} = 10 M_{\odot} \text{pc}^{-1}$, $R_{\odot} = 0.1 \text{pc}$ and $A_{\odot} = 10$ or $A_{\odot} = 3$). For the $A_{\odot} = 10$ case, the end-clumps approach their terminal velocity, around 1 Myr; thereafter, the *rate* at which work is done exceeds the *rate* of increase of the kinetic energy. This is not seen in the $A_{\odot} = 3$ case due to the filament collapsing before terminal velocity is reached; the abrupt shift in energies at $\sim 1.1 \text{Myr}$ is due to the end-clumps meeting at $z = 0$.

The first term on the righthand side of Eqn. (3.5) is the gravitational acceleration that the end-clump experiences due to the interior material. $(2\pi G\rho_o R_o)$ is the acceleration derived by Pon et al. (2012) from consideration of a point on the symmetry axis of the filament. α is a correction factor that takes account of the fact that the end-clump extends from the symmetry axis, $r = 0$, to $r = R_o$, where the gravitational acceleration is lower.

The second term on the righthand side of Eqn. (3.5) is the acceleration experienced by the end-clump due to ram pressure; Δv_{REL} is the relative velocity between the end-clump and the material about to be swept up, and $M(t)$ is the mass of the end-clump at time t . If the material interior to the end-clump were stationary, one could write $\Delta v_{\text{REL}} = dz/dt$, where dz/dt is the velocity of the end-clump at time t . However, the interior material is not stationary, as seen in figure 3.5a, and so instead $\Delta v_{\text{REL}} = dz/dt - dz_1/dt$, where dz_1/dt is the velocity of the material just interior to the end-clump at time t . Equation 3.5 is equivalent to the momentum equation used in the Pon et al. (2012) paper. It is their assumption that $\Delta v_{\text{REL}} = dz/dt$ (i.e the interior material is stationary) which distinguishes their analysis from the one presented here.

Fig. 3.7 shows that the velocity of the interior material is relatively low, and it moves inwards and then outwards. If one assumes the effect that this has on the density of the interior material is small, then the mass of the end-clump is $M(t) \simeq \mu_o(Z_o - z(t))$, and the acceleration of the end-clump becomes

$$\frac{d^2 z}{dt^2} \simeq -\alpha(2\pi G\rho_o R_o) + \frac{(dz/dt - dz_1/dt)^2}{(Z_o - z(t))}. \quad (3.6)$$

The assumption that the end clump's mass is approximately the same whether the interior material moves or not is shown to be valid in Fig. 3.8. Here, the mass of the $z > 0$ simulated end clump is compared with the function $M(t) = \mu_o(Z_o - z(t))$ for the high aspect fiducial case. The masses agree with each other within $\sim 10\%$. This is due to the interior density staying roughly constant during the collapse. At such low temperatures the end-clumps are moving supersonically and thus no density waves disturb the material interior to the clumps. Moreover, most of the interior material is unaffected by the gravitational pull of the end clumps and is approximately stationary until an end-clump approaches (Fig. 3.5).

To solve Eqn. (3.6) for $z(t)$ (the location of the end-clump), one must first find dz_1/dt , the speed of the material about to be swept up by the end-clump. The

acceleration at z_1 is

$$\begin{aligned} \frac{d^2 z_1}{dt^2} \simeq & -\alpha(2\pi G\rho_o) \left\{ 2z_1(t) + (R_o^2 + (z(t) - z_1(t))^2)^{1/2} \right. \\ & \left. - (R_o^2 + (z(t) + z_1(t))^2)^{1/2} \right\} \\ & + \beta(2\pi G\rho_o)(Z_o - z(t)) \left\{ \frac{(z(t) + z_1(t))}{(R_o^2 + (z(t) + z_1(t))^2)^{1/2}} \right. \\ & \left. - \frac{(z(t) - z_1(t))}{(R_o^2 + (z(t) - z_1(t))^2)^{1/2}} \right\} \end{aligned} \quad (3.7)$$

The first term on the righthand side of Eqn. (3.7), the one preceded by α , is the contribution to the gravitational acceleration from the material between the end-clumps, i.e. the acceleration at a point $z_1(t)$ in a uniform-density cylinder of radius R_o between $\pm z(t)$, where $z_1(t) < z(t)$ (Burkert & Hartmann, 2004). I have again assumed that the interior material stays at its initial uniform density, and included the factor α to take account of the fact that the material away from the symmetry axis experiences a lower acceleration than the material on the axis.

The second term on the righthand side of Eqn. (3.7; the one preceded by β) is the contribution to the gravitational acceleration from the end-clumps. This term is obtained by treating the end-clumps as discs of uniform surface-density, considering a point on the symmetry axis at $z_1(t)$, and then including a factor β to allow for the fact that material away from the symmetry axis experiences a lower acceleration than the material on the axis.

Eqns. (3.6) and (3.7) are second order non-linear coupled differential equations. I solved them numerically for the high aspect ratio fiducial case ($A_o = 10$, $\mu_o = 10 M_\odot \text{ pc}^{-1}$, $R_o = 0.1 \text{ pc}$), using the first order Euler-Cromer method and $\delta t = 0.003, 0.010$, and 0.020 Myr ; the results obtained with these different δt values are essentially indistinguishable, indicating that the Euler-Cromer method is converged. The interior of the filament is divided into 500 evenly spaced Lagrangian discs and the velocity of each disc calculated at each time-step by integrating Eqn. (3.7). The velocity of the disc just interior to the end-clump is then used to solve Eqn. (3.6). The correction factor α can be evaluated from the simulation data by averaging over the SPH particles in the end-clump, to obtain $\alpha = 0.60$. The correction factor β is obtained by averaging over the SPH particles making up discs of gas interior to the end-clumps, the first term of equation 3.7 is then subtracted. This results in a value of $\beta = 0.40$.

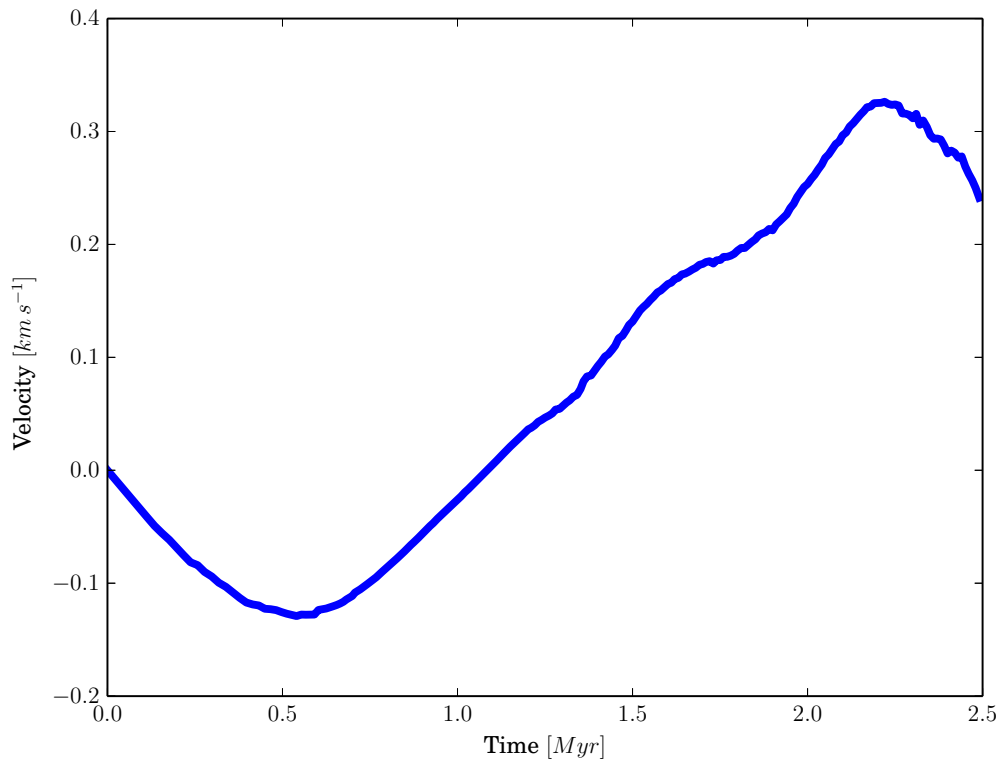


Figure 3.7. The z -velocity of the gas just interior to the $z > 0$ end-clump as a function of time. At early times, this gas flows inward with the end-clump, but at later times, it is attracted gravitationally to the end-clump and moves outwards to meet it. Close to the end of the collapse, the interior material begins to be gravitationally attracted by the $z < 0$ end-clump resulting in the velocity maximum at ~ 2.2 Myr.

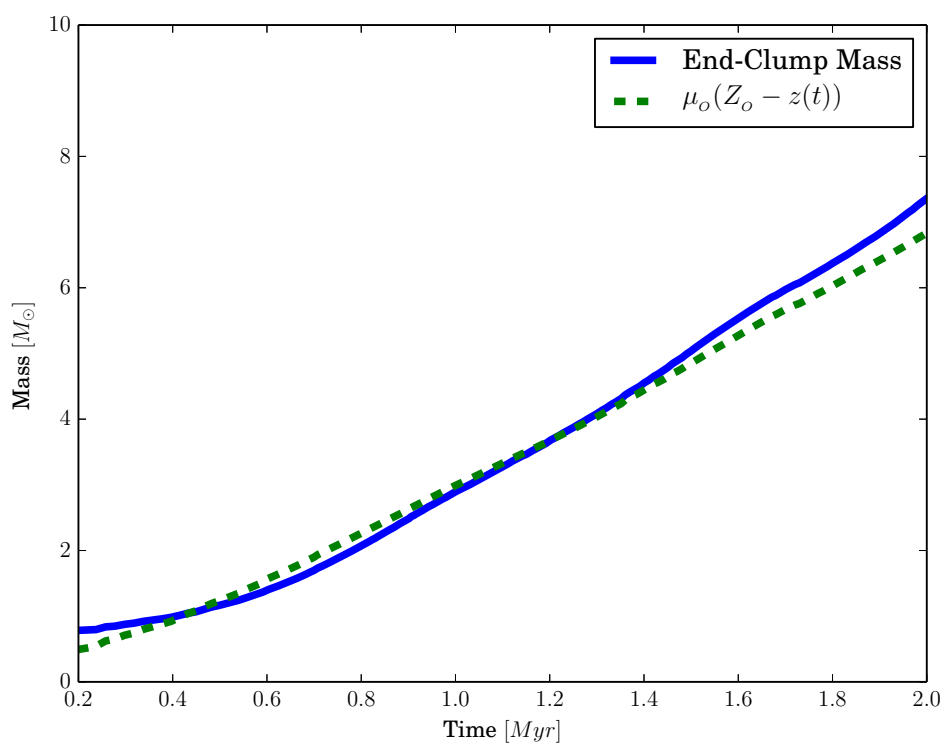


Figure 3.8. The mass of the $z > 0$ simulated end-clump is compared with the end-clump mass expected if the interior material was stationary, $M(t) = \mu_{\circ}(Z_{\circ} - z(t))$. The masses are within $\sim 10\%$ over the course of the simulation.

Fig. 3.9 compares the results of the semi-analytical model with the simulation, for the high aspect ratio fiducial case ($A_o = 10$, $\mu_o = 10 M_\odot \text{pc}^{-1}$, $R_o = 0.1 \text{pc}$) and the low aspect ratio fiducial case ($A_o = 3$, $\mu_o = 10 M_\odot \text{pc}^{-1}$, $R_o = 0.1 \text{pc}$); comparisons have also been made for the cases with $A_o = 10$, $R_o = 0.1 \text{pc}$, and $\mu_o = 35 M_\odot \text{pc}^{-1}$ and $50 M_\odot \text{pc}^{-1}$, and the agreement is equally good. This suggests that the semi-analytical model is capturing the important physical processes, and that the factors $\alpha = 0.60$ and $\beta = 0.40$ are valid correction terms.

If Eqn. (3.6) accurately describes the acceleration of an end-clump, then, once the end-clump approaches its terminal velocity and its acceleration falls towards zero, we must have

$$\frac{(dz/dt - dz_1/dt)^2}{(Z_o - z(t))} \sim \alpha 2\pi G \rho_o R_o. \quad (3.8)$$

Since the righthand side of this equation is constant, a plot of $\log_{10}(dz/dt - dz_1/dt)$ against $\log_{10}(Z_o - z(t))$ should have a slope 0.5. This is shown in figure 3.10 for the high aspect ratio fiducial case ($A_o = 10$, $\mu_o = 10 M_\odot \text{pc}^{-1}$, $R_o = 0.1 \text{pc}$) between 1.2 Myr and 2.2 Myr. It is well fit by a straight line with a gradient of 0.64, close to the expected 0.5. The deviation is due to the fact that the end-clump is not quite moving at a constant velocity; it experiences a small acceleration. There is a small oscillation about the straight line, indicating that, once the terminal velocity is approached, the dynamics is stable: if the end-clump is moving slightly slower than the terminal velocity, the acceleration due to ram pressure is slightly less than the gravitational acceleration, and it speeds up; conversely, if the end-clump is moving slightly faster than the terminal velocity, the acceleration due to ram-pressure is slightly greater than the gravitational acceleration, and it slows down.

Eqn. (3.4) agrees with the generic theorem that the free-fall collapse time for a uniform-density filament is longer than for a sphere of the same uniform density. However, it disagrees with the predictions of Pon et al. (2012) (Figure 3.2a). Overall, Pon et al. (2012) predicts somewhat longer collapse times for short filaments, $A_o < 9$, and shorter collapse times for longer filaments, $A_o > 9$. The Pon et al. (2012) collapse times for short filaments are too long, because their analysis assumes such filaments collapse homologously. They also assume that the interior material is stationary but as seen in figure 3.7 at early times the material is moving inwards with the end-clumps, reducing the retarding ram-pressure. The Pon et al. (2012) collapse times for long filaments are too short, because their analysis does not take account of the interaction between an end-clump and the material it is about to sweep up, as analysed in §3.4. I do not consider the discrepancies between the results presented here and those found in Pon et al. (2012) for the range $A_o < 3$ as such a cloud is outside our definition of

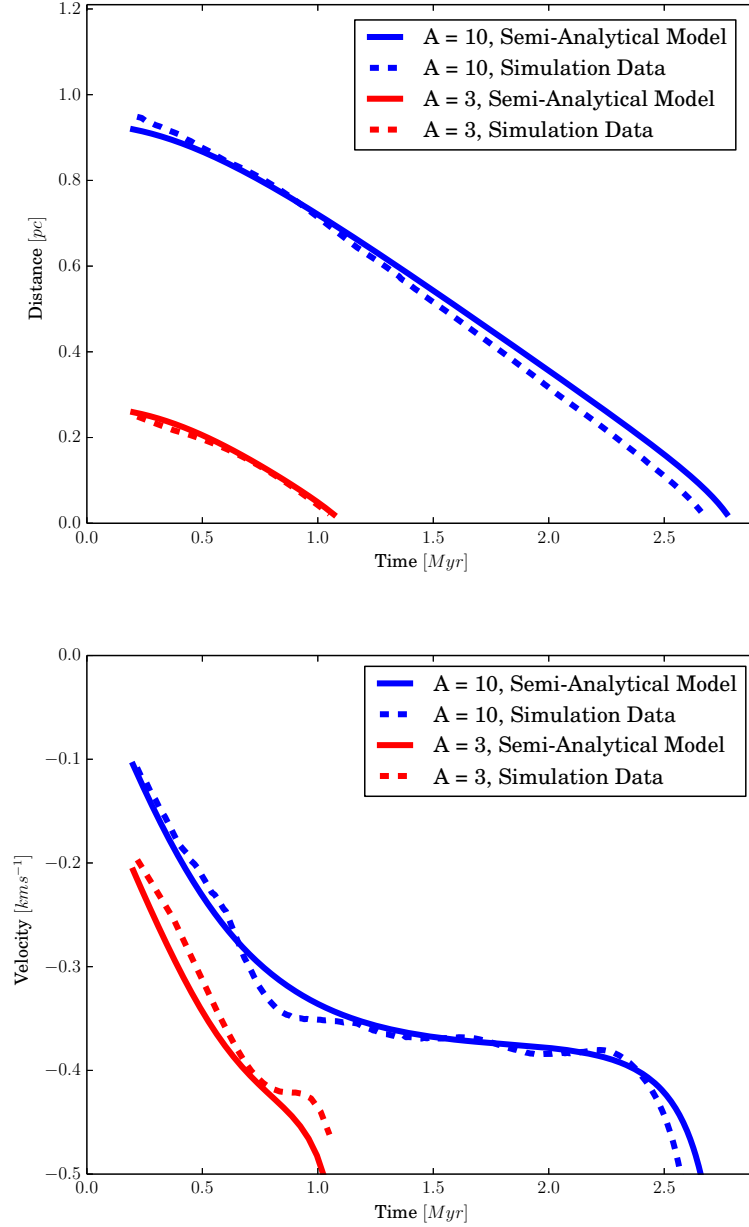


Figure 3.9. A comparison between simulation data and the semi-analytic model for a filament characterised by $\mu_{\text{O}} = 10 M_{\odot} \text{pc}^{-1}$, $R_{\text{O}} = 0.1 \text{pc}$ and either $A_{\text{O}} = 10$ or $A_{\text{O}} = 3$. (a) The position of the end-clump as a function of time. It starts at $t = 0.2 \text{Myr}$ when the end-clumps are clearly established. (b) The velocity of the end-clump as a function of time. The velocity of the $A_{\text{O}} = 3$ end clump has been shifted downwards by 0.1km s^{-1} for clarity. Simulation and model profiles fit reasonably well for both initial aspect ratios.

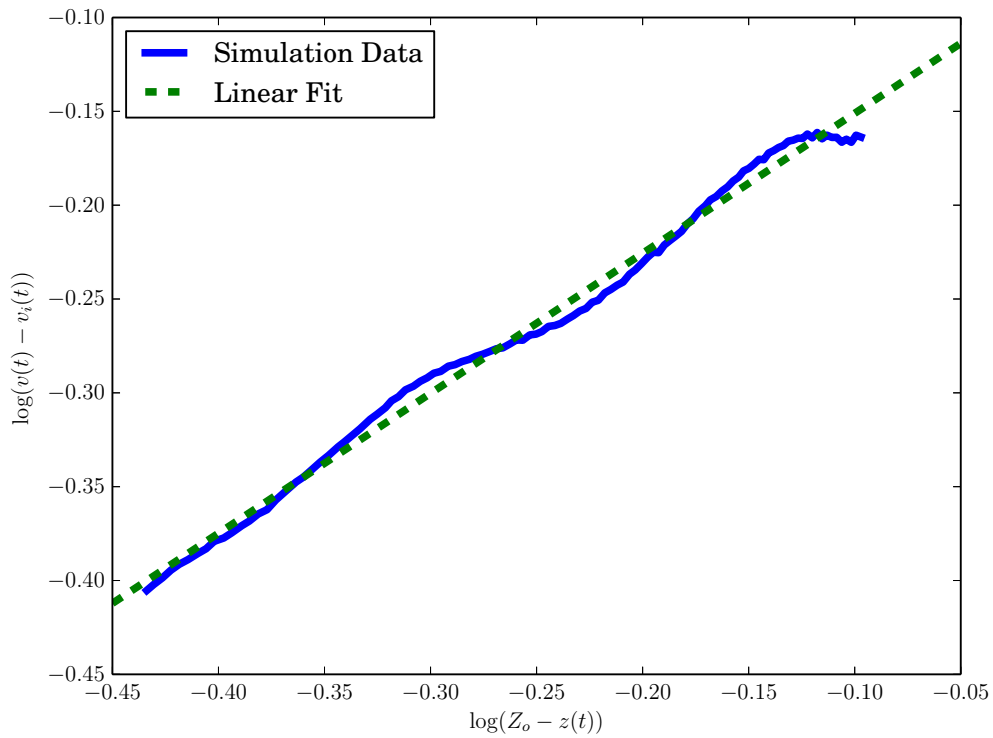


Figure 3.10. A test of the validity of equation 3.8; $\log_{10}(dz/dt - dz_1/dt)$ is plotted against $\log_{10}(Z_o - z(t))$ for the high aspect ratio fiducial case. The simulation data are well fit by a straight line with a gradient of 0.64, close to the expected 0.5. The oscillations around the linear fit show that once the terminal velocity is approached, the dynamics is stable.

a filament.

3.4.2 OBSERVATIONAL EVIDENCE OF END-DOMINATED COLLAPSE

Recent observations of isolated filamentary infra-red dark clouds (IRDCs) show signs of end-dominated longitudinal collapse (Zernickel, Schilke & Smith, 2013; Beuther et al., 2015; Kainulainen et al., 2016a). In the case of IRDC 18223 (Beuther et al., 2015) two massive cores are seen at either end of the filament (figure 3.11). Core 2 is found to have a mass of $377 M_{\odot}$ and core 11 is found to have a mass of $385 M_{\odot}$, the average core mass in the filament is $76 M_{\odot}$. The formation of such large cores could be explained by end-dominated global collapse. The high gravitational acceleration at the filament's ends causes interior material to be swept up and produces a massive dense region.

Due to its relatively pristine condition, the massive cores in IRDC 18223 may be used to give a minimum age of the system. The ratio between the end-clump gas density and interior gas density changes with time, figure 3.12 shows the evolution of this 'contrast' ratio over time for both the high and low aspect ratio fiducial cases and for the case: $A_0 = 10$, $\mu_0 = 35 M_{\odot} \text{ pc}^{-1}$, $R_0 = 0.1 \text{ pc}$. The contrast ratio is independent of initial aspect ratio but is stretched by a factor of $\rho_0^{-1/2}$ in the x-direction. Thus, if one knows the current contrast ratio and the average density of the interior gas (assuming the current average density is the same as the initial density) one can use this curve to estimate the time it took for the end-clumps to reach such a density. This time estimate should be considered a minimum age as the simulations presented in this chapter do not contain any gas outside the filament; as seen in Pon, Johnstone & Heitsch (2011) the presence of a smooth tapering of density at the filament's ends reduces the gravitational acceleration and increases the collapse time. Beuther et al. (2015) estimate that IRDC 18223 has a number density in the range $10^4 - 10^5 \text{ cm}^{-3}$, this is between 1.6 and 16 times as dense as the fiducial cases. Figure 3.13 shows the contrast ratio evolution for the upper and lower density limits. The contrast ratio between the observed column density in core 2 and 11, and the column density observed in the interior gas is $\sim 5 - 6$, which corresponds to a minimum age for IRDC 18223 of $0.4 \pm 0.25 \text{ Myr}$.

In contrast to IRDC 18223, the filamentary Musca molecular cloud (Kainulainen et al., 2016a) has been observed to have highly fragmented regions at either end of the filament, while the centre is relatively uniform and sterile. This can also be explained by end-dominated collapse. The collection of high density gas in the end-clumps leads to an area of preferential star formation and fragmentation. In this

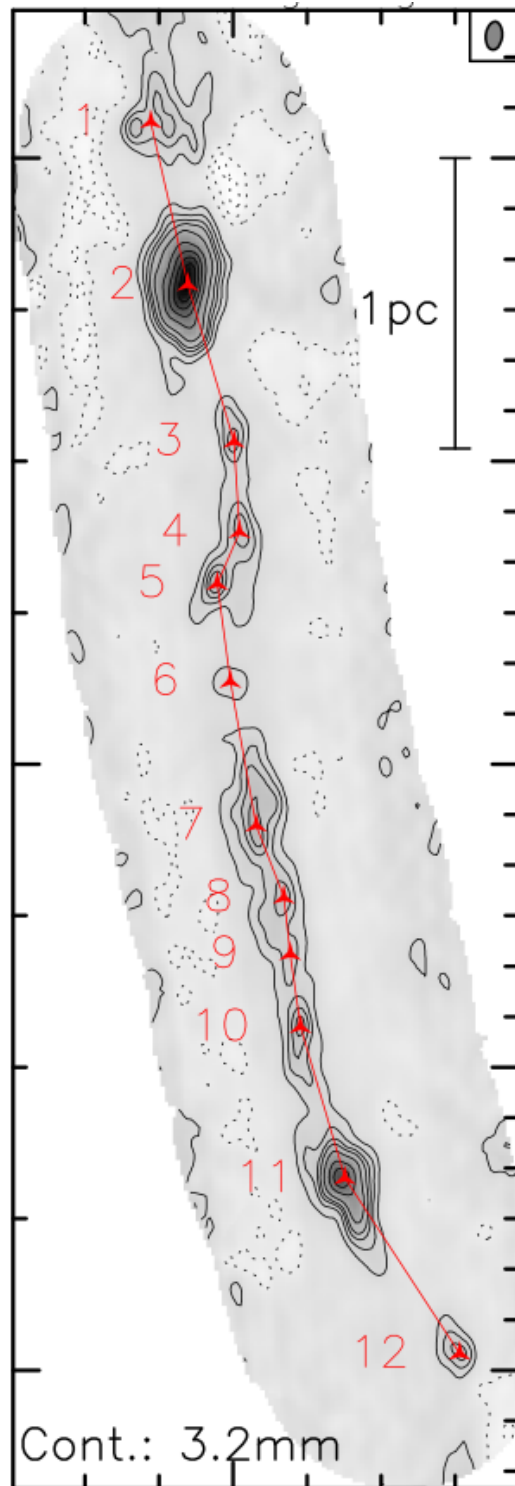


Figure 3.11. A 3.2mm continuum image of the IRDC 18223 filament, figure 2 in Beuther et al. (2015). The most notable feature of this cloud are the two massive cores at either end of the filament, cores 2 and 11. These two cores could be the end-clumps formed due to global collapse.

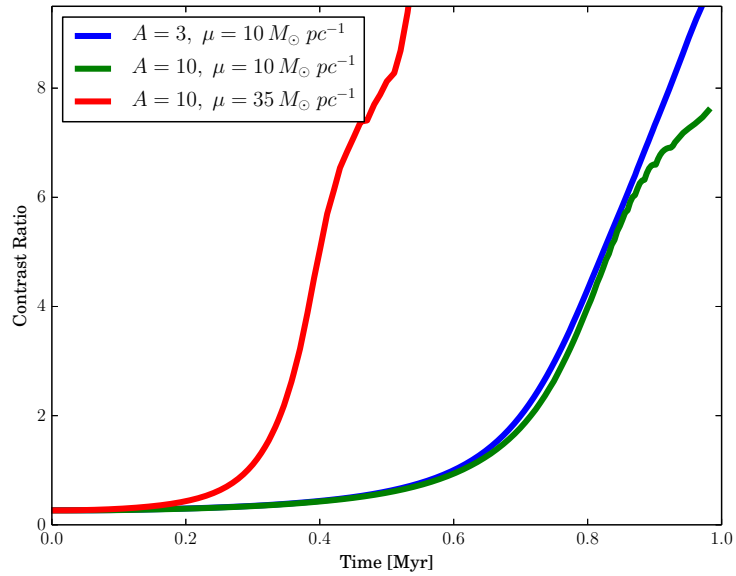


Figure 3.12. The time evolution of the ratio between the density of gas in the end-clumps and gas in the interior material. The evolution of this ‘contrast’ ratio is independent of the initial aspect ratio of the filament (the blue and green lines.) It is solely dependent on the initial density of the filament, as seen when comparing the red and the green lines. This dependence is characterised by a stretching in the x -axis by a factor of $\rho_0^{-1/2}$.

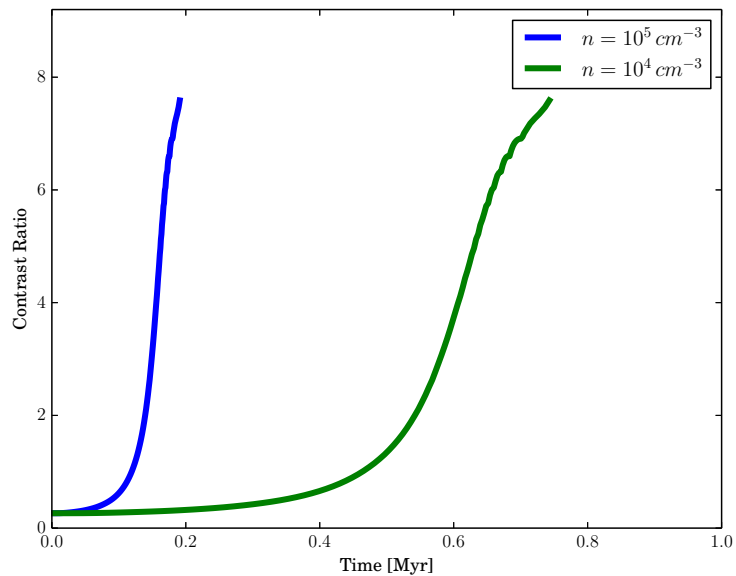


Figure 3.13. The time evolution of the contrast ratio for IRDC 18223 assuming number densities of $n = 10^5 \text{ cm}^{-3}$ and $n = 10^4 \text{ cm}^{-3}$. Using the observed column densities in Beuther et al. (2015), the contrast ratio is found to be $\sim 5 - 6$. This leads to a timescale in the range $0.4 \pm 0.25 \text{ Myr}$.

scenario, the global collapse of the filament gathers large amounts of gas quickly which proceeds to form stars before the interior gas. As the end-clumps are denser than the rest of the filament, the fragmentation timescale will be shorter; thus the end-clumps are more prone to fragmentation than the interior gas. It is unclear why some end-clumps fragment and others remain as monolithic structures. High resolution observations may find that the end-clumps in IRDC 18223 have fragmented.

3.5 SUMMARY

Pon et al. (2012) have suggested that there are two modes for the freefall collapse of a uniform-density filament: short filaments, $A_o < 5$, collapse homologously, on a timescale that varies as A_o (see Eqn. 3.1); longer filaments undergo end-dominated collapse, on a timescale that varies as $A_o^{1/2}$ (see Eqn. 3.3). I find no such dichotomy. Rather, end effects are evident for all aspect ratios, and just one equation,

$$t_{\text{COL}} = (0.49 + 0.26A_o) (G\rho_o)^{-1/2} \quad (3.4)$$

predicts the free-fall collapse times obtained in the simulations to within $\pm 3\%$ for $2 < A_o < 20$, $2 M_\odot \text{ pc}^{-1} < \mu_o < 50 M_\odot \text{ pc}^{-1}$, and $0.05 \text{ pc} < R_o < 0.15 \text{ pc}$.

The linear relationship between t_{COL} and A_o , for large aspect ratios, is due to the fact that the end-clumps quickly approach a terminal velocity before collapse finishes. The same linear relationship still holds for small aspect ratio filaments despite the lack of a terminal velocity. Hence, the linear relationship is ultimately a result of the dynamics of the system which are independent of initial aspect ratio. Before being swept up, the gas immediately ahead of an end-clump is accelerated outwards by the gravitational attraction of the approaching end-clump. This outward velocity increases the amount of ram pressure exerted on the end-clump, and the amount of work needed to accelerate and compress the swept up gas. Pon et al. (2012) neglected this outward moving gas and its consequences (Pon, private comm.).

I have constructed a semi-analytical model which describes the acceleration of the gas in a collapsing filament, using only gravity and ram-pressure. This model is able to reproduce the end-clump position and velocity seen in the simulations and accurately describes the evolution of the end-clumps over a range of initial conditions.

I apply this model to recent observations of isolated filamentary clouds that have dense or highly fragmented massive clumps at their ends. The presence of large cores or increased fragmentation at the ends of these clouds can be explained by positing that they are undergoing end-dominated collapse. Moreover, in those cases

which show no fragmentation in the end-clumps, one can determine a minimum age of the filament by measuring the ratio of column density in the end clump and column density in the centre.

CHAPTER 4

PERTURBATION GROWTH IN ACCRET- ING FILAMENTS *

In this chapter I present a series of Smoothed Particle Hydrodynamic simulations used to investigate the growth of perturbations in infinitely long filaments as they form and grow by accretion. The growth of these perturbations leads to filament fragmentation and the formation of cores. Most previous work on this subject has been confined to the growth and fragmentation of equilibrium filaments and has found that there exists a preferential fragmentation length scale which is roughly 4 times the filament's diameter. My results show a more complicated dispersion relation with a series of peaks linking perturbation wavelength and growth rate. These peaks are due to gravo-acoustic oscillations along the longitudinal axis during the sub-critical phase of growth. The positions of the peaks in growth rate have a strong dependence on both the mass accretion rate onto the filament and the temperature of the gas. When seeded with a multi-wavelength density power spectrum there exists a clear preferred core separation equal to the largest peak in the dispersion relation. My results allow one to estimate a minimum age for a filament which is breaking up into regularly spaced fragments, as well as an average accretion rate. The model is applied to observations of filaments in Taurus by Tafalla & Hacar (2015) and I find an accretion rate in agreement with that estimated by Palmeirim et al. (2013). This model is also applied to the infra-red dark cloud IRDC 18223.

*The work presented here is published in Clarke, Whitworth & Hubber, 2016, MNRAS, 458, 319

4.1 INTRODUCTION

The prevalence of filamentary structures across a wide range of scales (Schneider & Elmegreen, 1979; Lada, Alves & Lada, 1999; Hartmann, 2002; Myers, 2009; André et al., 2010; Palmeirim et al., 2013; Beuther et al., 2015) has led to several papers studying their structure, stability, fragmentation and collapse (Ostriker, 1964; Larson, 1985; Inutsuka & Miyama, 1992; Burkert & Hartmann, 2004; Pon, Johnstone & Heitsch, 2011; Fischera & Martin, 2012; Heitsch, 2013; Clarke & Whitworth, 2015).

It has been shown that a filament's line density (defined as the mass per unit length) determines the filament's radial stability: filaments below a critical line density will not and cannot be made to collapse radially, those with line density above the critical value will. For an isothermal filament the critical line density is

$$\mu_{\text{CRIT}} = \frac{2a_0^2}{G} \sim 16.7 M_\odot \text{ pc}^{-1} \left(\frac{T}{10 \text{ K}} \right), \quad (4.1)$$

where a_0 is the isothermal sound speed, G is the gravitational constant and T is the gas temperature (Ostriker, 1964).

The Herschel Gould Belt Survey has shown that the majority of star-forming cores are found within filaments which have super-critical line densities, while sub-critical filaments are sterile (André et al., 2010). It has also been shown theoretically that, due to their geometry, filaments are apt to fragment; small-scale perturbations can readily collapse locally before global longitudinal collapse overwhelms them (Pon, Johnstone & Heitsch, 2011). This suggests a paradigm in which filaments are formed inside molecular clouds, and the densest of these filaments then become super-critical and go on to fragment into cores.

Inutsuka & Miyama (1992) have analysed how small-scale perturbations grow and collapse in an *equilibrium* filament; they derive a dispersion relation linking perturbation wavelength with perturbation growth rate. They find that perturbations are unstable when their wavelength is larger than twice the filament's diameter, and there exists a fastest growing mode at approximately 4 times the filament's diameter. When the line density of an isothermal filament exceeds the critical value by a small amount, the perturbations do not have time to grow before global radial collapse takes place; in this case, it is thought that fragmentation occurs at the point when the gas becomes optically thick and starts to heat up so that radial collapse is halted.

Though perturbations in equilibrium and super-critical filaments have been studied before (e.g. Larson, 1985; Inutsuka & Miyama, 1992, 1997; Freundlich, Jog & Combes, 2014), non-equilibrium filaments have been neglected. However, it is unlikely

that when a filament first forms it is in equilibrium or has a super-critical line density; it is far more likely that a filament will be sub-critical when it first forms and mass then accretes on to it until it becomes unstable and fragments. As filaments and perturbations form together and co-evolve, it is important to understand how density perturbations behave during the sub-critical phase, especially so if one attempts to link the density perturbation power spectrum to the core mass function (Inutsuka, 2001; Roy et al., 2015).

In this chapter, I present numerical simulations of initially sub-critical perturbed accreting filaments, in order to investigate the dispersion relation between perturbation wavelength and perturbation growth rate, and to compare to the relation found by Inutsuka & Miyama (1992) for equilibrium filaments. In section 4.2, I detail the simulation setup and the initial conditions used; in section 4.3, I present the results of these simulations; in section 4.4, I discuss their significance and compare to previous work; and in section 4.5, I summarize my conclusions.

4.2 NUMERICAL SETUP

The simulations presented in this chapter are performed using the Smoothed Particle Hydrodynamics (SPH) code GANDALF (Hubber et al. in prep). The simulations invoke both self-gravity and hydrodynamics, with the barotropic equation of state

$$T(\rho) = T_{\text{O}} \left(1 + \left(\frac{\rho}{\rho_{\text{BARO}}} \right)^{2/3} \right). \quad (4.2)$$

Here T_{O} is the initial temperature and $\rho_{\text{BARO}} = 10^{-14} \text{ g cm}^{-3}$ is the critical density at which the gas changes from being approximately isothermal to approximately adiabatic. I present two sets of simulations, one with $T_{\text{O}} = 10 \text{ K}$ and the other with $T_{\text{O}} = 40 \text{ K}$; this results in isothermal sound speeds of $\sim 0.19 \text{ km/s}$ and $\sim 0.37 \text{ km/s}$ respectively, assuming solar metallicity. Grad-h SPH (Price & Monaghan, 2004) is implemented, with $\eta = 1.2$, so that a typical particle has ~ 58 neighbours. Sink particles are implemented as described in Hubber, Walch & Whitworth (2013) using the sink creation density, $\rho_{\text{SINK}} = 10^{-12} \text{ g cm}^{-3}$.

The computational domain is open in the x and y directions, but is periodic in z , the long axis of the filament (see Wünsch et al. in prep, for the implementation of the modified Ewald field). This in effect allows us to study the perturbation growth in an infinitely long filament, and hence to ignore the complicating effects of global longitudinal collapse (Clarke & Whitworth, 2015).

One can generate an arbitrary density field in SPH by stretching a distribution

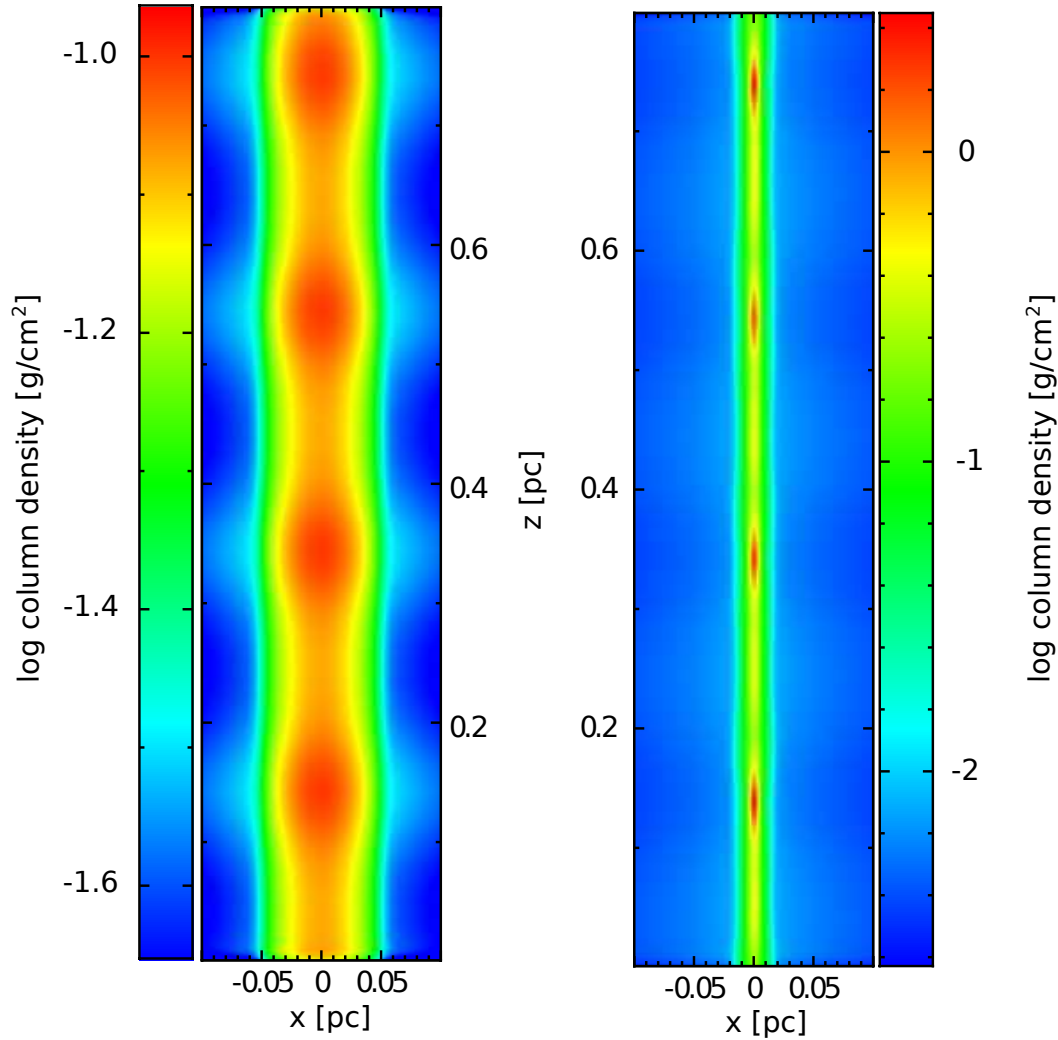


Figure 4.1. The column density projected onto the x - z plane for the fiducial case (i.e. $A = 0.2$, $\lambda = 0.2$ pc, $T_{\text{O}} = 40$ K and $\dot{\mu} = 70 M_{\odot} \text{pc}^{-1} \text{Myr}^{-1}$) at two different times. On the left, at $t = 0.15$ Myr, the filament has formed on the z axis, it is sub-critical and confined by the ram pressure of the accreting gas. On the right, at $t = 0.55$ Myr, the filament has become supercritical and is contracting radially; at the same time the seeded perturbations have become sites of local collapse. Created using the visualisation tool SPLASH (Price, 2007).

of particles with uniform density. This is done by constructing the cumulative mass profile along each axis at every position for both the arbitrary density field and the uniform density field. One axis at a time, the cumulative mass at a particle's position is noted for the uniform density case, the particle is then moved to the position which corresponds to the same cumulative mass for the arbitrary density field. This results in an arbitrary density field with very little noise. (Lomax priv. comm.)

To generate the initial conditions, a cylindrical settled glass of particles with a uniform density is stretched so that it reproduces the density profile,

$$\rho(r, z) = \frac{\rho_o r_o}{r} \left(1 + A \sin \left(\frac{2\pi z}{\lambda} \right) \right). \quad (4.3)$$

Here ρ_o is the density at $r_o = 0.1$ pc, A is the amplitude of the perturbation and λ is the perturbation's wavelength. The initial velocity field is,

$$\underline{v} = -v_o \hat{r}. \quad (4.4)$$

Combined, these density and velocity profiles result in a setup which can be characterised by A , λ and the influx of mass per unit length, $\dot{\mu} = 2\pi\rho_o r_o v_o$.

The resulting perturbed cylinder of particles has a radius of $r_{max} = 1$ pc, and a length, $L = m\lambda$, where m is the largest integer that satisfies $L \leq 1$ pc. This provides a sufficiently large computational domain to allow us to study a wide range of plausible perturbation wavelengths, while maintaining good resolution. I am confident that the effects of a periodic boundary condition in the z -direction is minimal. Taking a length of 1 pc for the computational domain and a temperature of 40 K, leading to an isothermal sound speed of 0.37 km/s, the sound crossing time for the computational domain is ~ 2.5 Myr. The simulations are typically ended after ~ 0.7 Myr.

I stress that there is no filament present at the outset. At $t = 0$ all the material is flowing radially inwards, towards the z -axis. As soon as the simulation starts, an accretion shock forms on the z -axis and then propagates outwards; the filament is the dense material inside this shock. The initial setup should be seen as a simple approximation to the formation of a filament, a locally convergent flow in a globally turbulent field.

I consider perturbations which are initially small, taking $A = 0.1$ or 0.2 . The perturbation wavelength λ is varied between 0.05 pc and 0.5 pc. The lower limit is due to resolution concerns, and the upper limit to ensure that at least 2 wavelengths fit within the computational domain. The mass flux per unit length is varied between

$\sim 10 M_{\odot} \text{ pc}^{-1} \text{ Myr}^{-1}$ and $\sim 100 M_{\odot} \text{ pc}^{-1} \text{ Myr}^{-1}$, in line with the accretion rates estimated observationally by Palmeirim et al. (2013) and Kirk et al. (2013). I define the critical time as the time at which the filament reaches the critical line density and becomes radially unstable, $\tau_{\text{CRIT}} \sim \mu_{\text{CRIT}}/\dot{\mu}$.

After the first sink forms, I only follow the simulation for a further 0.01 Myr, since I am principally interested in the dynamics that lead to instability, rather than the subsequent collapse.

The simulations are run with 3 million particles per parsec, giving a particle mass of $1.5 \times 10^{-5} M_{\odot}$ and $4 \times 10^{-5} M_{\odot}$ and a mass resolution of between $1.5 \times 10^{-3} M_{\odot}$ and $4 \times 10^{-3} M_{\odot}$. Such high resolution is necessary to ensure the small wavelength perturbations are well resolved even at low densities. The artificial viscosity needed to capture shocks is known to overly dampen short wavelength oscillations on the order of the smoothing length. Therefore, I have invoked time dependent artificial viscosity as described in Morris & Monaghan (1997) to further lessen the effect of artificial viscosity on short wavelength oscillations. Tests with different numbers of particles show that the simulations are converged at 3 million particles per parsec.

4.3 RESULTS

The perturbations seeded in the initial density profile survive the approximately cylindrical accretion shock bounding the filament, and form a radially sub-critical perturbed filament of typical width $\sim 0.1 \text{ pc}$ (figure 4.1a). The rest of the gas continues to accrete onto the filament until it reaches the critical line density and the perturbed sections collapse (figure 4.1b). This can be seen clearly in figure 4.2 which shows the time evolution of the full width half maximum of a filament's longitudinally and azimuthally averaged radial density profile. As material flows onto the filament it grows wider but at $\sim 0.3 \text{ Myr}$ it reaches its maximum diameter and begins to contract. As the filament's diameter is constantly changing throughout the simulation, it is unclear one would attempt to apply the Inutsuka & Miyama (1992) equilibrium fragmentation model.

I take the time at which the first sink particle forms, τ_{SINK} , as a proxy for the perturbation growth time. The earlier a sink particle forms the faster the perturbation became unstable. Specifically I define the perturbation growth rate as $g_{\lambda} = 1/\tau_{\text{SINK}}$. Figure 4.3 shows the dispersion relation linking perturbation wavelength with perturbation growth rate for $T_{\text{O}} = 40 \text{ K}$, $\dot{\mu} = 70 M_{\odot} \text{ pc}^{-1} \text{ Myr}^{-1}$ and $A = 0.2$ (the fiducial case) and also with $A = 0.1$. It is evident that the inclusion of the non-equilibrium

sub-critical phase has dramatically changed the relationship from the one derived by Inutsuka & Miyama (1992). There no longer exists a single local maximum at 4 times the filament's diameter. Instead the dispersion relation appears to have two features: longer wavelength perturbations tend to grow faster, and superimposed on this there is a series of peaks and troughs.

Varying the mass accretion rate one sees that the shape of the dispersion relation is unchanged, but it is rescaled in the x-direction (figure 4.4). As the mass accretion rate is increased, and the time taken for the filament to become supercritical is decreased, the dispersion relation is squeezed and the peaks in the growth rate move to shorter wavelengths. Let us suppose that there exists a function, $f(x)$, which transforms the parameters, λ , a_o and $\dot{\mu}$, into the observed dispersion relation g_λ . Figure 4.4 shows that the dispersion relation takes the form $g_\lambda = f(\lambda\dot{\mu}) = f(\lambda/\tau_{\text{CRIT}})$, where τ_{CRIT} is the time at which the filament becomes supercritical.

When the initial temperature of the gas, and by extension the isothermal sound speed, is varied one sees the same type of behaviour as when the mass accretion rate is varied (figure 4.5). As the temperature of the gas is decreased the dispersion relation is squeezed and the peaks in the growth rate move to shorter wavelengths. We find that the stretching goes as $T_o^{-1/2}$, or as a_o^{-1} , so one can write the dispersion relation as $g_\lambda = F(\lambda/a_o\tau_{\text{CRIT}})$.

4.4 DISCUSSION

The primary characteristic of the sub-critical phase is that thermal pressure forces are greater than gravitational forces. Thus, during this phase the evolution of the perturbations within the filament is dominated by acoustic oscillations, and standing waves are set up along its length. Figure 4.6 shows the volume-density profile along the z -axis at two different times. The density peaks oscillate with a period $\lambda/a_o \sim 0.50\text{Myr}$. Thus, between 0.05 Myr and 0.30 Myr, a half period has elapsed, and the density peaks and troughs have switched.

It is the presence of these acoustic density oscillations that gives rise to the oscillations seen in the dispersion relation (figure 4.3). The depressed growth rate at certain wavelengths is due to the fact that in these cases the time at which radial collapse begins, τ_{CRIT} , coincides with the point in the oscillation at which the peak of the density perturbation is being dispersed and reformed at a trough (figure 4.7). Thus when the gas making up the density peak becomes self-gravitating it is moving outwards. This has two consequences: the gas must first be decelerated and turned around before the perturbation collapses longitudinally as well as radially, and the

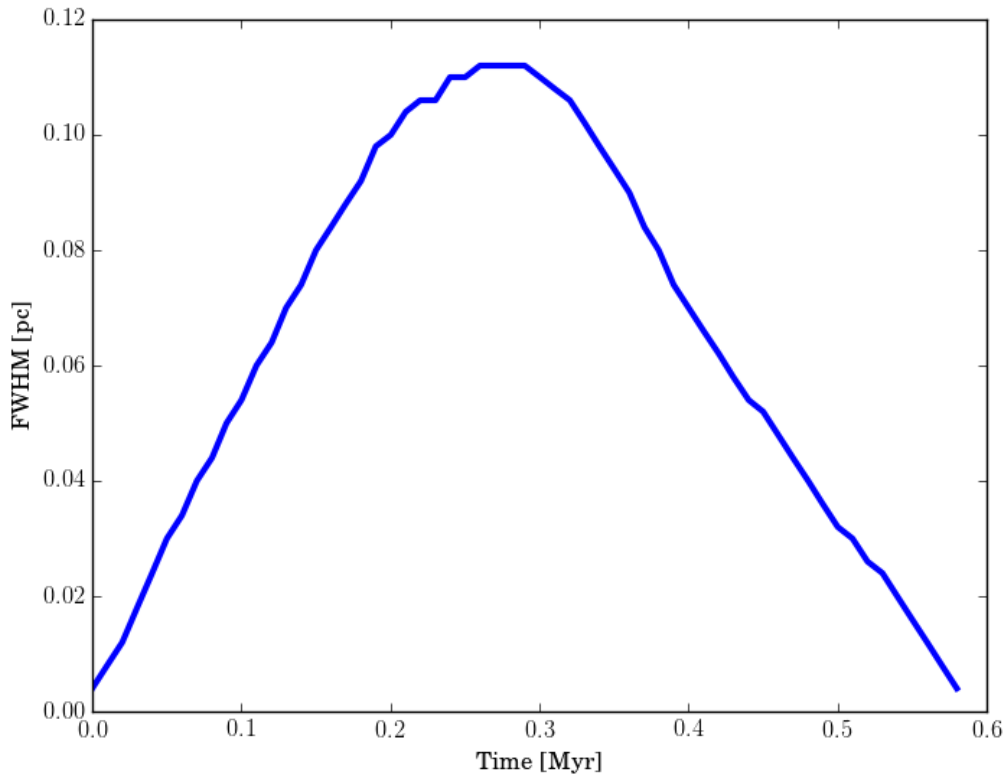


Figure 4.2. The time evolution of the full width half maximum (FWHM) of the filament's longitudinal and azimuthally averaged radial density profile for the simulations with $T_{\text{O}} = 40 \text{ K}$, $\dot{\mu} = 70 \text{ M}_{\odot} \text{ pc}^{-1} \text{ Myr}^{-1}$, $A = 0.2$ and $\lambda = 0.1 \text{ pc}$. One can see that the diameter is in range $0.05 - 0.12 \text{ pc}$ for much of the filament's evolution.

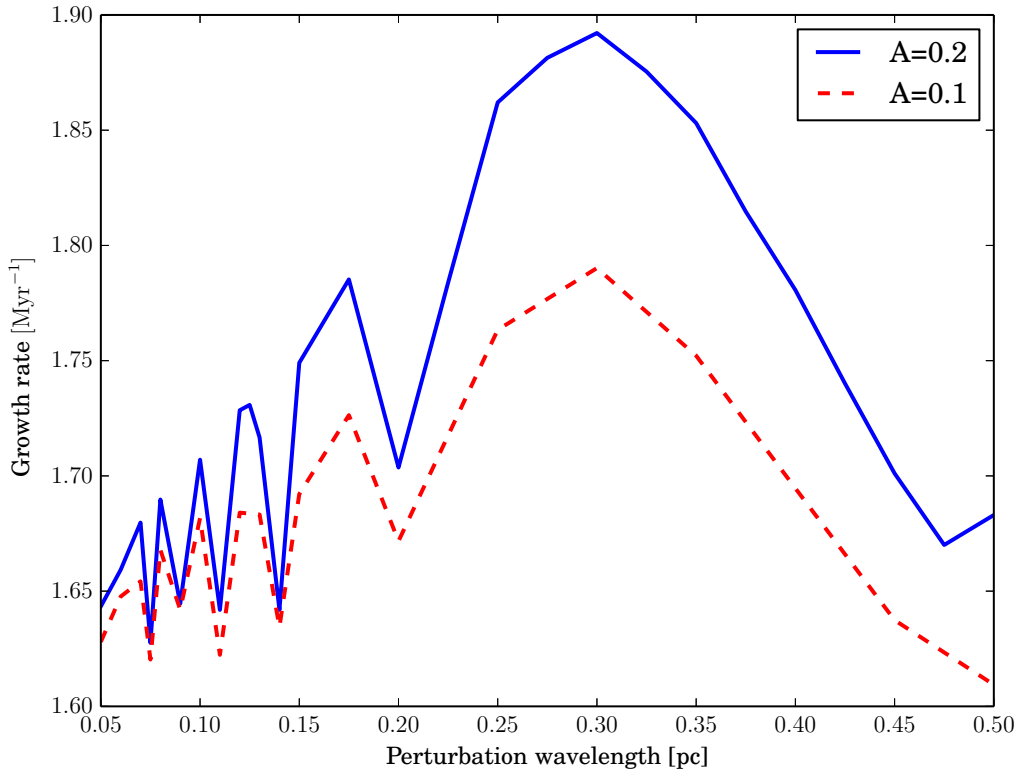


Figure 4.3. The dispersion relation between perturbation wavelength and perturbation growth rate for $T_{\odot} = 40 \text{ K}$, $\dot{\mu} = 70 \text{ M}_{\odot} \text{ pc}^{-1} \text{ Myr}^{-1}$ and $A = 0.2$ (the fiducial case) and also with $A = 0.1$. There no longer exists a single local maximum at 4 times the filament’s diameter, instead there exists a series of peaks and troughs. The initial amplitude of the perturbations does not affect the shape of the dispersion relation, rather it only affects the magnitude of the growth rate.

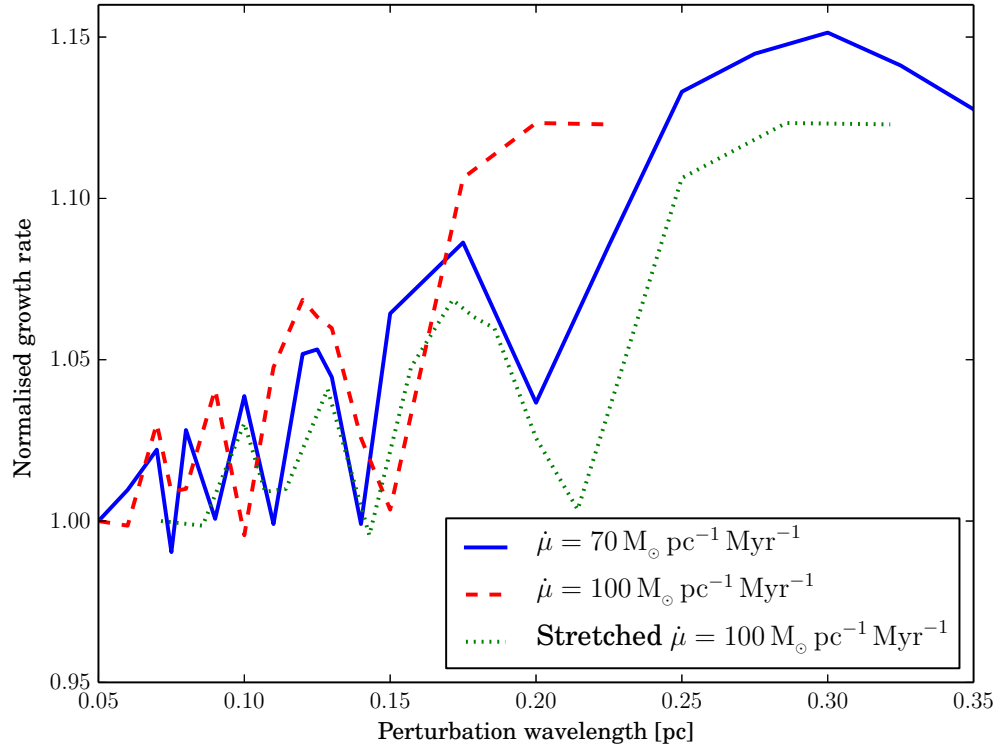


Figure 4.4. The dispersion relation between perturbation wavelength and normalised growth rate for the fiducial case ($\dot{\mu} = 70 M_{\odot} \text{ pc}^{-1} \text{ Myr}^{-1}$), and for the case with $\dot{\mu} = 100 M_{\odot} \text{ pc}^{-1} \text{ Myr}^{-1}$. The normalised growth rate is defined as $\hat{g}_{\lambda} = g_{\lambda}/g_{0.05\text{pc}}$. The fiducial case (solid blue line) and the case with a higher accretion rate (dashed red line) are out of phase, the peaks in the dispersion relation do not line up. The higher accretion rate has caused the relation to be squeezed in the x-direction. The green dotted line is the result of stretching the high accretion line assuming the dispersion relation takes the form $g_{\lambda} = f(\lambda/\tau_{\text{CRIT}})$, where τ_{CRIT} is the time at which the filament becomes supercritical. The peaks in the stretched dispersion relation now line up with those from the fiducial case.

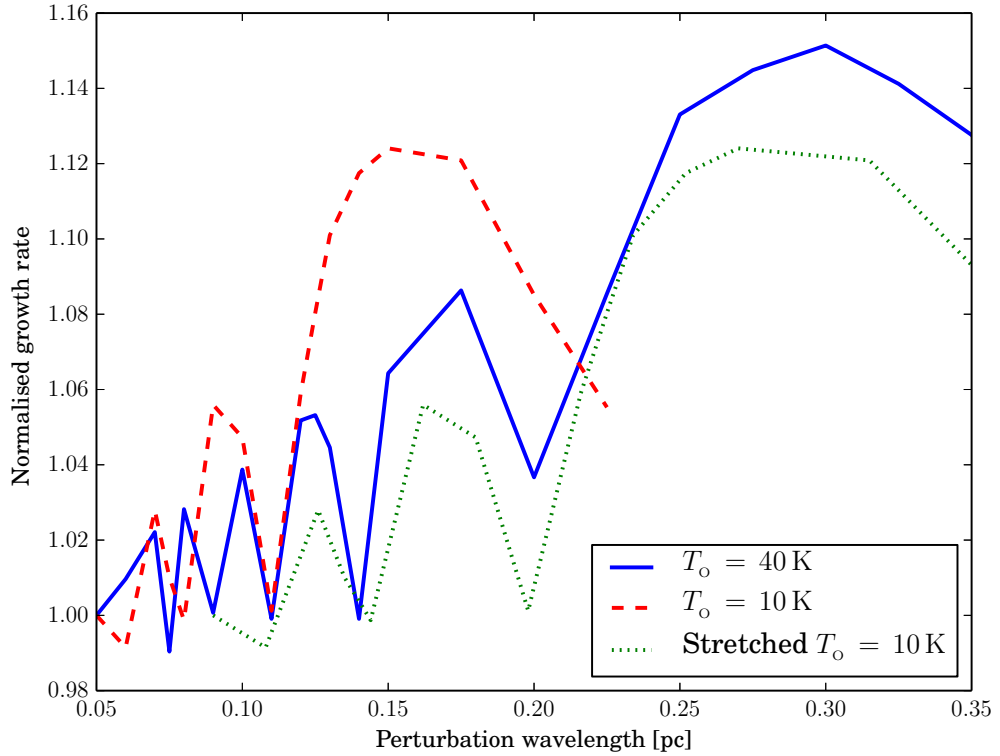


Figure 4.5. The dispersion relation between perturbation wavelength and normalised growth rate for the fiducial case ($T_o = 40 \text{ K}$), and for the case with $T_o = 10 \text{ K}$. The normalised growth rate is defined as $\hat{g}_\lambda = g_\lambda / g_{0.05\text{pc}}$. The fiducial case (solid blue line) and the case with the lower temperature (dashed red line) are out of phase. The lower temperature has caused the relation to be squeezed in the x-direction. The green dotted line is the result of stretching the $T_o = 10 \text{ K}$ line assuming the dispersion relation takes the form $g_\lambda = f'(\lambda/a_o)$, where a_o is the isothermal sound speed. The peaks in the stretched dispersion relation now line up with those from the fiducial case.

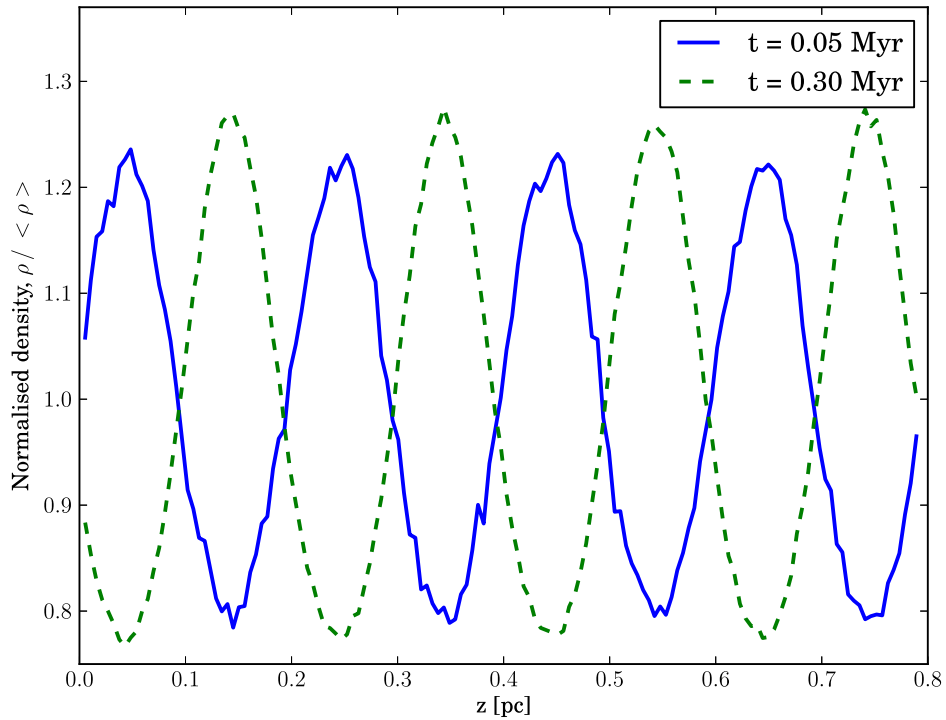


Figure 4.6. The normalised volume-density profile, $\rho / \langle \rho \rangle$, along the z -axis for the fiducial case at two different times, $t = 0.05$ Myr (blue solid line) and $t = 0.30$ Myr (green dashed line). A standing gravo-acoustic wave is set up along the filament's length; the locations of the initial density peaks are the anti-nodes of the wave. The density peaks and trough switch after 0.25 Myr has passed, i.e. half an oscillation period.

amplitude of the density peak is decreased as mass has moved into what once was a trough. These two effects cause the collapse of the perturbation to proceed more slowly once the filament has become super-critical, resulting in a significantly lower growth rate. Conversely, the peaks are caused by the longitudinal motions converging on a density peak at the time of radial collapse, when the perturbation is reaching its peak amplitude.

One can write an equation to predict the positions of the peaks in the dispersion relation by considering when the oscillation period and the time at which the filament becomes supercritical, τ_{CRIT} , are in phase. For the two to be in phase requires

$$\tau_{\text{CRIT}} \sim n\tau_{\text{HALF OSCILLATION}}, \quad (4.5)$$

where n is a positive integer and

$$\tau_{\text{HALF OSCILLATION}} = \frac{\lambda}{2a_{\text{O}}}. \quad (4.6)$$

Hence

$$\lambda_{\text{DOM},n} \sim \frac{2\tau_{\text{CRIT}}a_{\text{O}}}{n}. \quad (4.7)$$

At $T_{\text{O}} = 40$ K the isothermal sound speed, a_{O} , is 0.37 km/s, and taking τ_{CRIT} as 0.45 Myr, we expect the dispersion relation to show peaks at $\lambda_{\text{DOM},n} = 0.33, 0.17, 0.11, \dots$ corresponding to $n = 1, 2, 3, \dots$. We see the $n \leq 6$ peaks in figure 4.3 where equation 4.7 predicts. The dominant wavelength, the one that grows most quickly, is the $n = 1$ peak (figure 4.3).

This dominant wavelength, λ_{DOM} , is defined by a resonance between the timescale, τ_{CRIT} on which the line density of the filament approaches the critical value for radial collapse, and the timescale on which the longitudinal oscillations of the perturbation complete a half oscillation, $\tau_{\text{HALF OSCILLATION}}$, so that both motions act to enhance the perturbation - i.e. both radial and longitudinal flows are converging.

From equation 4.7 one can see that if the temperature, and hence the sound speed, a_{O} , are kept constant, and the mass influx per unit length, $\dot{\mu}$, is increased, the dominant wavelength decreases because τ_{CRIT} has been reduced (see figure 4.4). Conversely if τ_{CRIT} is kept constant, and the temperature and sound speed are decreased, the dominant wavelength again decreases, but now because the timescale to complete half a longitudinal oscillation has been increased (see figure 4.5).

As the oscillations are acoustic in nature and are dependent on the sound speed it is not clear yet if they will survive in the presence of turbulence. However, it has been shown that filaments are decoupled from the supersonic medium surrounding

them and appear to only contain sub-sonic motions (Hacar & Tafalla, 2011; Hacar et al., 2016), which may lead to only a small correction to the model presented here. This will be examined in chapter 5.

As noted above, the dispersion relation (figure 4.3) shows that there is an upwards trend in growth rate with increasing wavelength, longer wavelength perturbations grow faster than shorter wavelength perturbations. This can be explained in terms of the Jeans length. The Jeans length is applicable because the perturbations are roughly spherical as they approach instability, as also observed by Inutsuka & Miyama (1997). For a perturbation to be unstable and collapse its length must be greater than the Jeans length, $\lambda_J = a_o(\pi/G\rho)^{1/2}$. Smaller wavelength perturbations must therefore reach higher densities before they become unstable, and this delays their growth.

4.4.1 MULTI-WAVELENGTH PERTURBATIONS

I now apply my analysis to filaments which are seeded with perturbations at multiple wavelengths, in order to investigate whether the dispersion relation continues to hold true. I use initial conditions informed by the work of Roy et al. (2015), who find that the power spectrum of density perturbations in interstellar filaments is well described by a power law with an index of $\alpha = -1.6 \pm 0.3$.

I have performed a set of simulations whose initial longitudinal density profile is characterised by such a power law. I perform ten realisations with an index of $\alpha = -1.3$, ten with $\alpha = -1.6$ and ten with $\alpha = -1.9$. So as to compare the results to the dispersion relation (figure 4.3) in section 4.3, I take $T_o = 40$ K, the computational domain is set to 1 pc, $\dot{\mu} = 70 M_\odot \text{ pc}^{-1} \text{ Myr}^{-1}$, the maximum amplitude perturbation has $A = 0.2$, the same radial density and velocity profiles are used, and the $k = 1$ mode has an amplitude of 0. We set the amplitude of the $k = 1$ mode to zero as it corresponds to a wavelength of 1 pc, beyond the range of perturbation wavelengths considered in the previous section.

Figure 4.8 shows the longitudinal density profile for one of the $\alpha = -1.6$ simulations at $t = 0.05$ Myr and $t = 0.56$ Myr (just before the first sink forms). The density peaks are roughly periodic at $t = 0.56$ Myr despite there being no obvious indication of it in the initial conditions. This suggests that there exists a preferential length scale for fragmentation.

I determine the core separations for each set of simulations and plot the histograms in figure 4.9. Separation distances below 0.05 pc have been removed; in a number of simulations a few cores form very close together, with separations ~ 0.02 pc,

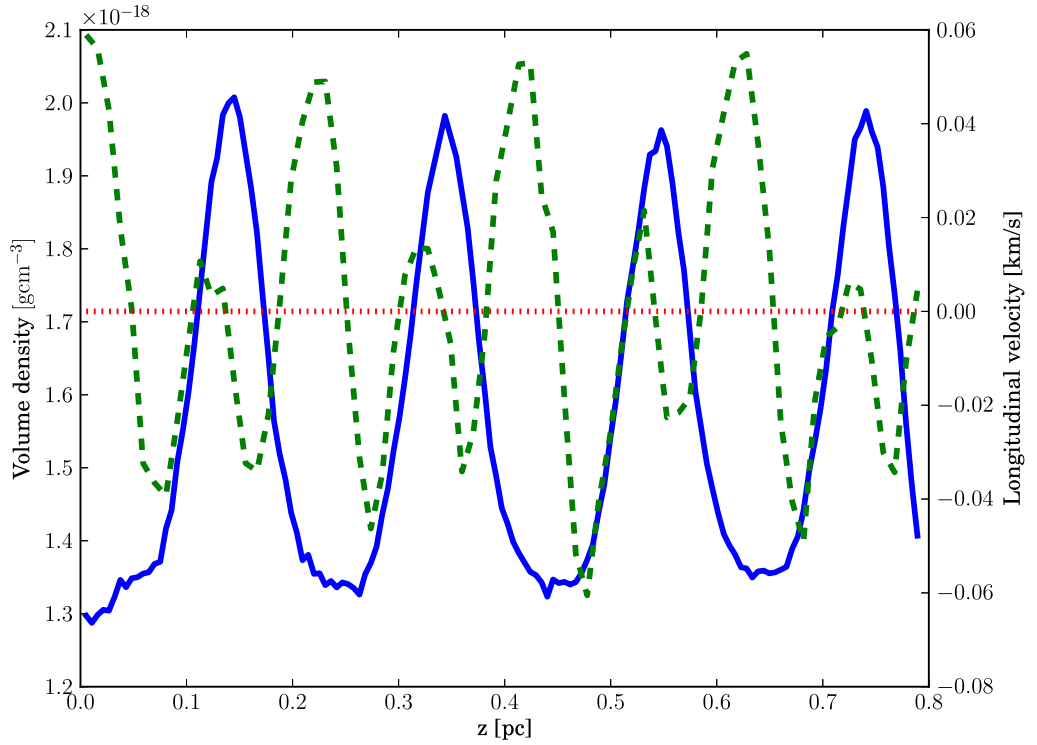


Figure 4.7. The longitudinal density (blue solid line) and velocity (green dashed line) profiles at $t = 0.45$ Myr for the simulation with $\lambda = 0.2$ pc, $T_{\text{O}} = 40$ K, $\dot{\mu} = 70 M_{\odot} \text{pc}^{-1} \text{Myr}^{-1}$ and $A = 0.2$. This is the time at which the perturbations are just becoming self-gravitating and the filament is close to becoming globally super-critical. The red dotted line is the $v = 0$ km/s line, which is included to help the reader see the converging and diverging regions along the filament. The velocity field is out of phase with the density field, and the main converging flows are positioned where the troughs of the density profile are. Because of this the majority of the gas is moving away from the density peaks just as radial collapse is about to begin. There are small converging flows at the central density peaks because these regions have just become self-gravitating.

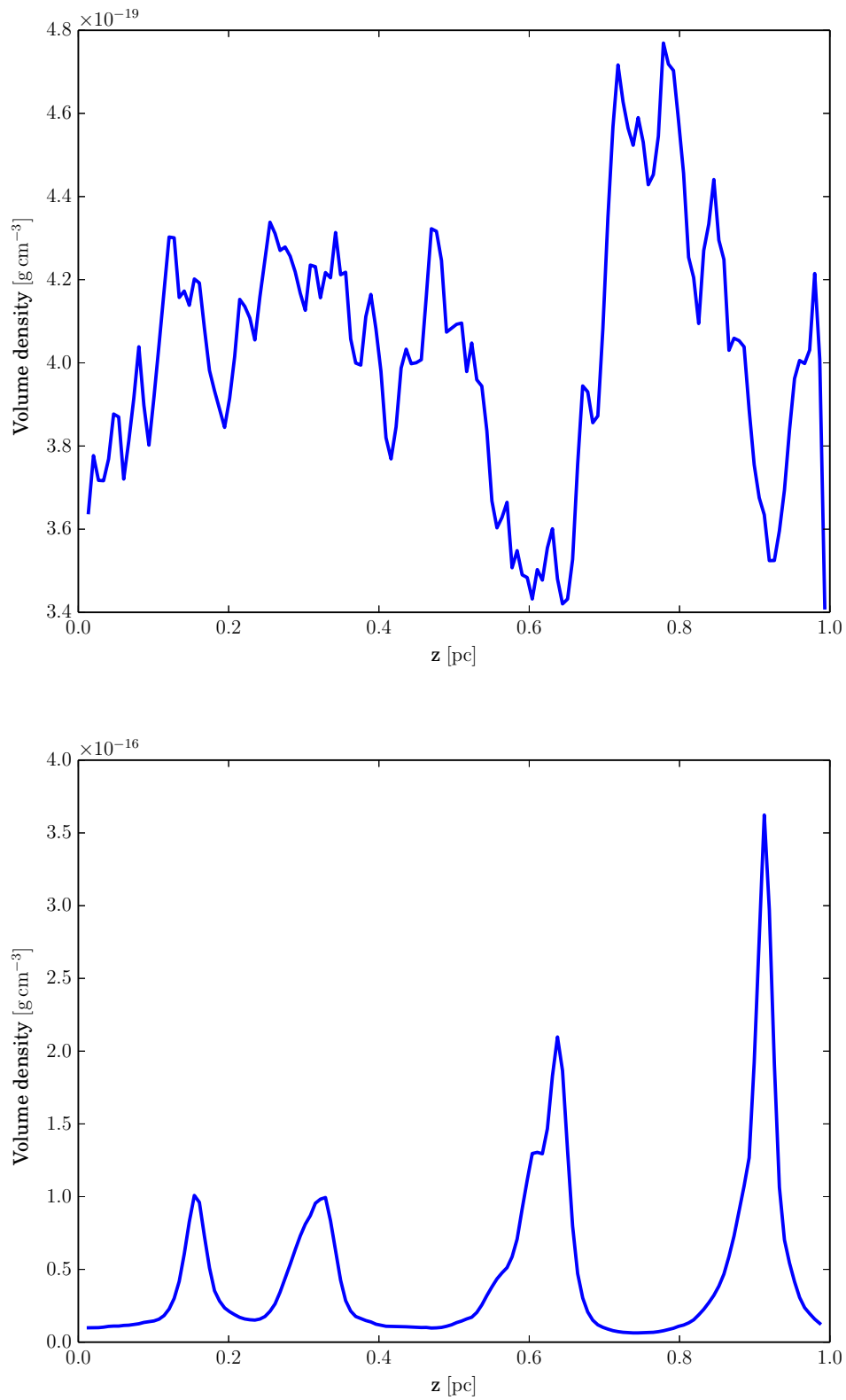


Figure 4.8. The longitudinal density profile for one of the $\alpha = -1.6$ simulations at $t = 0.05$ Myr (top) and $t = 0.56$ Myr (bottom). The density peaks (cores) at $t = 0.56$ Myr, are roughly periodically spaced, having an average separation of 0.24 pc.

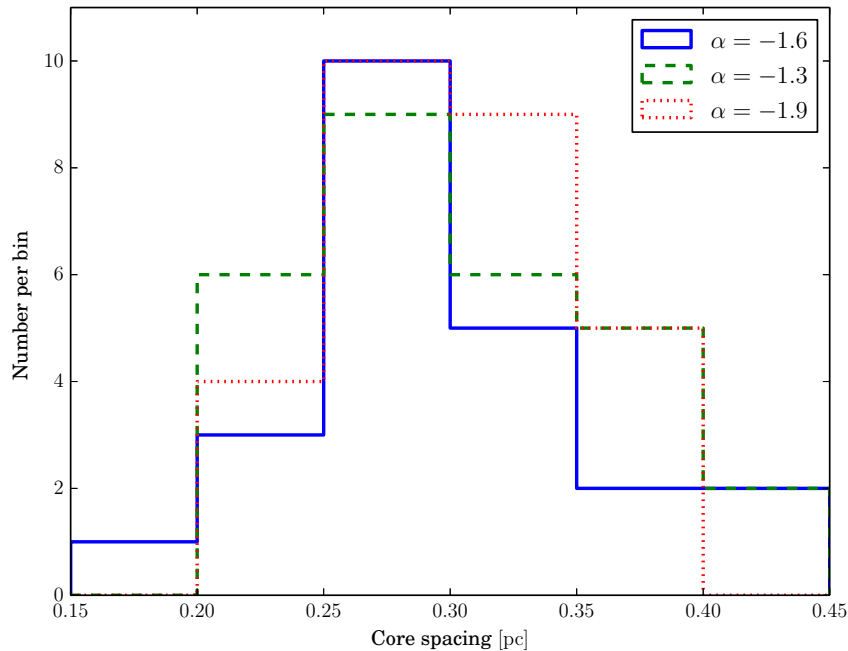


Figure 4.9. Histograms showing the distribution of core spacings in a set of 30 simulations. The blue line shows the core spacings for the ten simulations where $\alpha = -1.6$, the green line shows the core spacings from the ten simulations where $\alpha = -1.3$ and the red line shows the core spacing for the ten simulations where $\alpha = -1.9$. Spacings below 0.05 pc were removed; in a number of simulations a few cores form very close together, ~ 0.02 pc, these clusters are then separated by much greater distances. The change in power index does not affect the distribution, all three distributions are strongly peaked at ~ 0.3 pc. Considering all 30 simulations together, a sample of 114 spacings, the distribution has a mean of 0.296 pc and a standard deviation of 0.070 pc

and these clusters of cores are then separated by much greater distances.

Changing the index of the power-law index does not appear to affect the distribution of core separations, all three are sharply peaked at ~ 0.3 pc. As the value of α does not have a strong effect on the distribution we combine the data from all 30 simulations, this leads to a sample of 114 spacings with a mean of 0.296 pc and a standard deviation of 0.070 pc.

The peak in core separations corresponds to the $n = 1$ peak in the dispersion relation (figure 4.3); even though there is initially greater power in other modes, it is the wavelength with the fastest growth rate which determines the fragmentation length scale.

My simulations suggest that one could estimate a lower age limit for a filament which is fragmenting periodically by measuring the average core separation distance.

Equation 4.7 can be re-written as,

$$\tau_{\text{AGE}} \geq \tau_{\text{CRIT}} \simeq \frac{\lambda_{\text{CORE}}}{2a_{\text{O}}}. \quad (4.8)$$

This is a lower limit on the filament's age, as one does not know how much time has elapsed between when the cores formed and when the filament is observed. One can also estimate the average accretion rate that the filament experienced during its assembly, $\dot{\mu} = \mu_{\text{CRIT}}/\tau_{\text{CRIT}} = 2a_{\text{O}}\mu_{\text{CRIT}}/\lambda_{\text{CORE}}$. A filament which has closely spaced cores is likely to have experienced a very high accretion rate and vice versa.

Tafalla & Hacar (2015) find that there exists a preferential core separation of ~ 0.2 pc in the sub-filaments making up the L1495/B213 complex in Taurus. Taking a gas temperature of 10 K and assuming solar metallicity, the sound speed is 0.19 km/s. This results in a minimum age for these sub-filaments of 0.53 Myr. The critical line density at this temperature is $16.7 M_{\odot} \text{ pc}^{-1}$. Therefore we infer that the average accretion rate during the filament's formation was $\sim 32 M_{\odot} \text{ pc}^{-1} \text{ Myr}^{-1}$, in agreement with the accretion rate inferred observationally by Palmeirim et al. (2013), $27 - 50 M_{\odot} \text{ pc}^{-1} \text{ Myr}^{-1}$.

Williams et al. (in prep.) show that the north-west filament of the cloud SDC13 exhibits periodic fragmentation, the cores spaced roughly 0.4 pc apart. Using the work presented here, they suggest that the filament is at least 1 Myr old, and experienced an average accretion rate of $\sim 50 M_{\odot} \text{ pc}^{-1}$.

Another filament which has fragmented into roughly periodically spaced cores is IRDC 18223 (as can be seen in figure 3.13.) Beuther et al. (2015) find that the cores are spaced roughly 0.4 pc apart. Taking a gas temperature of 15 K (Beuther et al., 2015) and assuming solar metallicity the sound speed is 0.23 km/s. This results in a minimum age for IRDC 18223 of 0.87 Myr. This is consistent with the minimum age determined by considering the contrast ratio (section 3.4.2.)

However, IRDC 18223 has a line density of $\sim 1000 M_{\odot} \text{ pc}^{-1}$, around 40 times greater than the critical line density due to thermal pressure alone. This suggests that an additional support mechanism exists. The observed line of sight velocity dispersion in IRDC 18223 is ~ 1.0 km/s, taking this as a purely supportive turbulent pressure yields a critical line mass of $\sim 400 M_{\odot} \text{ pc}^{-1}$. As IRDC 18223 is clearly undergoing radial collapse, as evidenced by the presence of cores, it is likely that a significant portion of the observed line of sight velocity dispersion may be caused by the radial collapse of the gas, and not due to supporting turbulence. Thus $\mu_{\text{CRIT}} \sim 400 M_{\odot} \text{ pc}^{-1}$ should be considered as an optimistic upper limit. Another mechanism is magnetic fields, these can provide a supporting pressure against radial collapse, but only if

they are aligned parallel to the long axis of the filament (Seifried & Walch, 2015). If the field is aligned parallel to the long axis it will have relatively little effect on longitudinal motions. As the strength of the magnetic field is unknown, one can not know the critical line density for IRDC 18223. I find the maximum average accretion rate since formation by using the observed line density, $\dot{\mu} = \mu_{\text{OBS}}/\tau_{\text{CRIT}} = 2a_{\text{O}}\mu_{\text{OBS}}/\lambda_{\text{CORE}}$. This yields an accretion rate of $\sim 1150 M_{\odot} \text{ pc}^{-1} \text{ Myr}^{-1}$, considerably larger than accretions rates onto more local filaments but similar to those seen in simulations and observations of large scale colliding flows (Peretto et al., 2013; Balfour et al., 2015, Balfour private comm.).

4.5 SUMMARY

Filament fragmentation is a complex phenomenon. I have shown that the sub-critical accretion phase in a filament's evolution strongly influences the growth of the perturbations which lead to fragmentation. During the sub-critical accretion phase the thermal pressure term dominates over gravity and sets up standing gravo-acoustic oscillations, leading to a series of oscillations in the dispersion relation linking perturbation growth rate and perturbation wavelength.

The fastest growing mode in an evolving filament is no longer simply linked to the diameter of a filament (as shown to be the case for equilibrium filaments by Inutsuka & Miyama, 1992). Instead it is dependent on the temperature and the accretion rate onto the filament, because the fastest growing wavelength is the one for which there is a resonance between the timescale on which the filament becomes super-critical and the period of the longitudinal oscillations. I have shown that this dependence holds when filaments are seeded with a multi-wavelength density power spectrum. Moreover, the results are insensitive to the exact power law index in the range of indices ($-1.3 \leq \alpha \leq -1.9$) observed by Roy et al. (2015).

These results allow observers to constrain the age of a filament which is breaking up into regularly spaced fragments, as well as its accretion history. I have applied this model to the sub-filaments making up the L1495/B213 complex in Taurus, and IRDC 18223. I find minimum ages of 0.53 Myr and 0.87 Myr respectively. As the sub-filaments in Taurus appear to be predominately supported by thermal pressure, I find an average accretion rate during their sub-critical phase of $\sim 32 M_{\odot} \text{ pc}^{-1} \text{ Myr}^{-1}$, in agreement with observations by Palmeirim et al. (2013). IRDC 18223 is likely to be magnetically supported, and assuming the magnetic field is parallel to the long axis, I find a maximum average accretion rate over the filament's entire history of $\sim 1150 M_{\odot} \text{ pc}^{-1} \text{ Myr}^{-1}$, consistent with observations and simulations of large scale

colliding flows.

CHAPTER 5

FILAMENTARY FRAGMENTATION IN A TURBULENT MEDIUM *

In this chapter I present the results of smoothed particle hydrodynamic simulations investigating the evolution and fragmentation of filaments that are accreting from a turbulent medium. I show that the presence of turbulence, and the resulting inhomogeneities in the accretion flow, play a significant role in the fragmentation process. Filaments which experience a weakly turbulent accretion flow fragment in a two-tier hierarchical fashion, similar to the fragmentation pattern seen in the Orion Integral Shaped Filament. Increasing the energy in the turbulent velocity field results in more sub-structure within the filaments, and one sees a shift from gravity-dominated fragmentation to turbulence-dominated fragmentation. The sub-structure formed in the filaments is elongated and roughly parallel to the longitudinal axis of the filament, similar to the fibres seen in observations of Taurus, and suggests that the fray and fragment scenario is a possible mechanism for the production of fibres. I show that the formation of these fibre-like structures is linked to the vorticity of the velocity field inside the filament and the filament's accretion from an inhomogeneous medium. Moreover, I find that accretion is able to drive and sustain roughly sonic levels of turbulence inside the filaments, but is not able to prevent radial collapse once the filaments become supercritical. However, the supercritical filaments which contain fibre-like structures do not collapse radially, suggesting that fibrous filaments may not necessarily become radially unstable once they reach the critical line-density.

*The work presented here has been submitted to MNRAS

5.1 INTRODUCTION

Previous work has shown that filaments are prone to fragmentation due to their geometry; small-scale density perturbations have time to collapse locally before global longitudinal collapse occurs (Pon, Johnstone & Heitsch, 2011). Inutsuka & Miyama (1992) have performed an analytic perturbation analysis to investigate how small-scale density perturbations grow in equilibrium filaments. They find that the most unstable perturbation has a wavelength roughly four times the filament's diameter.

However, it is unlikely that a filament forms, stops accreting, relaxes to equilibrium and then proceeds to fragment. Instead, the filament and perturbations will co-evolve during a non-equilibrium accretion stage until the filament becomes unstable and fragments. This scenario was investigated in the previous chapter. In chapter 4 I show that the fastest growing mode is the result of a resonance between radial accretion and longitudinal oscillations. The dominant wavelength is given by

$$\lambda_{\text{DOM}} \sim 2\tau_{\text{CRIT}} a_{\text{O}}, \quad (5.1)$$

where τ_{CRIT} is the time at which the filament becomes radially unstable and a_{O} is the isothermal sound speed.

This fastest growing mode continues to be the dominant mode in simulations seeded with perturbations at multiple wavelengths. Moreover, the fastest growing mode is linked to the environment of the filament, its temperature and its accretion rate. This allows observers to determine the age, τ_{AGE} , and mean accretion rate, $\langle \dot{\mu} \rangle$, of a filament which is fragmenting in a roughly periodic manner,

$$\tau_{\text{AGE}} \geq \tau_{\text{CRIT}} \simeq \frac{\lambda_{\text{CORE}}}{2a_{\text{O}}}, \quad (5.2)$$

and

$$\langle \dot{\mu} \rangle \simeq \frac{2a_{\text{O}}\mu}{\lambda_{\text{CORE}}}, \quad (5.3)$$

where λ_{CORE} is the measured core separation and μ is the filament's line-density.

Tafalla & Hacar (2015) have recently observed the star forming filament L1495 in Taurus, and find that it can be decomposed into velocity-coherent sub-filaments, which they term 'fibres'. On the basis of these results, they propose that filaments first fragment into fibres and that these fibres then go on to fragment into cores, a model they call *fray and fragment*. Recent simulations by Smith, Glover & Klessen (2014) suggest that fibres do not form from the fragmentation of filaments, but rather form in the surrounding cloud and are then swept up by large scale motions to form a single column density structure. At present it is unclear which mechanism is dominant, or

what role fibres play in filamentary fragmentation.

In this chapter, I present numerical simulations of initially sub-critical filaments which accrete from a turbulent medium. Unlike the simulations presented in the previous chapter in which density perturbations were placed in the accretion flow, the simulations in this chapter use a turbulent velocity field to seed density perturbations. In Section 5.2, I detail the simulation setup and the initial conditions used; in Section 5.3 I present the results of these simulations; in Section 5.4, I discuss the significance of these results and compare them with previous work and observations; and in Section 5.5, I summarise my conclusions.

5.2 NUMERICAL SETUP

The simulations presented in this chapter are performed using the Smoothed Particle Hydrodynamics (SPH) code GANDALF (Hubber et al. in prep.). The simulations invoke both self-gravity and hydrodynamics, with an isothermal equation of state. T_{O} is taken to be 40 K throughout so as to compare to the fiducial case presented in the previous chapter; this results in an isothermal sound speed of ~ 0.37 km/s, assuming solar metallicity. Grad-h SPH (Price & Monaghan, 2004) is implemented, with $\eta = 1.2$, so that a typical particle has ~ 58 neighbours.

Sink particles are implemented as described in subsection 2.9.1 using the sink creation density, $\rho_{\text{SINK}} = 10^{-15} \text{ g cm}^{-3}$. The simulations have been tested with sink creation densities ranging from $10^{-12} \text{ g cm}^{-3}$ to $10^{-17} \text{ g cm}^{-3}$, and are well converged with a sink creation density of $10^{-15} \text{ g cm}^{-3}$.

The computational domain is open in the x - and y - directions, but periodic in z , the long axis of the filament (see Wünsch et al. in preparation, for the implementation of the modified Ewald field). This allows us to study the fragmentation of an infinitely long filament, and ignore the complicating effects of global longitudinal collapse (see chapter 3).

To generate the initial conditions, a cylindrical settled glass of particles with uniform density is stretched so that it reproduces the density profile,

$$\rho(r, z) = \frac{\rho_{\text{O}} r_{\text{O}}}{r}. \quad (5.4)$$

Here, ρ_{O} is the density at $r_{\text{O}} = 0.1 \text{ pc}$. Note that this is a uniform density profile in the longitudinal z direction. The particles are stretched using the same method as explained in the previous chapter. The $1/r$ density profile is chosen to produce a

mass accretion rate which is radially independent. The initial velocity field is

$$\mathbf{v} = -v_{\circ}\hat{\mathbf{r}} + \mathbf{v}_{\text{TURB}}. \quad (5.5)$$

The first term of the velocity field is identical to the field used in the previous chapter, a radially convergent velocity field to model the formation of a filament. The second term is a turbulent velocity field which is added to the gas to seed density perturbations. The characteristics of this turbulent field are discussed below in section 5.2.1.

Values of $\rho_{\circ} = 150 \text{ M}_{\odot} \text{ pc}^{-3}$ and $v_{\circ} = 0.75 \text{ km/s}$ are used, as these are the fiducial values used in the previous simulations; this corresponds to a mass accretion rate onto the filament of $\sim 70 \text{ M}_{\odot} \text{ pc}^{-1} \text{ Myr}^{-1}$, consistent with accretion rates inferred observationally (Palmeirim et al., 2013; Kirk et al., 2013).

The turbulent cylinder of particles has a radius of $r_{\text{MAX}} = 1 \text{ pc}$ and a length of $L = 3 \text{ pc}$. This provides a sufficiently large computational domain to allow us to study a wide range of possible perturbation wavelengths, while maintaining good resolution. The open vacuum boundary conditions in the x and y directions mean that those particles at the edge of the cylinder, $r \sim r_{\text{MAX}}$, experience an outwards pressure force. This boundary effect has no impact on the results due to the choice of r_{MAX} . Given $v_{\circ} = 0.75 \text{ km/s}$, those particles that are located at $\sim r_{\text{MAX}}$ require $\sim 1.3 \text{ Myr}$ to reach the filament formed at the z -axis, as the simulations take at most 0.75 Myr those particles would never reach the filament during the simulation time even without the boundary effect.

Artificial viscosity is needed to capture shocks, but it is known to overly dampen motions on the order of the smoothing length. Therefore, the simulations use the time-dependent artificial viscosity described in Morris & Monaghan (1997) to lessen this effect.

After the first sink particle forms, the simulations run until the sinks have accreted roughly 10% of the initial gas mass. After this time, feedback mechanisms such as protostellar jets are expected to play an important role, and, as these processes are not modelled, the simulations are terminated.

The simulations are run with 450,000 particles; each SPH particle has a mass of $6.3 \times 10^{-4} \text{ M}_{\odot}$, giving a conservative mass resolution of $6.3 \times 10^{-2} \text{ M}_{\odot}$. Tests with different numbers of particles show that the simulations are converged.

5.2.1 TURBULENT VELOCITY FIELDS

The initial turbulent velocity field, \mathbf{v}_{TURB} , is generated using the procedure described in Lomax, Whitworth & Hubber (2015). The turbulent velocity field is defined by a power spectrum, $P(k) \propto k^{-\alpha}$, where k is the velocity mode's wavenumber. Burgers turbulence, $\alpha = 4$, is appropriate for highly supersonic turbulence, while $\alpha = 11/3$, known as Kolmogorov turbulence, is appropriate for subsonic turbulence in an incompressible fluid. For a compressible fluid with transonic turbulence, the exponent is expected to lie between these two values. In both the Burgers and Kolmogorov cases, the majority of the power lies in the small wavenumber, large wavelength modes and so the exact choice of exponent is not very significant. This is shown to be the case when the exponent is greater than 3 in prestellar core simulations presented by Walch et al. (2012). For this work we use $\alpha = 4$.

I do not include the longest wavelength modes in the x and y directions, $\mathbf{k} = (1, 0, 0)$ and $(0, 1, 0)$, as the first term of equation 5.5 can be considered as an imposed velocity mode in those directions.

I do consider the effect that the ratio of compressive to solenoidal kinetic energy has on filament fragmentation. Purely compressive turbulence is defined as a curl-free velocity field and purely solenoidal turbulence is defined as a divergence-free velocity field. A velocity field with a userdefined ratio of compressive to solenoidal kinetic energy can be constructed using Helmholtz's theorem (see §2.1.3 of Lomax, Whitworth & Hubber (2015) for more details). I consider two cases, purely compressive and a 'natural' mix, i.e. where the solenoidal modes have twice the power of the compressive modes. In the nomenclature used by Lomax, Whitworth & Hubber (2015) these two cases correspond to $\delta_{\text{sol}} = 0$ and $\delta_{\text{sol}} = 2/3$ respectively.

A turbulent field is defined by its power spectrum, which determines the distribution of energy as a function of wavenumber, and the three dimensional velocity dispersion, $\sigma_{3\text{D}}$, which determines the total amount of energy in the velocity field. We consider three cases, $\sigma_{3\text{D}} = 0.1, 0.4, 1.0$ km/s, which correspond to Mach numbers of $\mathcal{M} \sim 0.25, 1, 2.5$ respectively.

Each turbulent field is generated using a random number seed, and I have performed 10 realisations of each pair of parameters, δ_{sol} and $\sigma_{3\text{D}}$, resulting in a total of 60 simulations.

5.3 RESULTS

The turbulent field produces density perturbations on many different length scales within the filament (for one example see figure 5.1). In all simulations, the

filament is sub-critical during early times and has a typical width of ~ 0.1 pc. Gas continues to accrete onto the filament, until it reaches the critical line density and the regions of high density, formed due to the turbulent velocity field, collapse to form sink particles.

To study the fragmentation of a filament I work out the sink separation at the end of the simulation when 10% of the mass is in sink particles. For each pair of parameters, δ_{sol} and σ_{3D} , I work out the sink separations for all 10 realisations to produce a separation distribution. All separations which are below 0.02 pc are removed; this is to remove the effects of the multiple systems produced at some core locations. Visually inspecting the simulations, there is no evidence of scattering of sink particles from these multiple systems. Figure 5.2 shows the histograms of the separation distributions for the natural-mix turbulence, $\delta_{\text{sol}} = 2/3$, and figure 5.3 shows the same information for the purely compressive turbulence, $\delta_{\text{sol}} = 0$.

All 6 histograms seen in figures 5.2 and 5.3 show a more complicated distribution than that found in chapter 4 (figure 4.9); turbulence has thus altered the fragmentation of the filaments considerably.

For the subsonic case (figures 5.2a and 5.3a), the distributions from the natural mix and purely compressive turbulence share the same morphology. Both core separation distributions show two peaks at the same locations, one at ~ 0.1 pc and the other at ~ 0.5 pc. The small insets show the small scale separations, < 0.3 pc, in more detail for both values of δ_{sol} . Here one can see that there is a small difference in the two distributions, the natural mix produces a peak just above 0.1 pc, while the purely compressive turbulence produces a peak just below 0.1 pc.

The transonic case (figures 5.2b and 5.3b) is more complicated. The natural mix turbulence has a wide range of core separations and a peak at ~ 1 pc. The purely compressive turbulence produces a bimodal distribution with peaks at ~ 0.5 pc and ~ 1.2 pc.

The supersonic case (figures 5.2c and 5.3c) produces two very different distributions. The natural mix turbulence causes a number of filaments to only form one core (the large peak in core separations at 3 pc), those that do fragment into numerous cores do so with a wide range of separation distances with a peak ~ 1.2 pc. More filaments fragment into multiple cores when the turbulence is purely compressive, and those that do, do so with a bimodal distribution with peaks at ~ 1.5 pc and ~ 0.1 pc.

The results of individual simulations are summarised in tables 5.2 - 5.4 at the end of the chapter. These tables show the time at which the first sink particle forms, t_{sink} , the time the simulation ended when 10% of the mass is in the form of sinks, $t_{10\%}$, the difference between these times, Δt , and the number of sinks formed by the

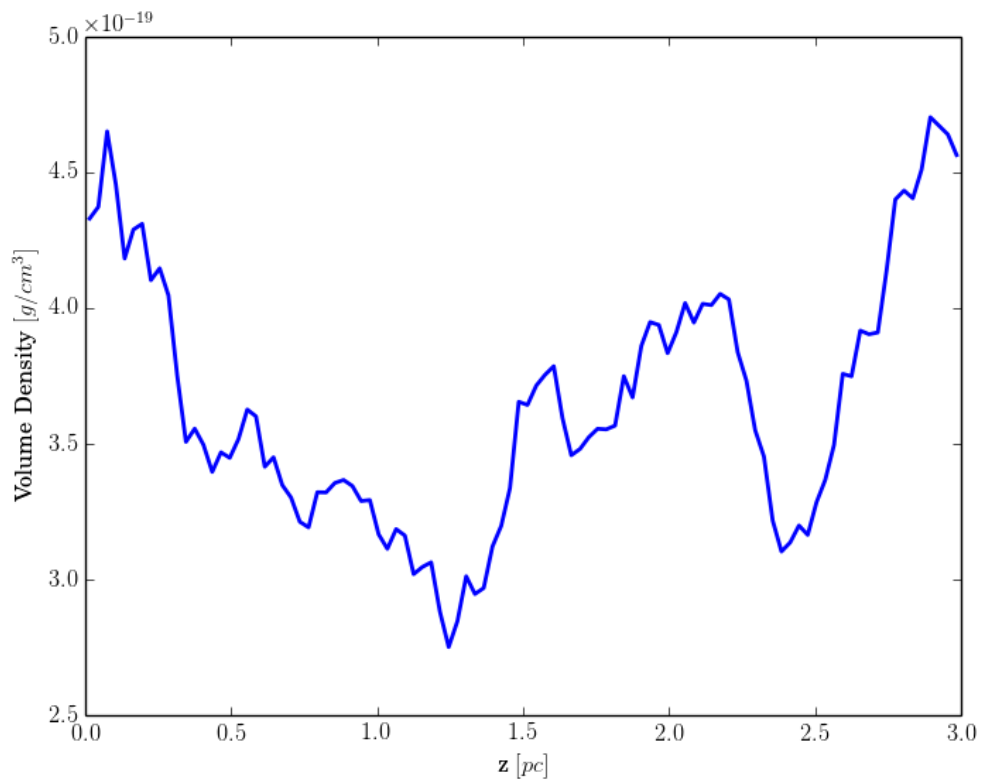


Figure 5.1. The volume density profile along the z -axis at $t = 0.4$ Myr showing density perturbations on many different scales. The turbulent field has a natural mix of compressive and solenoidal modes, $\delta_{\text{sol}} = 2/3$, and a subsonic velocity dispersion, $\sigma_{3\text{D}} = 0.1$ km/s.

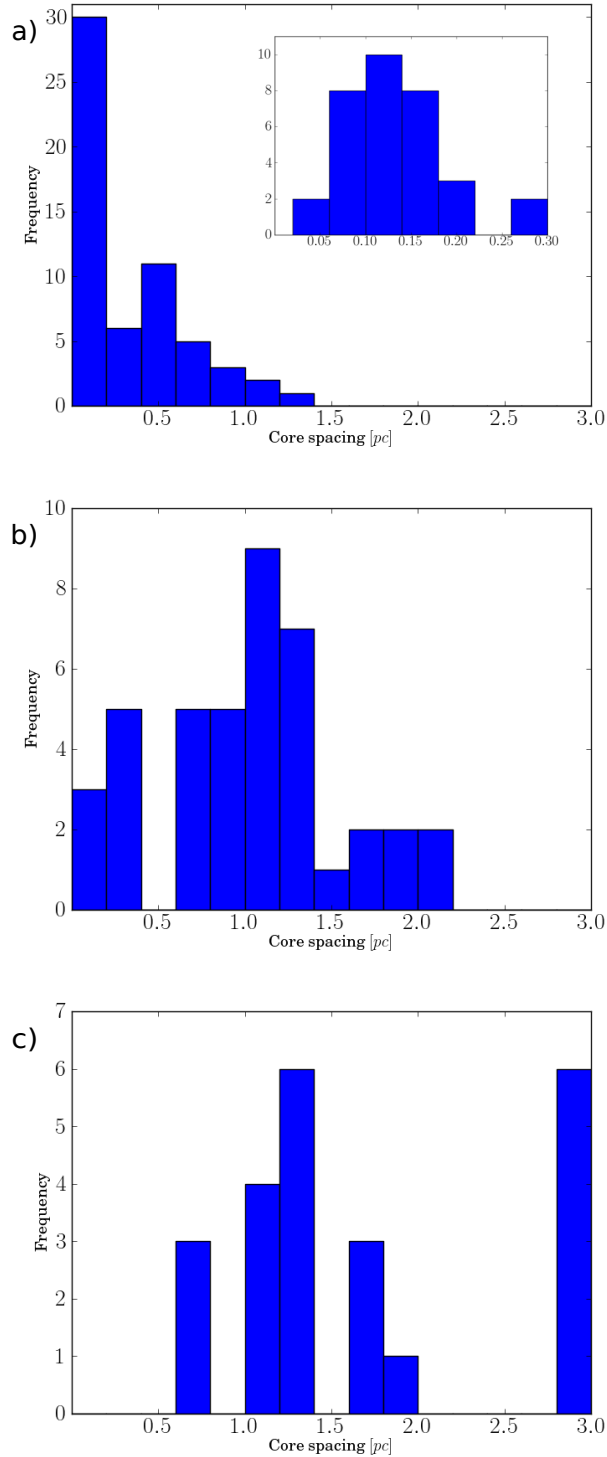


Figure 5.2. Histograms showing the distribution of core separation distances for the set of simulations initialized with a natural mix of turbulence, $\delta_{\text{sol}} = 2/3$, for (a) $\sigma_{3D} = 0.1$ km/s, (b) $\sigma_{3D} = 0.4$ km/s and (c) $\sigma_{3D} = 1$ km/s. Figures a, b and c have 58, 41 and 23 separations respectively. The sub-sonic case (a) has an inset to show the distribution of small scale separations (< 0.3 pc) in more detail. Note that a separation of 3 pc is recorded when the filament has only produced one core.

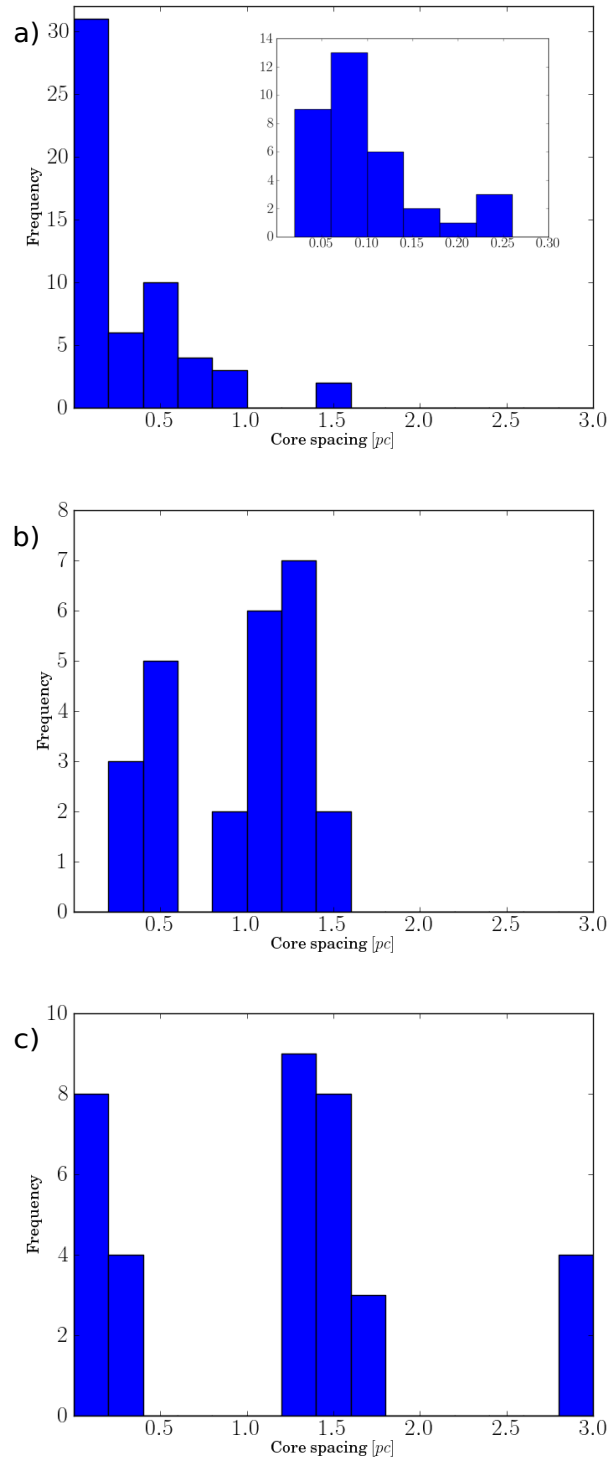


Figure 5.3. Histograms showing the distribution of core separation distances for the set of simulations initialized with purely compressive turbulence, $\delta_{\text{sol}} = 0$, for (a) $\sigma_{3D} = 0.1$ km/s, (b) $\sigma_{3D} = 0.4$ km/s and (c) $\sigma_{3D} = 1$ km/s. Figures a, b and c have 56, 25 and 36 separations respectively. The sub-sonic case (a) has an inset to show the distribution of small scale separations (< 0.3 pc) in more detail. Note that a separation of 3 pc is recorded when the filament has only produced one core.

end of the simulation, N_{sink} . Also shown is the mean and standard deviation of these statistics.

5.4 DISCUSSION

The nature of the turbulence plays an important role in the fragmentation of a filament when the turbulence is transonic or supersonic. Compressive turbulence produces narrower and more clearly defined core separation distributions, and so is more likely to lead to quasi-periodically fragmented filaments. Natural turbulence produces wider distributions with less well defined peaks.

5.4.1 INITIALLY SUBSONIC TURBULENCE

For subsonic turbulence, the nature of the turbulence does not play a significant role in the fragmentation. Both cases show bimodal distributions, neither peak corresponding to that suggested by the most unstable mode of a filament, given by equation 5.1. Taking $a_o = 0.37$ km/s and $\tau_{\text{CRIT}} = 0.45$ Myr, one would expect to see a peak at ~ 0.3 pc. These are the values for the fiducial case in the previous chapter, which share the same accretion rate and temperature as the simulations presented here. However, equation 5.1 uses the isothermal sound speed which is likely to be inappropriate in a turbulent environment. In the presence of turbulence, one ought to use the effective sound speed defined as $a_{\text{EFF}} = \sqrt{a_o^2 + \sigma_{1D}^2}$, where σ_{1D} is the one-dimensional velocity dispersion. For isotropic turbulence, $\sigma_{1D} = \sigma_{3D}/\sqrt{3}$, where σ_{3D} is the three-dimensional velocity dispersion. Changing a_o for a_{EFF} in equation 5.1, the most unstable mode in a turbulent filament is given by

$$\lambda_{\text{DOM}} \sim 2\tau_{\text{CRIT}} a_{\text{EFF}}. \quad (5.6)$$

To calculate the three-dimensional velocity dispersion within a filament one must first define the edge of the filament. This is done by finding the azimuthally and longitudinally averaged radial profile of the filament and determining the radius at which the density profile blends into the background profile; for these simulations that is when $\rho \propto r^{-1}$, the initial accretion flow's density profile given by equation 5.4. All SPH particles which lie within this bounding radius are considered to be part of the filament. The three-dimensional velocity dispersion is calculated using velocities in the cylindrical co-ordinate system, (r, θ, z) ; this is done to avoid artificially high velocity dispersions when one uses Cartesian co-ordinates. At each timestep we find the average three-dimensional velocity dispersion of the 10 realisations for each

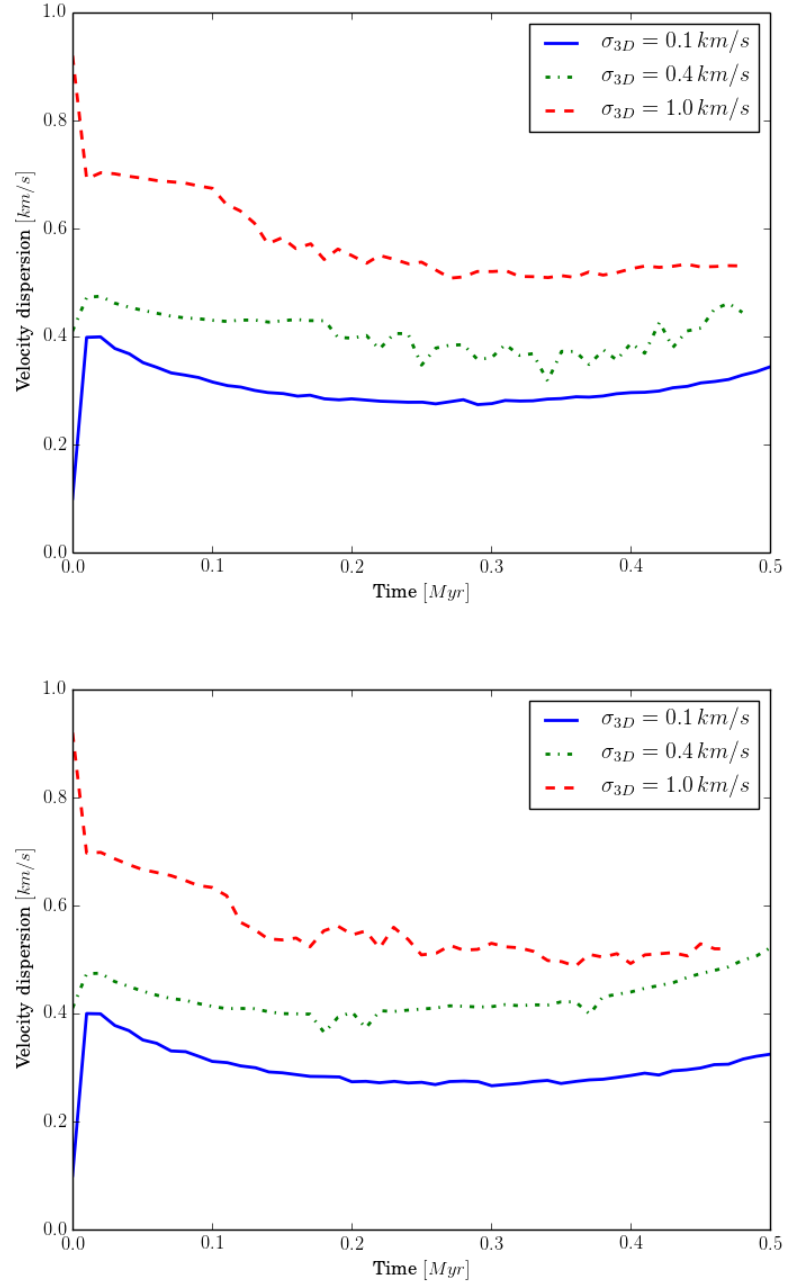


Figure 5.4. Average velocity dispersion as a function of time for the subsonic (solid blue), transonic (dot-dashed green) and supersonic (dashed red) for (top) natural mix turbulence simulations and (bottom) purely compressive turbulence simulations. In all 6 cases the velocity dispersion tends to stabilise at a roughly transonic level, $\sim 0.4 \pm 0.15 \text{ km/s}$.

parameter pair. The resulting velocity dispersions for the natural mix turbulence simulations are shown in Figure 5.4. One sees that, no matter what the initial turbulent velocity dispersion is, the three-dimensional velocity dispersion within the filament tends to approximately the same transonic value, $\sim 0.4 \pm 0.15$ km/s. The velocity dispersion rises after 0.5 Myrs as the filament begins to fragment.

Taking a value of 0.4 km/s for σ_{3D} , the effective sound speed in these filaments is $a_{\text{EFF}} \sim 0.45$ km/s. Radial collapse begins at $\tau_{\text{CRIT}} \sim 0.5$ Myr. Thus the most unstable mode given by equation 5.6 is ~ 0.45 pc, consistent with the large scale (but not dominant) peak in the core separation distributions for the initially subsonic filaments. The small scale (and dominant) peak at ~ 0.1 pc is consistent with the effective Jeans length given by $a_{\text{EFF}}/\sqrt{G\rho}$, where ρ is the average density in the filament and G is the gravitational constant. The average density in these filaments is of the order $10^{-19} - 10^{-18}$ g/cm $^{-3}$, which results in a Jeans length of 0.05 – 0.17 pc.

If the large scale separation is regulated by a variant of the dispersion relation found previously, it may be used to determine the age and mean accretion rate of a filament. One needs to substitute the effective sound speed for the isothermal sound speed in equations 5.2 and 5.3 resulting in,

$$\tau_{\text{AGE}} \geq \tau_{\text{CRIT}} \simeq \frac{\lambda_{\text{CORE}}}{2a_{\text{EFF}}}, \quad (5.7)$$

and

$$\langle \dot{\mu} \rangle \simeq \frac{2a_{\text{EFF}}\mu}{\lambda_{\text{CORE}}}, \quad (5.8)$$

Filaments assembled from gas with subsonic turbulence therefore possess two preferential fragmentation length scales: a large fragmentation length scale which is consistent with a modified version of the filamentary fragmentation model presented in chapter 4 (equation 5.6); and a small fragmentation length scale which is consistent with the effective Jeans length in these filaments.

It is important to note how these fragmentation length scales evolve. Figure 5.5 shows the number of large scale core separations (> 0.3 pc) divided by the number of small scale core separations (< 0.3 pc) as a function of time since the first sink particle forms. Large scale fragmentation proceeds first but is quickly followed by small scale fragmentation such that 0.1 Myrs after fragmentation begins, there are roughly twice as many small length scale core separations as large length scale core separations. The rapid increase in small scale Jeans length separations after collapse begins reduces the periodicity of the fragmentation. The fact that the phase of a filament's life when it is dominated by periodic fragmentation is short-lived may explain why quasi-periodically fragmented filaments are rare, despite both equilibrium

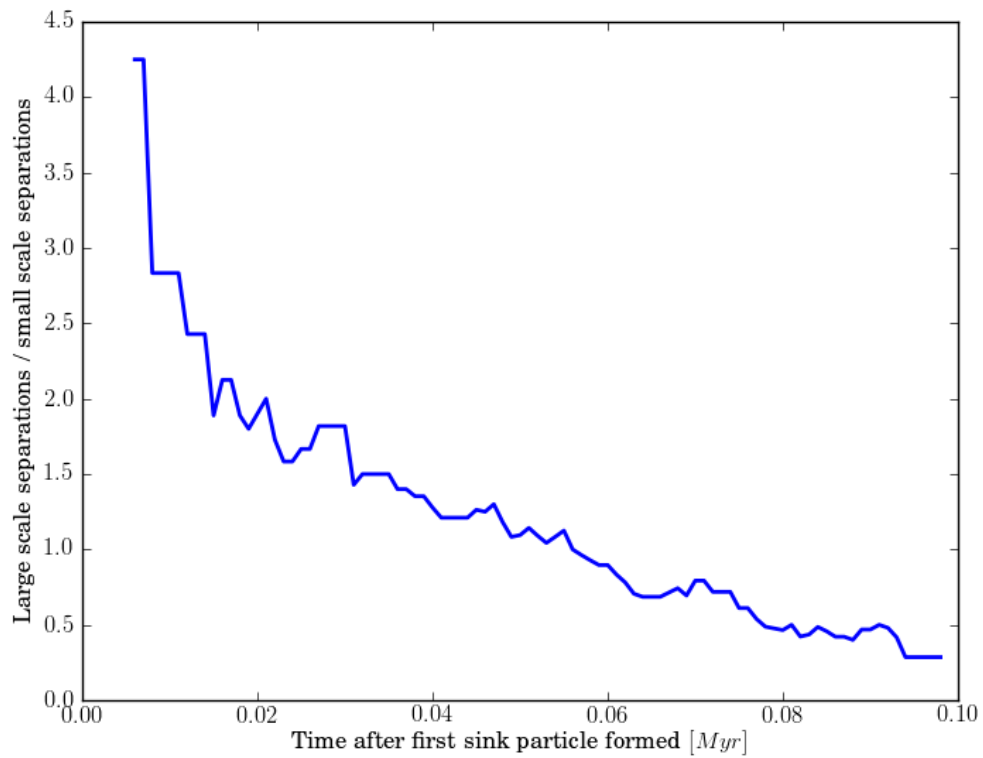


Figure 5.5. Ratio of the number of large scale core separations (> 0.3 pc) over the number of small scale core separations (< 0.3 pc) as a function of time for subsonic natural mix turbulence simulations. Large scale separations dominate at early times, but small scale separations become more common very quickly, on the order of a tenth of a megayear.

and non-equilibrium models suggesting they ought to be standard.

Thus, initially subsonic filaments fragment in a two-tier hierarchical fashion, where large scale fragmentation occurs first on a length scale determined by filamentary fragmentation and then those structures proceed to fragment on a smaller scale determined by the effective Jeans length. This type of hierarchical multi-tiered fragmentation has recently been observed in the Orion Integral Shaped Filament (Teixeira et al., 2016; Kainulainen et al., 2016b).

5.4.2 INITIALLY TRANSONIC TURBULENCE

When the turbulence in the accretion flow is subsonic, the separation of fragments is largely determined by gravitational fragmentation – as described in the preceding subsection. However, once the turbulence in the accretion flow is transonic, the separation of fragments is largely determined by the dominant wavelengths in the turbulence. Specifically, since most of the turbulent energy is in the longer wavelength modes, there is a clustering of separations in the range 1.0 pc to 1.5 pc, corresponding to the modes with $k_z = 2$ to 3 (recall that the box is 3 pc long). This trend is independent of whether the turbulence comprises purely compressive modes, or a natural mix of compressive and solenoidal modes.

As the fragmentation is dominated by the turbulent field, the exact position of the peak in core separations is likely to be the consequence of our choice of λ_{MAX} , the maximum wavelength in the turbulent field, and is a numerical effect. If λ_{MAX} were reduced the position of the peak would likely move to a lower value. This effect has been studied in detail for the case of a turbulent pre-stellar core by Walch et al. (2012).

As well as the ‘turbulent’ peak at ~ 1.2 pc, the purely compressive turbulence simulations also show a peak at ~ 0.5 pc, which is consistent with gravitational filamentary fragmentation (equation 5.6); this peak is not apparent in the natural-mix turbulence. This suggests that the case of purely compressive turbulence is better described by the gravitational fragmentation model (modified by combining the thermal and turbulent contributions to the velocity dispersion) than the case of natural-mix turbulence, which contains solenoidal modes. The purely compressive case is thus more likely to produce quasi-periodically fragmented filaments.

5.4.3 INITIALLY SUPERSONIC TURBULENCE

The initially supersonic cases also show a marked difference due to the nature of the turbulence. Both show the clustering of core separations around ~ 1.5 pc

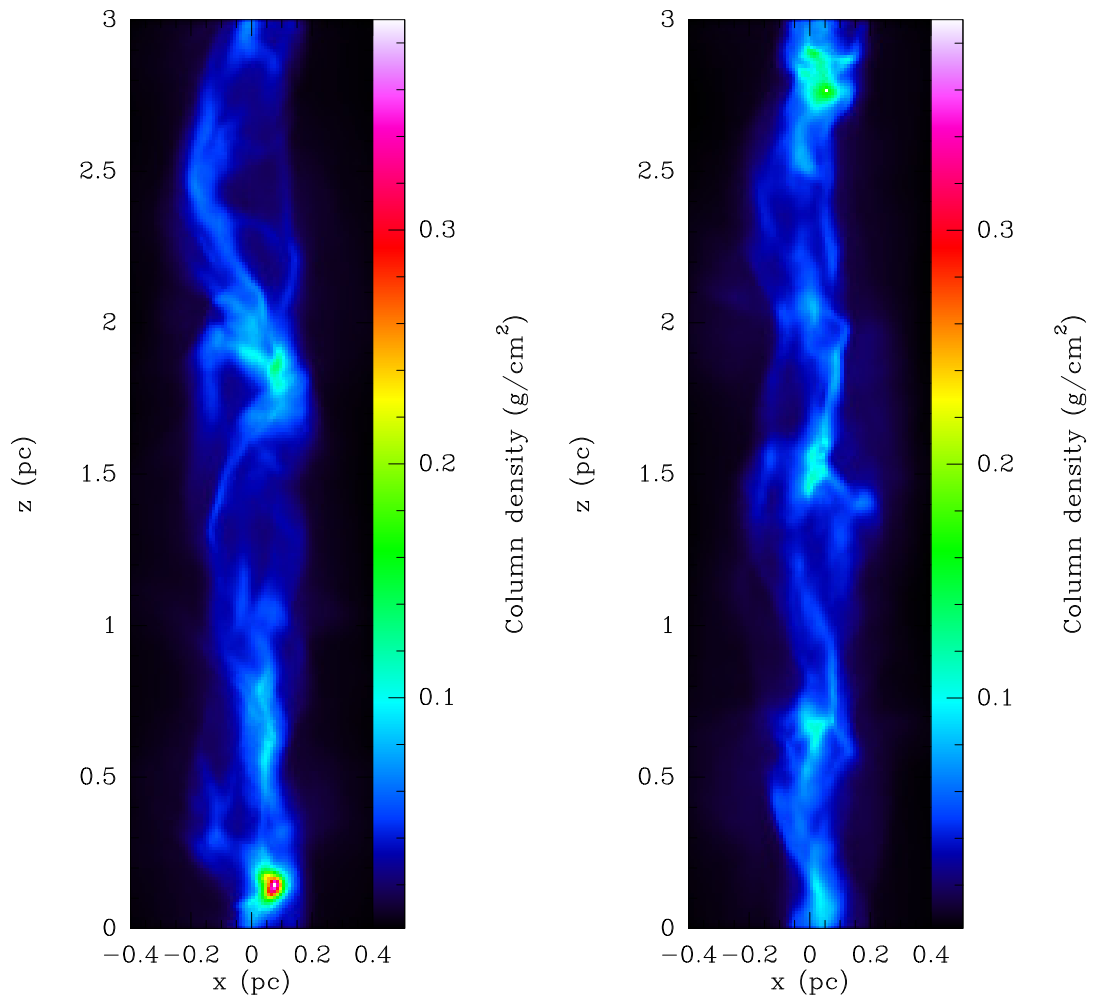


Figure 5.6. Column density maps at $t = 0.5$ Myr for two of the filaments with initially supersonic turbulence, $\sigma_{3D} = 1$ km/s but different types of turbulence. On the left, (a), is the natural mix case, $\delta_{sol} = 2/3$, which shows numerous elongated sub-structures. On the right, (b), is the purely compressive turbulence, $\delta_{sol} = 0$, which is more ‘clumpy’ but still shows elongated sub-structure.

due to the turbulent field dominating the fragmentation process. The compressive turbulence produces the narrower of the two distributions, as in the transonic case. There is a peak at very small separations in the purely compressive case which is not apparent in the natural-mix case. This is predominately composed of separations in the range 0.02 - 0.05 pc, i.e. just above the cut-off imposed to remove multiples. It is therefore likely that this peak is due to a number of wide multiples which just exceed the cut-off, and I do not consider these separations further.

A natural mix of modes tends to dampen fragmentation globally, leading to a large number of filaments which only produce one core. Natural-mix turbulence delays the onset of collapse, $\bar{\tau}_{\text{COLL}} = 0.717$ Myr, more than purely compressive turbulence, $\bar{\tau}_{\text{COLL}} = 0.611$ Myr. However, the time then taken for 10% of gas to convert into sinks is 0.131 Myr for the natural mix and 0.128 Myr for the purely compressive turbulence. Solenoidal modes therefore act as a support on large scales, but are unable to slow star formation once it has started.

The increase in initial turbulence also produces a significant change in the morphology of the filaments. This can be seen in column density maps of both the natural mix and the purely compressive cases, which show a number of elongated sub-structures (figure 5.6). The elongated structures seen in the column density maps are real continuous structures in volume density and may be similar to the fibres recently seen in Taurus (Hacar et al., 2013; Tafalla & Hacar, 2015). A large number of these elongated structures are seen to overlap and merge to form hub-like features, in which most of the cores form; this is somewhat different from the fibres seen in Taurus, which appear to fragment independently of each other.

The presence of fibre-like structures may explain why the supersonic cases produce a markedly different core separation distribution from the sub- and transonic simulations, which do not form such structures. In the supersonic cases the fibre-like structures dominate the fragmentation process.

An important point to make is that the fibres identified observationally are found as velocity coherent structures in position-position-velocity (PPV) space while these elongated structures are seen in position-position (PP) space in column density, and in position-position-position (PPP) space in volume density. Without synthetic images it is impossible to make a direct comparison between the fibre-like structures seen in these simulations and the fibres observed. Nonetheless one can consider how the fibre-like structures appear in three-dimensions. Figure 5.7 shows a slice at $y = 0$ pc with the gas velocity in the y -direction, the ‘line-of-sight’ velocity, and volume density contours overlaid for one of the natural-mix initially supersonic simulations at $t = 0.5$ Myr, the time at which the filament becomes globally thermally supercritical.

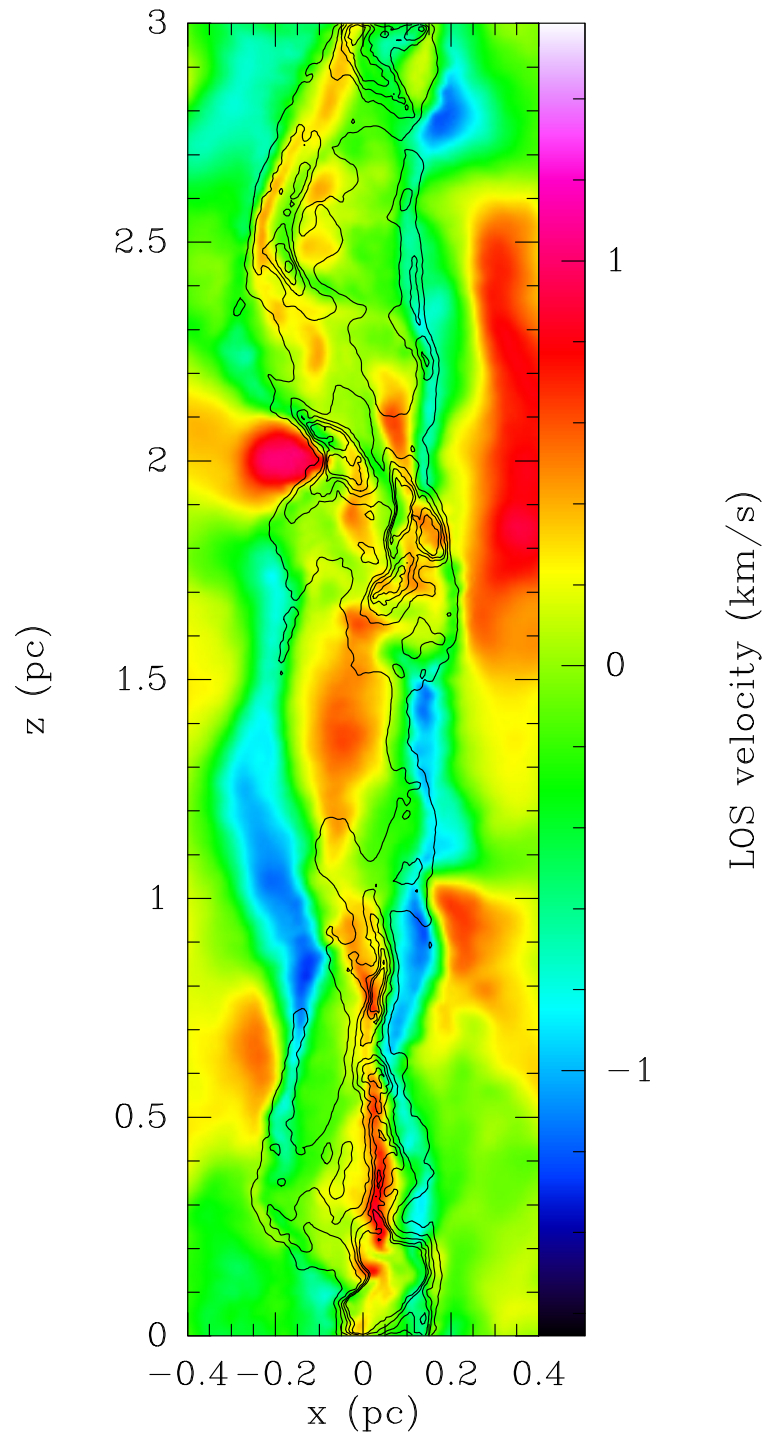


Figure 5.7. A map of the velocity component perpendicular to the plane, the ‘line-of-sight’ velocity v_y , at $y = 0$ pc with density contours overlaid for an initially supersonic natural mix turbulence simulation at $t = 0.5$ Myr. The density contours are at $2, 4, 6, 8, 10 \times 10^{-20} \text{ g/cm}^{-3}$. One can see that the dense elongated structures exhibit smooth and small variations in velocity. Those regions that show large variations are in the diffuse gas, outside the density contours, or in the high density cores which are undergoing collapse.

The density contours are at $2, 4, 6, 8, 10 \times 10^{-20} \text{ g/cm}^{-3}$. One can see that the velocity in the elongated structures varies smoothly and by small amounts. The regions which exhibit large velocity differences are either outside the contours, and so are diffuse, or associated with compact high density areas which are locally collapsing. Thus, although one cannot be certain that an observer would identify these elongated sub-structures as fibres, they are velocity coherent and continuous in volume-density.

5.4.4 DENDROGRAMS

To investigate quantitatively how hierarchical and sub-structured these filaments are, one may use dendrograms (Rosolowsky et al., 2008). Here I use the PYTHON package ASTRODENDRO*. Dendrograms are constructed from three dimensional volume density cubes with a resolution of 0.01 pc at $t = 0.5 \text{ Myr}$, the time at which the filaments become roughly thermally supercritical. The dendrograms are constructed using the parameters: $\text{min_value} = 10^{-20} \text{ g/cm}^3$, the lowest density that a data point must have to be considered when building the dendrogram; $\text{min_delta} = 5 \times 10^{-21} \text{ g/cm}^3$, the minimum density contrast between a leaf and its branch; and $\text{min_npix} = 100$, the minimum number of pixels needed for a leaf to be considered a true structure, corresponding to a sphere with a radius $\sim 0.03 \text{ pc}$. Figure 5.8 shows two example dendrograms, one from a natural mix turbulence simulation and the other from a purely compressive turbulence simulation.

One can obtain two statistics from the dendrograms which quantify the amount of sub-structure and how hierarchical that sub-structure is. The number of leaves in a dendrogram, N_{leaf} , tells one how fragmented a structure is, the more leaves the more fragments are present. The number of levels, N_{level} , from the highest leaf, that is the leaf which has the largest number of branches between it and the trunk of the dendrogram, tells one how hierarchical the structure is; the more levels, the more nested the sub-structure is. A natural mix of turbulent modes produces both a more fragmented and a more hierarchical structure than the purely compressive turbulence; the mean values and their associated errors: $N_{\text{leaf}} = 31.7 \pm 1.6$ and $N_{\text{level}} = 20.9 \pm 1.5$ for the natural mix case, and $N_{\text{leaf}} = 22.5 \pm 1.8$ and $N_{\text{level}} = 14.3 \pm 1.1$ for the purely compressive case. Though the exact values of N_{leaf} and N_{level} change when I use different values for min_value , min_delta and min_npix to construct the dendrograms, the result that the natural mix turbulence is more fragmented and hierarchical does not change.

As an observer does not have access to the three-dimensional volume density

*<http://www.dendrograms.org>

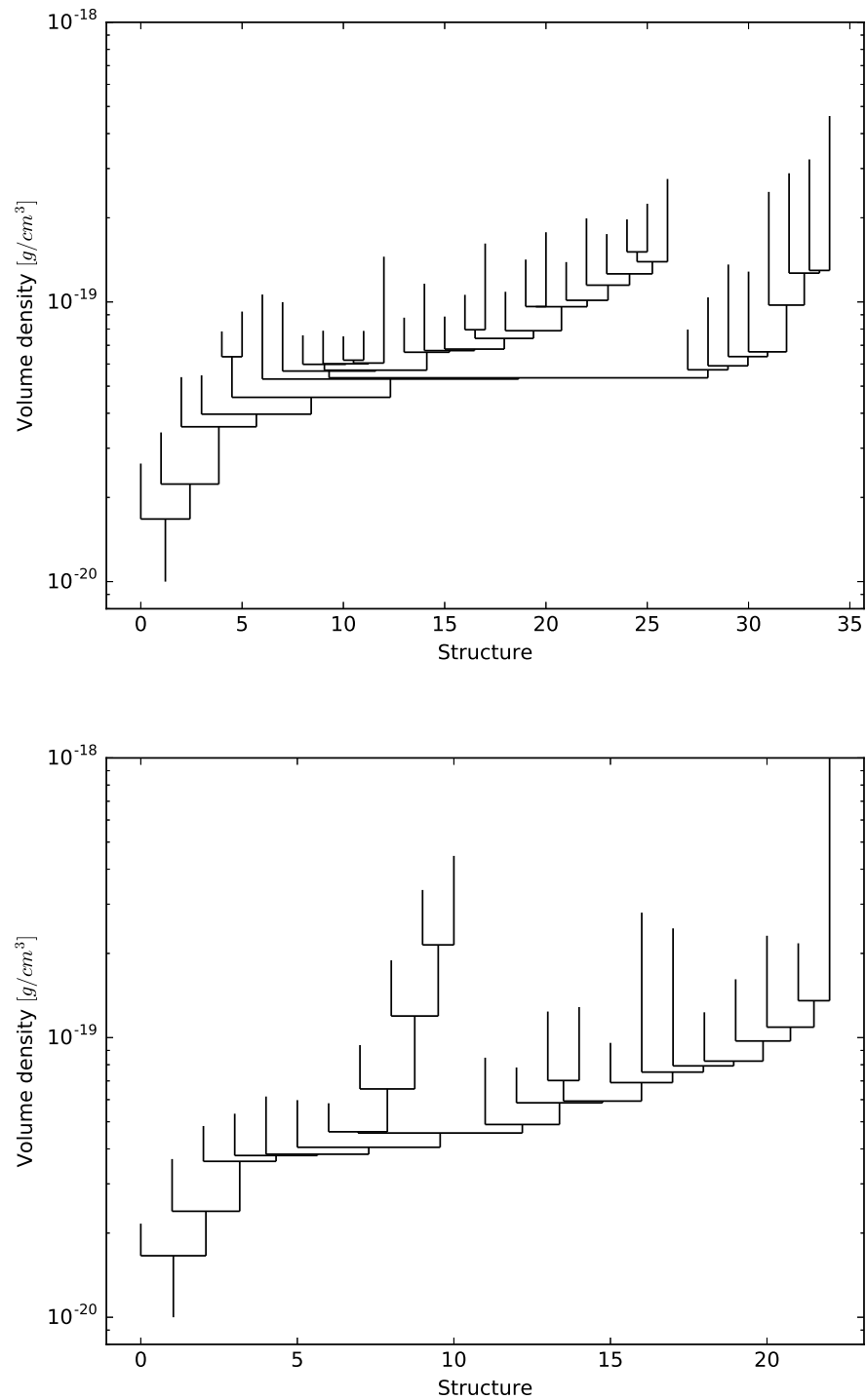


Figure 5.8. Dendrograms constructed using the three-dimensional volume density cubes of (top) a simulations with a natural mix of turbulence, and (bottom) a simulations with purely compressive turbulence. One can see that a natural mix of turbulence produces greater sub-structure, and that sub-structure is more hierarchical, than the simulations with purely compressive turbulence.

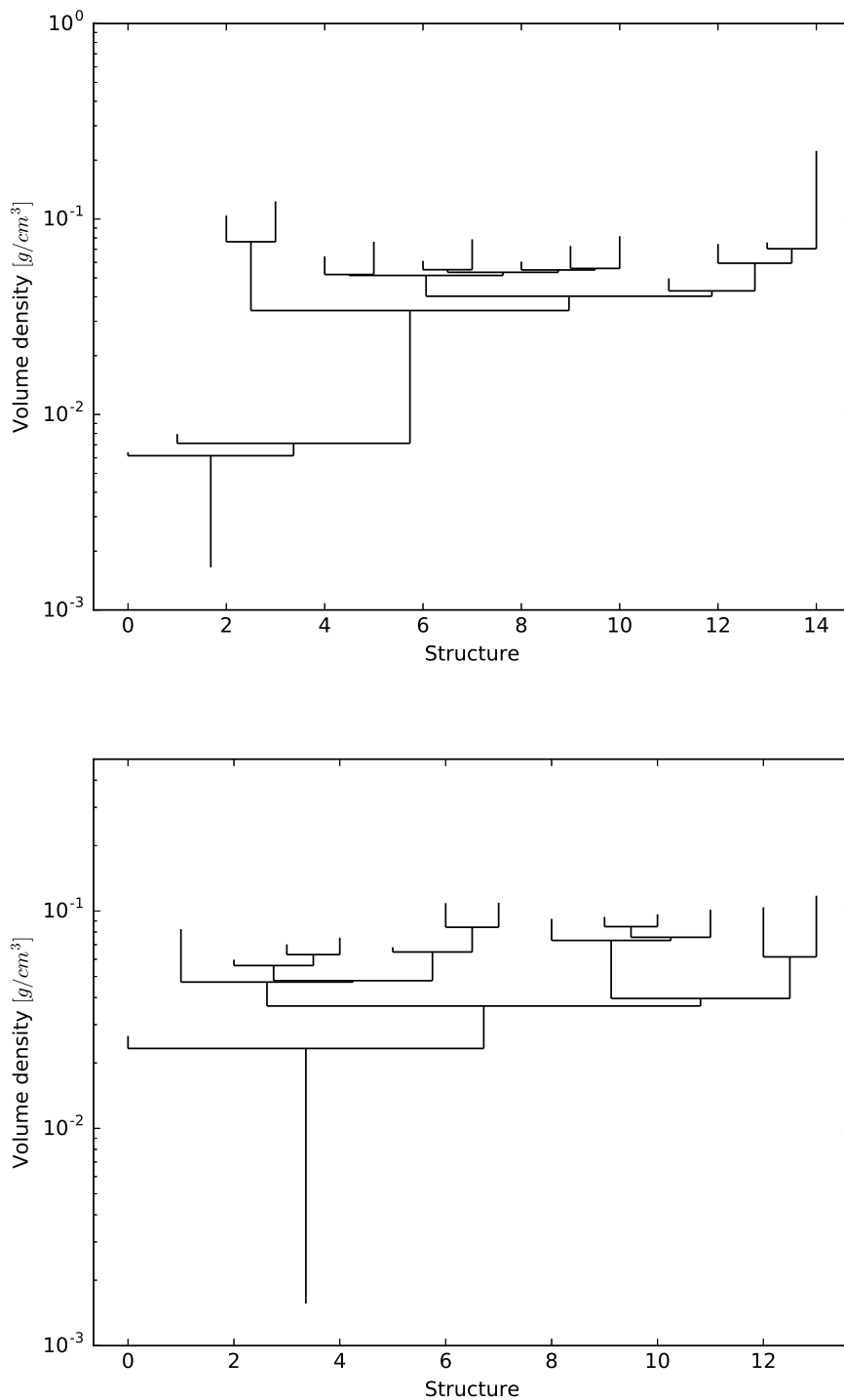


Figure 5.9. Dendrograms constructed using the two-dimensional column density maps of (top) a simulations with a natural mix of turbulence, and (bottom) a simulations with purely compressive turbulence. One can see that there is not a significant difference in either the amount of sub-structure, or hierarchical the sub-structure is.

structure of a filament, but instead must use the two-dimensional column density, I produce dendrograms using the column density of the simulations. The dendrograms are constructed using: $\text{min_value} = 3 \times 10^{-4} \text{ g/cm}^2$, $\text{min_delta} = 1.5 \times 10^{-4} \text{ g/cm}^2$ and $\text{min_npix} = 21$. These values for min_value and min_delta are chosen as they are the choices we made for the three-dimensional volume density dendrograms multiplied by 0.01 pc, the grid resolution. The choice of min_npix was made as it is $100^{2/3}$, the two-dimensional equivalent of our three-dimensional choice. The two cases, natural-mix turbulence and purely compressive turbulence, are indistinguishable from each other when one uses their column density dendrograms: $N_{\text{leaf}} = 15.8 \pm 0.7$ and $N_{\text{level}} = 9.7 \pm 0.5$ for the natural-mix turbulence, and $N_{\text{leaf}} = 14.4 \pm 0.6$ and $N_{\text{level}} = 8.9 \pm 0.6$ for the purely compressive turbulence. Figure 5.9 shows two example dendrograms built using the column density, one constructed from a natural mix turbulence simulation and the other from a purely compressive turbulence simulation. One can see that there is no significant difference between these dendrograms. This means that dendrograms derived from column density maps are unable to accurately detect differences in the three-dimensional structure, and that one ought to be cautious when using them to compare different regions. Perhaps dendrograms constructed using PPV data may show the differences in structure, and this is investigated in the next chapter.

5.4.5 THE FORMATION OF FIBRE-LIKE STRUCTURES

The formation of the fibre-like structures in situ shows that the fray and fragment scenario as proposed by Tafalla & Hacar (2015) is possible. A single main filament first forms due to the colliding flows. As mass is added to the main filament, it fragments to form elongated sub-structures, and eventually some of these fibre-like structures become unstable and fragment into cores. What is more common in these simulations is that hub networks appear and collapse occurs in the hubs, this can be seen in figure 5.10. The appearance of hub networks is a small modification to the original scenario proposed by Tafalla & Hacar (2015).

Turbulence is the main driving force by which the filaments fragment into elongated sub-structures. Only the initially supersonic turbulence simulations produce such sub-structures, thus they require a high degree of turbulence to form. Gravity cannot be the dominant mechanism for the formation of these fibre-like structures, gravitationally induced fragmentation causes collapse in the radial direction and produces the classic ‘beads on a string’ cores.

Tafalla & Hacar (2015) suggest that the fibres they observe are formed due to a combination of vorticity and self-gravity. Vorticity is defined as the curl of the

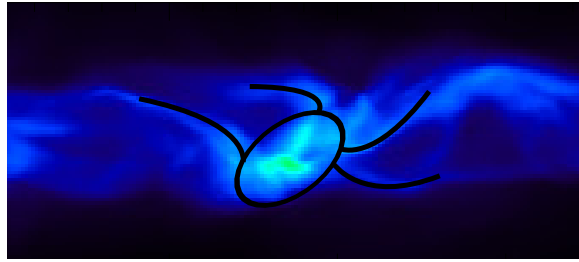


Figure 5.10. A section of the column density plot in figure 5.6 with a diagram highlighting a hub network. The circled region is the hub in which a star forms. This hub is at the intersection of numerous filamentary sub-structures. The hub network is a true structure in three dimensions and can be seen in the volume density contours in figure 5.12.

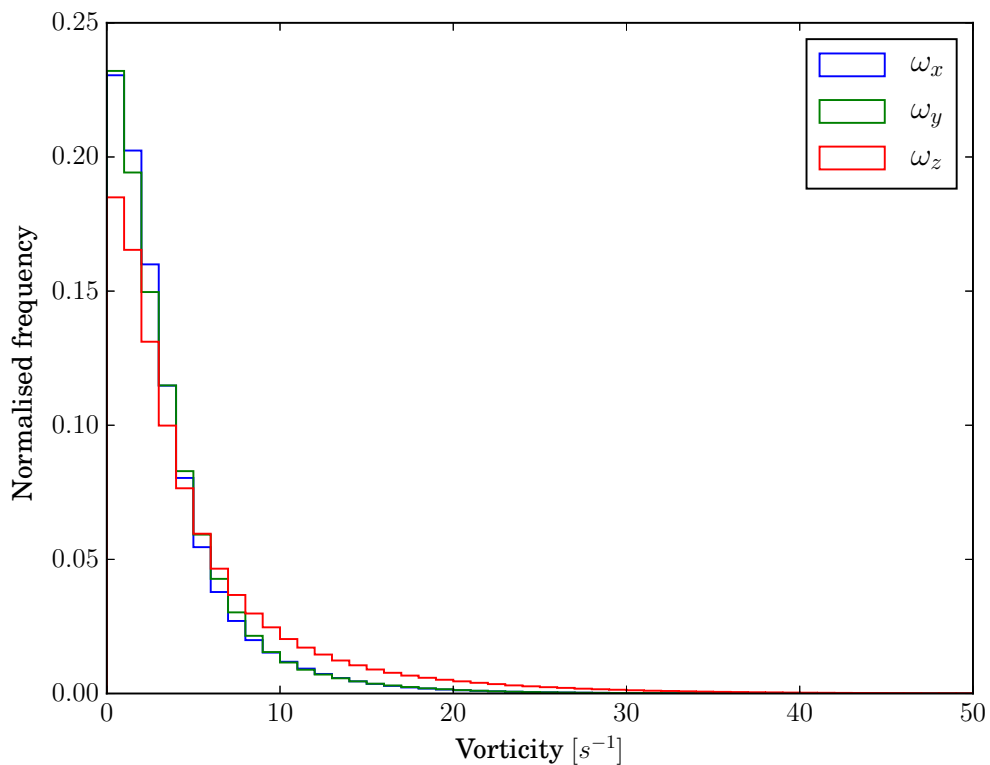


Figure 5.11. The normalised distributions of the magnitude of the three vorticity components, ω_x , ω_y and ω_z , for an initially supersonic turbulent filament at $t = 0.5$ Myr. The distribution of the vorticity parallel to the longitudinal axis of the filament, ω_z , shows a significant wing at large magnitudes.

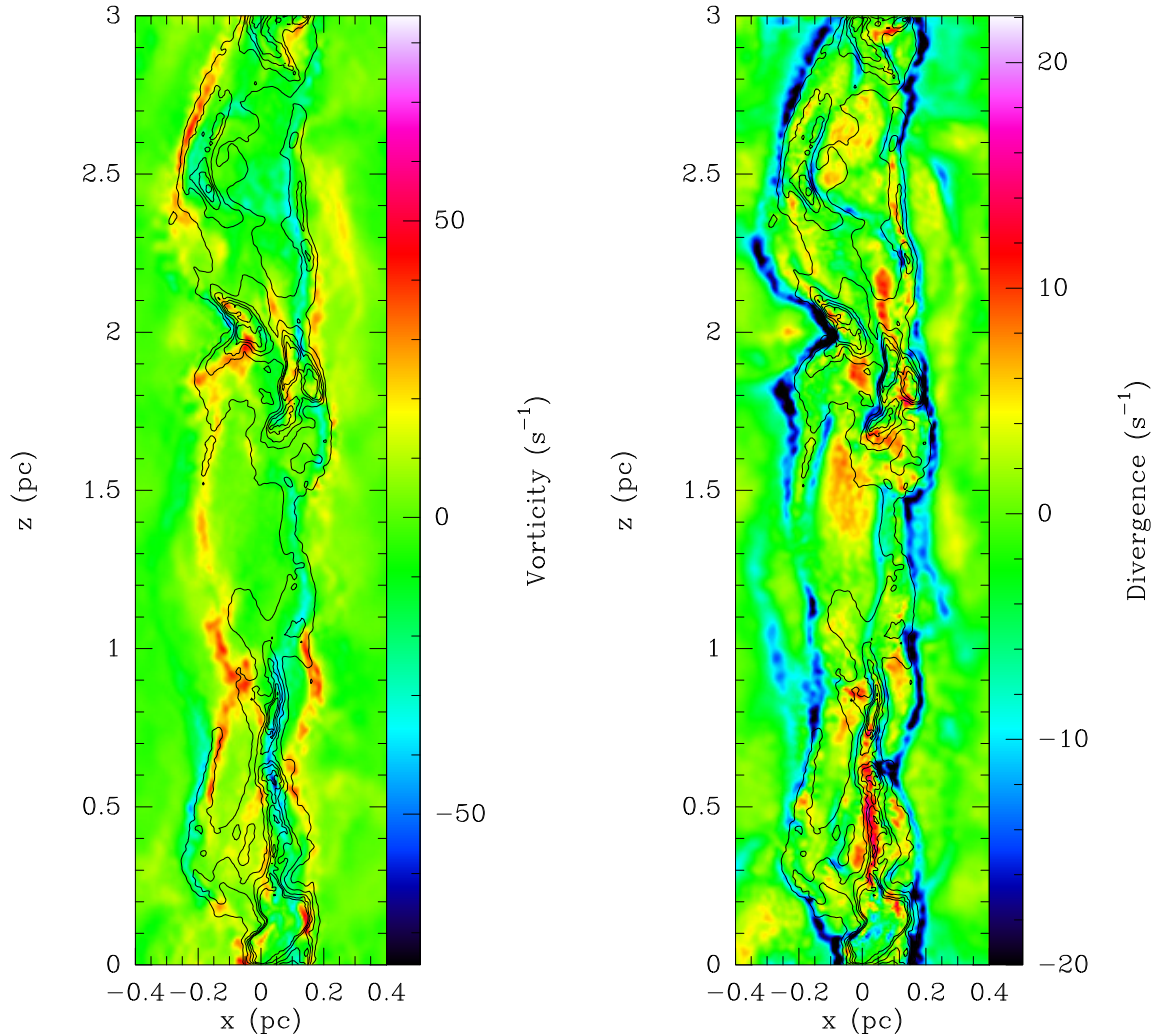


Figure 5.12. (Left) A map of the vorticity component parallel to the longitudinal axis of the filament, the z -axis, at $y = 0$ pc with density contours overlaid for an initially supersonic natural mix turbulence simulation. (Right) A map of the divergence of the velocity field in the filament, at $y = 0$ pc with the same density contours. The density contours are at $2, 4, 6, 8, 10 \times 10^{-20} \text{ g/cm}^{-3}$. One can see that the density structures follow the regions in which there exists a large vorticity gradient in the x -direction, i.e. where there are lines of blue and red/yellow next to each other. The divergence is seen to trace the accretion shock onto the main filament, but does not correlate well with the dense structures.

velocity field, $\boldsymbol{\omega} \equiv \nabla \times \mathbf{v}$, and is a measure of the local spinning motion in a fluid.

Figure 5.11 shows the normalised distributions of the magnitude of the three vorticity components, ω_x , ω_y and ω_z , for an initially supersonic turbulent filament at $t = 0.5$ Myr. One can see that ω_x and ω_y have near identical magnitude distributions. The vorticity component parallel to the longitudinal axis of the filament, ω_z , has a similar distribution to the other components but with a large tail at high magnitude. This is likely a consequence of the filamentary geometry, accretion in the radial direction will primarily produce motions in the x - y plane and appear as higher values of ω_z .

Table 5.1. Results of Spearman’s rank correlation tests

Velocity quantity	Spearman’s ρ	
	All densities	High densities
Divergence, $\nabla \cdot \mathbf{v}$	-0.16	-0.11
Vorticity, $ \omega_x $	0.31	0.28
Vorticity, $ \omega_y $	0.32	0.30
Vorticity, $ \omega_z $	0.52	0.47
Vorticity gradient, $ \delta\omega_z/\delta x $	0.61	0.58

Figure 5.12 shows a map of the vorticity parallel to the filament’s longitudinal axis, ω_z , at $y = 0$ pc, with volume density contours overlaid, for an initially supersonic turbulent filament at $t = 0.5$ Myr. The density contours are the same as those used in figure 5.7. One can see that a correlation exists between vorticity and density; more precisely the dense elongated structures form in regions in which there exists a large vorticity gradient in the radial direction, $d\omega_z/dx$. Figure 5.12 also shows a map of the divergence of the velocity field. The divergence traces the accretion shock onto the main filament but does not appear to correlate with the dense structures. There is little correlation between the other two components of vorticity, ω_x and ω_y , and density (figure 5.14). Figure 5.15 shows the mass-weighted version of figure 5.12, $\rho\nabla \cdot \mathbf{v}$ and $\rho\omega_z$. As the density spans a few orders of magnitude but the vorticity/divergence only spans a single order of magnitude these plots are dominated by the high density gas.

To quantify the correlation between the properties of the velocity field and the density, I perform Spearman rank correlation tests. This gives a non-parametric measure of the correlation between two variables which are connected by a monotonic function. The results can be seen in table 5.1. As the direction of rotation is unimportant, the magnitude of the vorticity is used. The magnitude of the vorticity gradient is also used for the same reason. As the number of points considered is very

large ($\sim 24,000$), the corresponding p -values are vanishingly small, indicating the correlations are statistically significant.

As one expects, the correlation between density and divergence is negative, i.e. dense material has a convergence flow while diffuse material has a divergent flow. However out of the five properties tested, divergence has the weakest correlation with density. Out of the three vorticity components, $|\omega_x|$, $|\omega_y|$, $|\omega_z|$, the vorticity component parallel to the filament's longitudinal axis, $|\omega_z|$, has the strongest correlation with density, as seen in figures 5.12 and 5.14. Furthermore, the vorticity gradient, defined as $|\delta\omega_z/\delta x|$, shows an even stronger correlation with density, as can be seen in figure 5.12. When the sign of the vorticity and vorticity gradient is considered, Spearman's ρ is roughly equal to zero, suggesting there is no directional preference. As can be seen in the third column of table 5.1, the same trends are apparent when one only considers high density regions, $\rho > 2 \times 10^{-20} \text{ g/cm}^3$ i.e. everything within the contours in figures 5.12 and 5.14. The values of Spearman's ρ are lower, likely due to smaller range over which the correlation is being measured.

When one considers only the magnitude of the divergence, Spearman's $\rho = 0.30$; comparable to the correlations between $|\omega_x|$ and $|\omega_y|$, and density. This suggests that the positive correlation between $|\omega_x|$, $|\omega_y|$ and $|\nabla \cdot \mathbf{v}|$, and density, is mainly due to the fact that the velocity field is more rapidly changing in higher density gas. The values of Spearman's ρ are greater for $|\omega_z|$ and $|\delta\omega_z/\delta x|$, suggesting that the same argument is not capable of explaining the correlation between these quantities and density. It is possible that due to the larger amount of energy in ω_z , as seen in figure 5.11, motions in this direction have a greater impact on structure formation. Thus the stronger correlation is due to causation.

Figure 5.13 shows density plotted against the velocity field properties in table 5.1. One can see that a correlation exists between all of these properties and density. Moreover, the relationship between $|\omega_z|$ and $|\delta\omega_z/\delta x|$, and density is both tighter and steeper than the link between the other velocity quantities and density; as expected from the results of the Spearman rank correlation tests.

Figure 5.16 is a cartoon illustrating how two nearby sites with anti-parallel vorticity vectors will result in a build-up of material and produce sub-structure. The velocity field brings gas parcels in to the centre and forms an area of higher density, gravity can then act to stabilise this structure even though it did not form the structure. However, even with gravity acting against dispersion, as the fibre-like structures are typically sub-critical, they ought to be short-lived. This could explain the prevalence of 'sterile' fibres found in Taurus (Hacar et al., 2013; Tafalla & Hacar, 2015), which are predominately sub-critical; they are mainly transitory structures created by

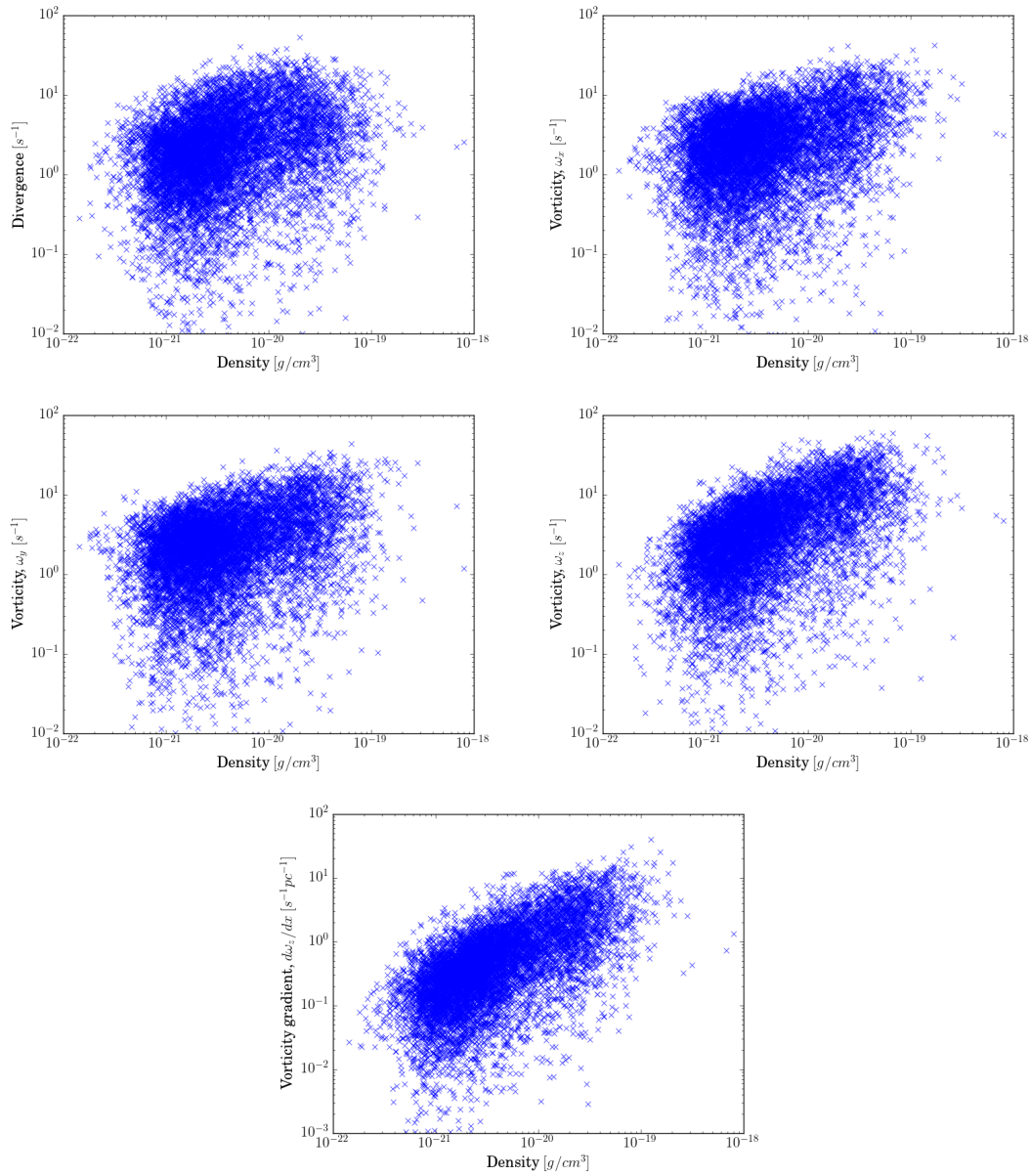


Figure 5.13. Plots showing volume density against the velocity quantities listed in table 5.1. One can see that the relationship between $|\omega_z|$ and $|\delta\omega_z/\delta x|$, and density is both tighter and steeper than the link between the other velocity quantities and density.

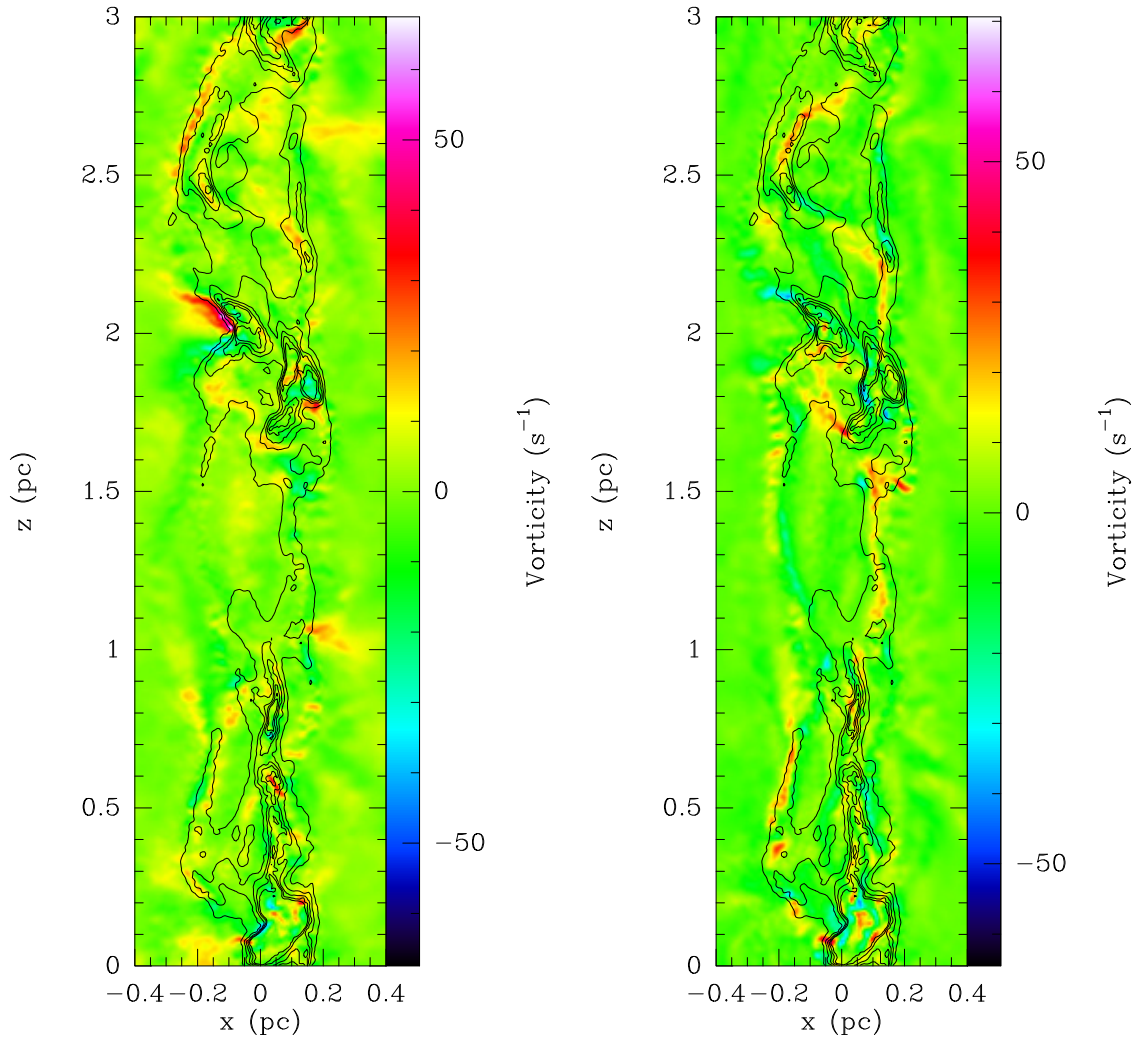


Figure 5.14. A map of the vorticity component parallel to, on the left, the x -axis and, on the right, the component parallel to the y -axis at $y = 0$ pc with density contours overlaid for an initially supersonic natural mix turbulence simulation. The density contours are at $2, 4, 6, 8, 10 \times 10^{-20} \text{ g/cm}^{-3}$. Neither plot shows a strong correlation between vorticity and the density structure.

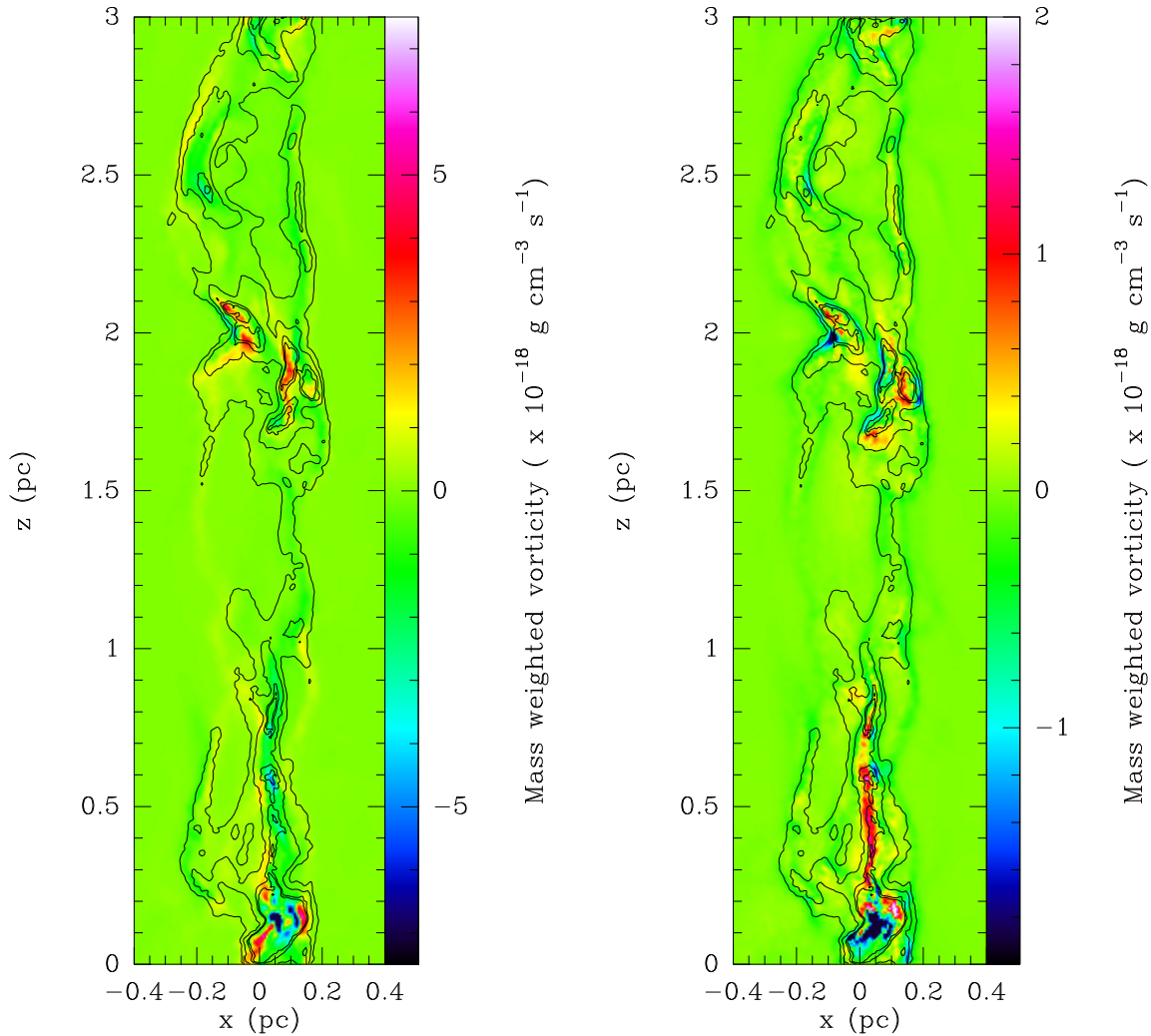


Figure 5.15. (Left) A map of the mass-weighted vorticity component parallel to the longitudinal axis of the filament, the z -axis, at $y = 0$ pc with density contours overlaid for an initially supersonic natural mix turbulence simulation. (Right) A map of the mass-weighted divergence of the velocity field in the filament, at $y = 0$ pc with the same density contours. The density contours are at $2, 4, 6, 8, 10 \times 10^{-20}$ g/cm⁻³. One can see regions with high values of mass-weighted divergence/vorticity lie within the highest density contours, this is due to the fact the density varies by a few orders of magnitude while divergence/vorticity only vary by a single order of magnitude.

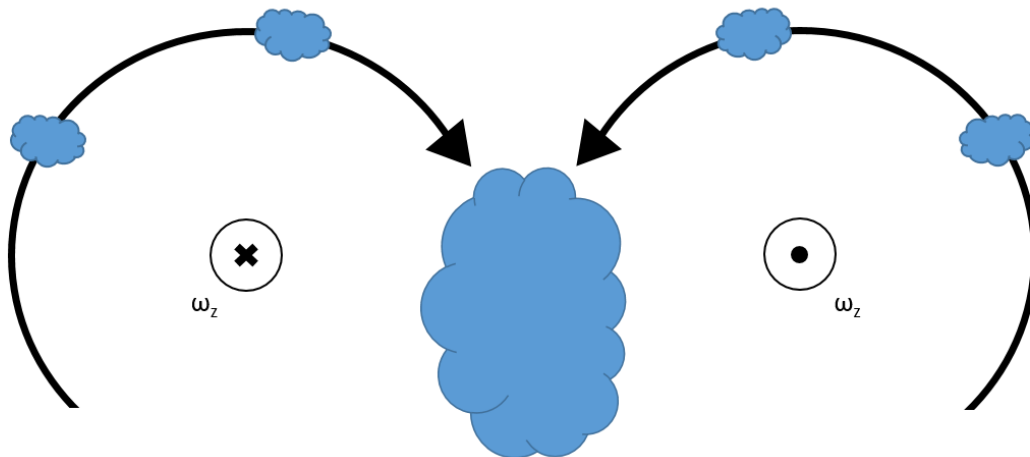


Figure 5.16. A face down view illustrating how two nearby sites with anti-parallel vorticity vectors can produce regions of higher density. The two flows are able to bring gas into the centre from both direction where it can be held together by self-gravity and form a fibre-like structure.

the filament's interior velocity field. Only the small proportion of fibres that acquire enough mass to become super-critical before they disperse are 'fertile' and fragment to form cores. One would then expect an increase in the number of 'fertile' fibres in a more massive and higher density filament, because the velocity field could produce more super-critical fibres before they disperse.

To test that the turbulent velocity field is the dominant cause of the filament fragmenting into fibre-like structures, one can re-run a simulation with no self-gravity. Figure 5.17 shows the column density plots of two simulations with the same initial conditions, but one with gravity and the other without. One can see that both simulations show the same general morphology and presence of elongated sub-structure. Gravity has therefore not played a dominant role in forming the fibre-like structures, but does act to hold them together, as seen in figure 5.17a where the fibre-like structures are narrower and denser than in the simulation without gravity.

As the filament's internal turbulence tends to a roughly transonic level no matter what the initial level of turbulence is (as seen in figure 5.4 and discussed in more detail in §5.4.6), the turbulence in the accretion flow must play a role in producing the differences in morphology between simulations with different initial levels of turbulence. Supersonic turbulence in the diffuse accretion flow produces density enhancements which flow onto the main filament. The impact of these irregular shaped clumps causes oblique shocks within the filament, producing vorticity, evidenced by

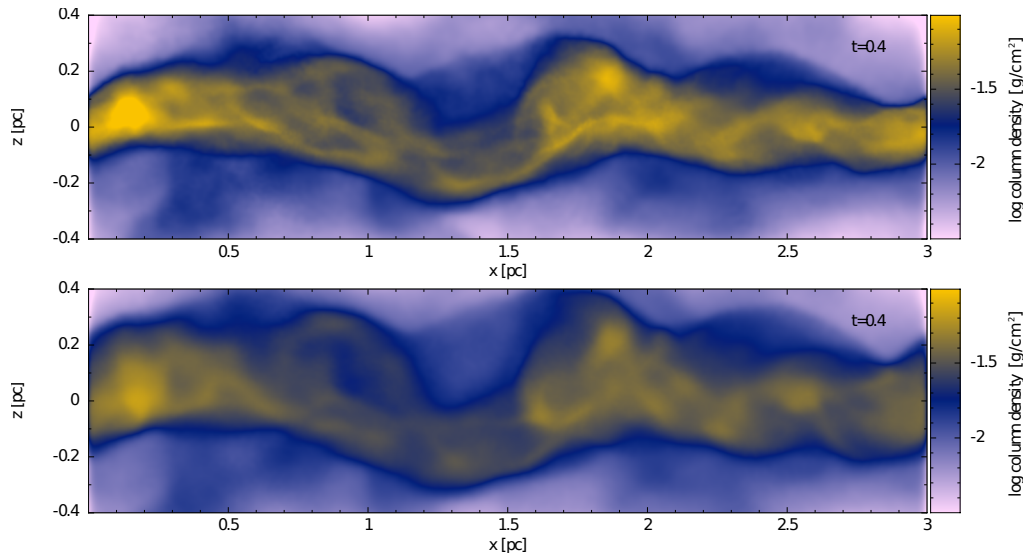


Figure 5.17. Column density plots of two natural-mix, initially supersonic turbulence simulations which have the same initial conditions, (top) shows the simulation with self-gravity, (bottom) shows the simulation without self-gravity. One can see that both simulations show the same elongated sub-structure, but the sub-structures are more well defined when self-gravity is included. Thus the velocity field is the dominant mechanism for the formation of these fibre-like structures, gravity acts against dispersal but is not necessary for their formation.

the high vorticity one can see at boundary of the filament where the accretion shock is located (see figure 5.12). Thus the formation of fibre-like structures may be intrinsically linked to a filament's accretion from a turbulent inhomogeneous medium.

5.4.6 ACCRETION DRIVEN TURBULENCE

The convergence of the velocity dispersion in all cases to a roughly transonic level is interesting as observers have seen a number of such filaments (Arzoumanian et al., 2013; Hacar et al., 2013; Fernández-López et al., 2014; Kainulainen et al., 2016a). There must exist a continuous mechanism which produces and sustains turbulence in the filaments. Heitsch (2013) proposes that accretion flows onto a filament can drive turbulence. He concludes that the velocity dispersion driven by accretion is given by,

$$\sigma(t) = \left(2\epsilon R_f v^2(R_f) \frac{\dot{m}(t)}{m(t)} \right)^{1/3}, \quad (5.9)$$

where ϵ is a driving efficiency factor in the range 0.01 - 0.1, R_f is the filament's bounding radius, $v(R_f)$ is the velocity of the accreting gas at the filament's bounding radius, $m(t)$ is the filament's line-density at time t and $\dot{m}(t)$ is the accretion rate at time t . One can use the information from the simulations to find the values of these

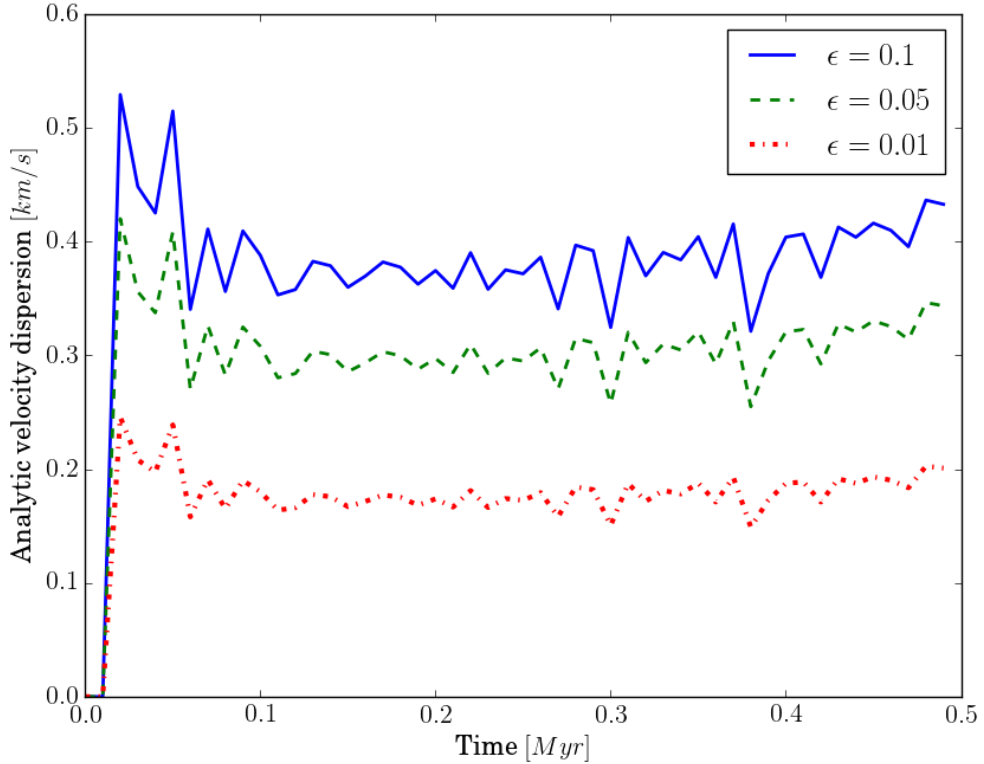


Figure 5.18. Analytically estimated velocity dispersion due to driving by accretion for the subsonic natural mix turbulence simulations (equation 5.9). A driving efficiency between 5% and 10% is necessary to produce a velocity dispersion ~ 0.4 km/s as seen in the simulations.

parameters at every snapshot time and so produce a time evolution of the expected velocity dispersion due to driving. Figure 5.18 shows the average expected velocity dispersion due to driving by accretion for $\epsilon = 0.01, 0.05, 0.1$ using the 10 simulations with parameters $\delta_{\text{sol}} = 2/3$ and $\sigma_{3\text{D}} = 0.1$ km/s. An efficiency factor in the range of 5 – 10% is able to drive a velocity dispersion of ~ 0.4 km/s; this is true for all 6 pairs of parameters.

Seifried & Walch (2015) see a similar result in their simulations, the accretion is only able to drive a velocity dispersion of at most 0.5 km/s. The simulations presented in this chapter use a relatively high initial accretion rate onto the filament, $\dot{\mu} = 70 M_{\odot} \text{pc}^{-1} \text{Myr}^{-1}$, which increases with time due to gravitational acceleration such that by the time of collapse $\dot{\mu} \sim 120 M_{\odot} \text{pc}^{-1} \text{Myr}^{-1}$. Observations have shown that accretion rates on to filaments lie in the range $10 - 150 M_{\odot} \text{pc}^{-1} \text{Myr}^{-1}$ (Palmeirim et al., 2013; Kirk et al., 2013), thus one cannot realistically invoke higher

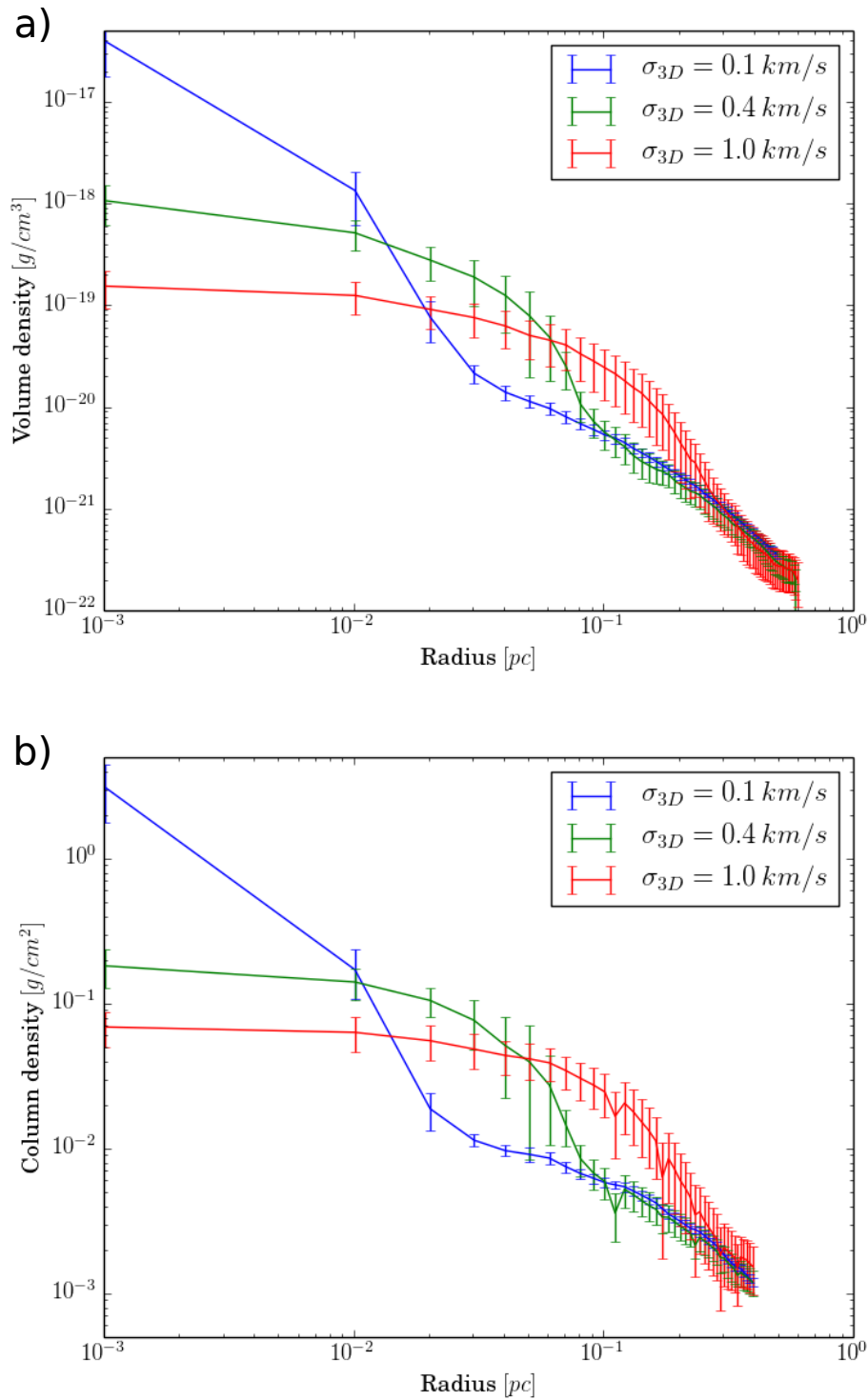


Figure 5.19. (a) The azimuthally and longitudinally averaged radial volume density profiles for the three natural mix turbulent cases, initially sub-, tran- and supersonic velocity dispersions, at the end of the simulations when the filaments have line-densities $\sim 1.3 \mu_{\text{CRIT}}$. (b) The longitudinally averaged radial column density profiles for the same simulations. The error bars show the inter-quartile range around the median.

accretion rates to produce additional turbulence to stabilise nearby supercritical filaments against radial collapse.

However, while the initially sub- and transonic filaments do radially collapse and produce narrow filaments, the initially supersonic filaments are thermally supercritical at the end of the simulations but still show a large radial extent. Figure 5.19a shows the azimuthally and longitudinally averaged radial volume density profiles for the three natural mix turbulent cases with initially sub-, tran- and supersonic velocity dispersions, at the end of the simulations when the filaments have line-densities $\sim 1.3 \mu_{\text{CRIT}}$. The median was used to average the profile so as to avoid undue influence of outliers, namely the very high density cores. One can see that the initially supersonic case shows the broadest radial profile. The full width half maxima (FWHMs) of these profiles are, < 0.02 , < 0.02 , and 0.08 pc for the sub-, tran- and supersonic cases respectively. The sub- and transonic cases have upper limits as the resolution of the grid used to produce these plot is 0.01 pc. The same result is seen in column density (figure 5.19b). The FWHMs of the column density profiles are, < 0.02 , 0.02 , and 0.12 pc for the sub-, tran- and supersonic cases respectively.

The fact that filaments growing from gas with supersonic turbulence do not collapse radially when their line-density exceeds the critical value can not be attributed to their internal velocity dispersion, all three cases end up with roughly the same level of internal turbulence. The main difference between the three cases is the resulting morphology; it is possible that the considerable level of sub-structure in the supersonic cases helps to moderate the global radial instability. Possibly the break up of a filament into fibre-like structures invalidates the assumptions underlying the derivation of the critical line-density in Ostriker (1964); this needs to be investigated further, as it presents a possible solution to the problem that supercritical filaments should collapse radially to widths narrower than the observed 0.1 pc (Arzoumanian et al., 2011; André et al., 2016).

5.5 CONCLUSIONS

The process by which a filament fragments into cores is complicated by the presence of turbulence and inhomogeneous accretion. Moreover, the amount of turbulence and inhomogeneity produces significant differences in filament morphology and fragmentation.

Those filaments which are formed in a roughly sub-sonic turbulent and mildly inhomogeneous medium show hierarchical two-tiered fragmentation, similar to the fragmentation seen in Orion (Teixeira et al., 2016; Kainulainen et al., 2016b). The

first fragments are large scale structures with wide separations, this fragmentation process is due to the gravitational fragmentation of the filament and is described by a modified dispersion relation derived in the previous chapter (equation 5.6). Next, these fragments undergo further fragmentation producing small scale separations, this fragmentation process occurs on the Jeans length. This change in fragmentation behaviour on different length scales has been seen in G11 by Kainulainen et al. (2013). Moreover, the fragmentation due to Jeans' instability occurs on a very short timescale, ~ 0.1 Myr, and removes obvious signs of periodicity in the separation of fragments along a filament, possibly explaining why observed quasi-periodically fragmenting filaments are rare.

As the level of turbulence increases, gravity dominated filament fragmentation lessens in importance and the fragmentation length scales are mainly determined by the density perturbations delivered by the turbulence. As well as changing fragmentation length scales, increased turbulence causes elongated fibre-like structures to form within the main filament, which is very like the fray and fragment scenario of fibre production in situ proposed by Tafalla & Hacar (2015). We see that these structures are intimately linked to the velocity field in the filament. Where there exists a large gradient in vorticity, the velocity field is able to gather gas together and form dense structures. I propose that this vorticity is generated by the accretion of dense irregular shaped clumps formed by supersonic turbulence in the diffuse accretion flow. The impact of such clumps causes oblique shocks inside the filament and so generates vorticity, which is seen by the high levels of vorticity at the edges of fibres, close to the accretion shock layer.

One could expect that, as fibres accrete from the gas within the filament, which is less turbulent than the gas in the accretion flow, they may fragment in a manner similar to the filaments in the initially sub-sonic simulations. Fibres could therefore be expected to fragment in a quasi-periodic manner. However, the simulations presented here do not contain enough mass for this to occur.

Although the initial level of turbulence in these simulations differs by a factor of 10, the internal filament velocity dispersion always tends towards the sonic level and remains stable until collapse begins. I show that accretion driving is able to sustain this level of turbulence if one takes an efficiency factor of 5 – 10%. The fact that there is a considerable difference in filament morphology and fragmentation with different initial velocity dispersions even though the internal filament velocity dispersion tends to the same value, suggests that the inhomogeneity of the accretion flow is the dominant factor governing a filament's evolution. Moreover, one sees that despite the same level of internal velocity dispersion the filaments in the initially

supersonic simulations do not collapse radially when their line-density exceeds the critical value, unlike the initially sub- and transonic cases which do collapse radially. It is possible that the considerable level of sub-structure present means that these filaments may collapse locally once they become super-critical but not necessarily globally.

Seed	Natural mix				Purely compressive			
	t_{sink}	$t_{10\%}$	Δt	N_{sink}	t_{sink}	$t_{10\%}$	Δt	N_{sink}
1	0.627	0.697	0.070	11	0.594	0.676	0.082	8
2	0.617	0.691	0.074	17	0.599	0.651	0.052	10
3	0.564	0.632	0.068	10	0.579	0.650	0.071	10
4	0.624	0.690	0.066	12	0.589	0.651	0.062	10
5	0.620	0.681	0.061	11	0.590	0.658	0.068	9
6	0.630	0.675	0.045	8	0.587	0.655	0.068	11
7	0.621	0.693	0.072	13	0.620	0.661	0.041	14
8	0.615	0.695	0.080	14	0.603	0.664	0.061	14
9	0.651	0.697	0.046	11	0.603	0.659	0.056	14
10	0.607	0.674	0.067	10	0.608	0.658	0.050	12
Mean	0.618	0.683	0.065	11.7	0.597	0.658	0.061	11.2
σ	0.021	0.019	0.011	2.4	0.011	0.007	0.011	2.1

Table 5.2. A table showing the time at which the first sink formed, t_{sink} , the time the simulation ended when 10% of the mass is in the form of sinks, $t_{10\%}$, the difference between these times, Δt , and the number of sinks formed by the end of the simulation, N_{sink} , for each simulation with an initial sub-sonic velocity dispersion of $\sigma_{3D} = 0.1$ km/s. Also shown is the mean and standard deviation of these statistics.

Seed	Natural mix				Purely compressive			
	t_{sink}	$t_{10\%}$	Δt	N_{sink}	t_{sink}	$t_{10\%}$	Δt	N_{sink}
1	0.606	0.748	0.142	12	0.557	0.689	0.132	8
2	0.593	0.712	0.119	19	0.540	0.662	0.122	10
3	0.472	0.776	0.304	4	0.514	0.634	0.120	3
4	0.610	0.689	0.079	14	0.520	0.690	0.170	12
5	0.646	0.721	0.075	9	0.508	0.633	0.125	15
6	0.610	0.724	0.114	10	0.570	0.689	0.119	10
7	0.641	0.734	0.093	10	0.655	0.736	0.081	13
8	0.607	0.704	0.097	13	0.569	0.705	0.136	11
9	0.702	0.776	0.074	12	0.528	0.642	0.114	10
10	0.588	0.687	0.099	16	0.611	0.689	0.078	12
Mean	0.608	0.727	0.120	11.9	0.557	0.678	0.120	10.4
σ	0.055	0.030	0.065	3.9	0.044	0.032	0.025	3.1

Table 5.3. A table showing the time at which the first sink formed, t_{sink} , the time the simulation ended when 10% of the mass is in the form of sinks, $t_{10\%}$, the difference between these times, Δt , and the number of sinks formed by the end of the simulation, N_{sink} , for each simulation with an initial sonic velocity dispersion of $\sigma_{3D} = 0.4$ km/s. Also shown is the mean and standard deviation of these statistics.

Seed	Natural mix				Purely compressive			
	t_{sink}	$t_{10\%}$	Δt	N_{sink}	t_{sink}	$t_{10\%}$	Δt	N_{sink}
1	0.652	0.864	0.212	13	0.684	0.811	0.127	9
2	0.665	0.793	0.128	20	0.661	0.735	0.084	12
3	0.436	0.658	0.222	7	0.469	0.585	0.116	11
4	0.695	0.859	0.164	13	0.532	0.718	0.186	13
5	0.911	1.027	0.116	23	0.565	0.693	0.128	12
6	0.801	0.867	0.066	11	0.453	0.641	0.188	9
7	0.730	0.847	0.117	16	0.836	0.892	0.056	9
8	0.684	0.820	0.136	7	0.688	0.814	0.126	18
9	0.930	1.010	0.080	3	0.516	0.659	0.143	13
10	0.661	0.725	0.064	14	0.701	0.837	0.136	10
Mean	0.717	0.847	0.131	12.7	0.611	0.739	0.128	11.6
σ	0.134	0.107	0.052	5.8	0.116	0.093	0.039	2.6

Table 5.4. A table showing the time at which the first sink formed, t_{sink} , the time the simulation ended when 10% of the mass is in the form of sinks, $t_{10\%}$, the difference between these times, Δt , and the number of sinks formed by the end of the simulation, N_{sink} , for each simulation with an initial supersonic velocity dispersion of $\sigma_{3D} = 1.0$ km/s. Also shown is the mean and standard deviation of these statistics.

CHAPTER 6

SYNTHETIC IMAGES OF FRAGMENTING FILAMENTS

In this chapter I present results of moving-mesh hydrodynamic simulations investigating the formation of fibres. As these simulations include coupled astrochemistry and thermodynamics, I present a set of synthetic $C^{18}O$ images of the filaments. The simulations produce filaments containing numerous fibre-like structures. Moreover, I show that when viewed in PPV space the filaments show a number of elongated and velocity coherent sub-structures, well-separated in velocity space, similar to the fibres observed by Hacar & Tafalla (2011). Using dendrograms on the ‘observed’ PPV cubes I show that dendrograms are not capable of statistically discerning differences in sub-structure in PPP space. Furthermore, I show the effect of line-of-sight confusion leading to blending and artificial separation in velocity space.

6.1 INTRODUCTION

Modelling time-dependent chemistry in the ISM is important for two reasons: the chemistry is thought to evolve on timescales comparable to the dynamic evolution of the molecular cloud, meaning that the two are strongly linked due to coupled heating and cooling (Heitsch, Mac Low & Klessen, 2001; Scalo & Elmegreen, 2004; Glover et al., 2010); and possessing information about the chemical abundances of the gas in simulations allows one to produce synthetic images which are directly comparable to observations, unlike the raw simulation data themselves. As carbon containing species play an important role as the main coolants over a wide range of densities (Glover & Clark, 2012c, 2014), and are often used to observationally trace gas dynamics and properties (Hacar et al., 2013; Ragan et al., 2014; Beuther et al.,

2015; Rigby et al., 2016; Peñaloza et al., 2016), these species are the main focus of most chemical modelling work.

Modelling the astrochemistry is extremely computationally expensive. This is due to the large number of chemical species and the even larger number of possible reactions between these species (Woodall et al., 2007). Moreover, to track the abundance of each species dynamically one must solve a set of ordinary differential equations (ODEs) taking into account the rates of every creation and destruction process. These ODEs are generally stiff and so are only stable if one uses an implicit method. Using an implicit method leads to scaling relations of the order of N_{SPEC}^3 , where N_{SPEC} is the number of species in the chemical model. It is therefore entirely possible for the chemical model to be more computational expensive than modelling the hydrodynamic evolution. Due to this, many authors use reduced chemical networks which only include the key species and the dominant reactions. Glover & Clark (2012a) perform a comparison test of simplified chemical networks focused on CO production. All the models tested produce the same density and temperature PDFs and so the dynamic behaviour of the cloud is not particularly sensitive to the small-scale chemistry as long as the coupled thermodynamics is well modelled.

Filamentary structures are typically observed using C^{18}O , N_2H^+ or NH_3 (Duarte-Cabral et al., 2012; Arzoumanian et al., 2013; Hacar et al., 2013; Ragan et al., 2015; André et al., 2016, Williams et al. in prep.). One of the most interesting recent discoveries from such molecular line observations is the presence of separate velocity coherent fibres which reside within a larger main filament (Hacar & Tafalla, 2011; Tafalla & Hacar, 2015). As these structures are detected by their distinct line-of-sight velocities, it is imperative that theories attempting to explain their formation and evolution reproduce their appearance in PPV space.

In this chapter, I present numerical simulations of fibre formation due to filament fragmentation. These simulations include coupled time-dependent chemistry and thermodynamics. With the results of these simulations I produce synthetic C^{18}O observations. In section 6.2, I detail the simulation setup, the initial conditions, and describe the chemical network and heating & cooling mechanisms used; in section 6.3, I present the results of simulations, outline the production of synthetic images and present those produced from the simulations; in section 6.4, I discuss these results and compare them to previous work and observations; and in section 6.5, I summarise my conclusions.

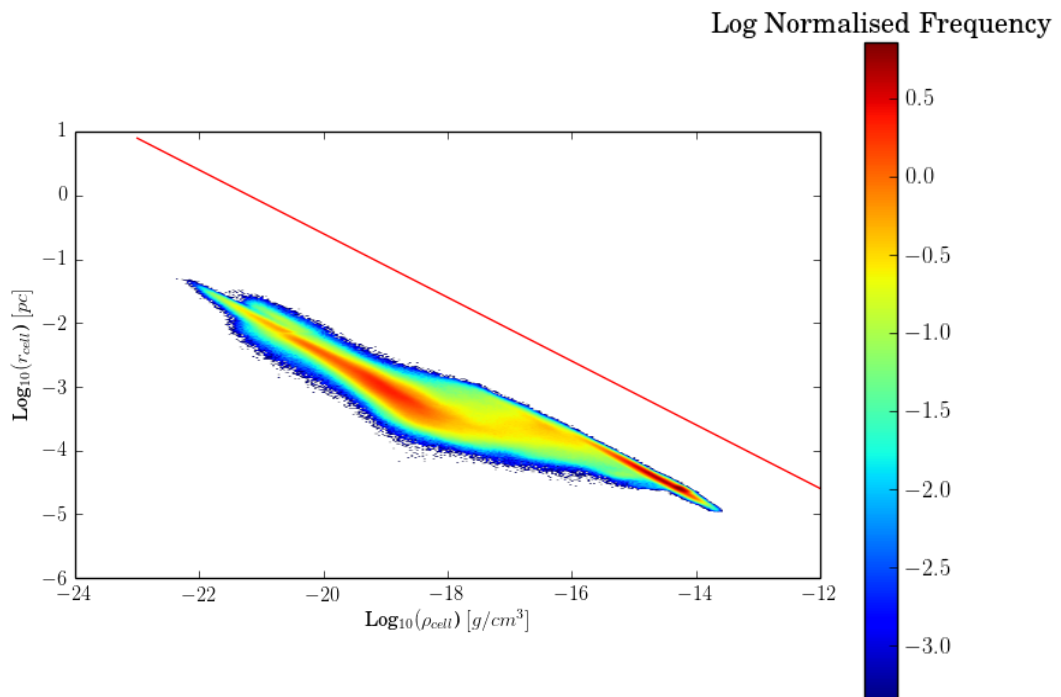


Figure 6.1. The probability density function of a cell's radius and density at the end of a simulation. The red line shows the Jeans length at 10 K for the entire density range. One can see that the Jeans length is well resolved over a wide range of densities.

6.2 NUMERICAL SETUP

The simulations presented in this chapter are performed using the moving mesh hydrodynamics code AREPO (Springel, 2011). The simulations include self-gravity, hydrodynamics and time-dependent coupled chemistry and thermodynamics.

The chemical network used in simulations is a combination of the hydrogen network introduced in Glover & Mac Low (2007a,b) and the CO network by Nelson & Langer (1997). The combined network is introduced as NL97 in Glover & Clark (2012a). The radiative heating and cooling, and cosmic ray heating rates presented in Glover & Mac Low (2007a,b) are used.

The simulations are run with solar metallicity, $Z = Z_{\odot}$, and the typical dust-to-gas ratio of 0.01. The interstellar radiation field (ISRF) is modelled as described in Draine (1978) at ultraviolet wavelengths, and in Black (1994) at longer wavelengths. The ISRF is normalised to the local ISRF, $G_O = 1.7$ in Habing (1968) units. The ISRF is attenuated using the TREECOL algorithm presented in Clark, Glover & Klessen (2012).

The gas is initially fully atomic and at 40 K; runs with initially fully molecular gas and runs at different initial temperatures show no significant differences. This agrees with the results of Glover & Clark (2012a) and Clark & Glover (2015), who find that the initial chemical state of a cloud does not alter the global evolution.

The initial density and velocity fields are the same as those described in chapter 5. The same fiducial values are used, $\rho_{\odot} = 150 M_{\odot} \text{pc}^{-3}$ and $v_{\odot} = 0.75 \text{ km/s}$, corresponding to a mass accretion rate onto the filament of $\sim 70 M_{\odot} \text{pc}^{-1} \text{Myr}^{-1}$. The filament has a length, $L = 3 \text{ pc}$, and the accretion flow a radius of $r_{\text{MAX}} = 2 \text{ pc}$, resulting in these simulations containing twice as much mass as the simulations presented in chapter 5. The turbulent field has an initial velocity dispersion of 1.0 km/s . Twenty simulations are performed, ten with a natural mix turbulent field, $\delta_{\text{SOL}} = 2/3$, and ten with a purely compressive turbulent field, $\delta_{\text{SOL}} = 0$. Simulations are terminated when a sink particle is formed.

The computational domain is periodic in all three dimensions, but does not use periodic gravity. This is done because AREPO cannot implement open boundary conditions. To ensure that domain edge effects do not affect the evolution of the filament, the computational domain is made larger than the accretion flow. The domain is $4 \times 4 \times 5 \text{ pc}$ while the accretion flow is a 3 pc long cylinder with a radius of 2 pc . At a radial velocity of $v_{\odot} = 0.75 \text{ km/s}$, gas at the edge of the cylinder, $r = 2 \text{ pc}$, would take $\sim 2.5 \text{ Myr}$ to reach the filament. As the simulations are terminated at $\sim 0.45 \text{ pc}$, the boundary does not have an effect on the filament. The rest of the

computational domain is filled with uniform density gas, $\rho = 1 \times 10^{-22} \text{ g cm}^{-3}$, ten times less dense than the outer edge of the accretion flow. This filler gas contributes $< 5\%$ of the total mass in the simulation and does not have a large effect on the filament.

The simulations are initialised using the same code to initialise the SPH simulations presented in the previous chapter. Cells are placed down like SPH particles and given the appropriate densities based on their radius. The initial conditions use ~ 1 million cells.

The resolution of the simulation is approximately given by $r_{\text{CELL}} = (3V_{\text{CELL}}/4\pi)^{1/3}$, where V_{CELL} is the volume of a cell, determined by the cell's mass and density. This is similar to SPH where higher densities lead to higher spatial resolution. One can trust features larger than a few cell radii. Additionally, like AMR codes, cell refinement is used to ensure that the resolution is sufficient to satisfy the Truelove criterion (Truelove et al., 1997). The cell is refined if $r_{\text{CELL}} > 8\lambda_J$, where λ_J is the Jeans length at that cell's density and at 10 K. As very little gas is ever below 10 K, this gives a conservative estimate of the Jeans length. Figure 6.1 shows the probability density function of a cell's radius and density at the end of one of the simulations, the red line is the Jeans length at 10 K. The majority of the gas in the filament has a density in the range $10^{-20} - 10^{-18} \text{ g/cm}^{-3}$, giving a spatial resolution in the range $\sim 3 \times 10^{-3} - 3 \times 10^{-4} \text{ pc}$.

6.3 RESULTS

The simulations produce the same fibrous morphology as those presented in the previous chapter using SPH, which indicates that their formation was not a numerical effect. Figure 6.2 shows the column density for a natural mix and a purely compressive turbulent simulation just before a sink particle forms. One can see the numerous elongated fibre-like structures in the natural mix simulation, whereas the purely compressive turbulence has created a very thin filament with signs of fibre-like structures only in the middle region.

As observational fibres are identified in position-position-velocity (PPV) space, the natural next step is to produce synthetic images so as to determine if the elongated sub-structures seen in PPP and PP space are fibres.

6.3.1 SYNTHETIC OBSERVATIONS

Synthetic observations are produced using the post-processing radiative transfer code RADMC-3D (Dullemond, 2012). Here I present synthetic observations of

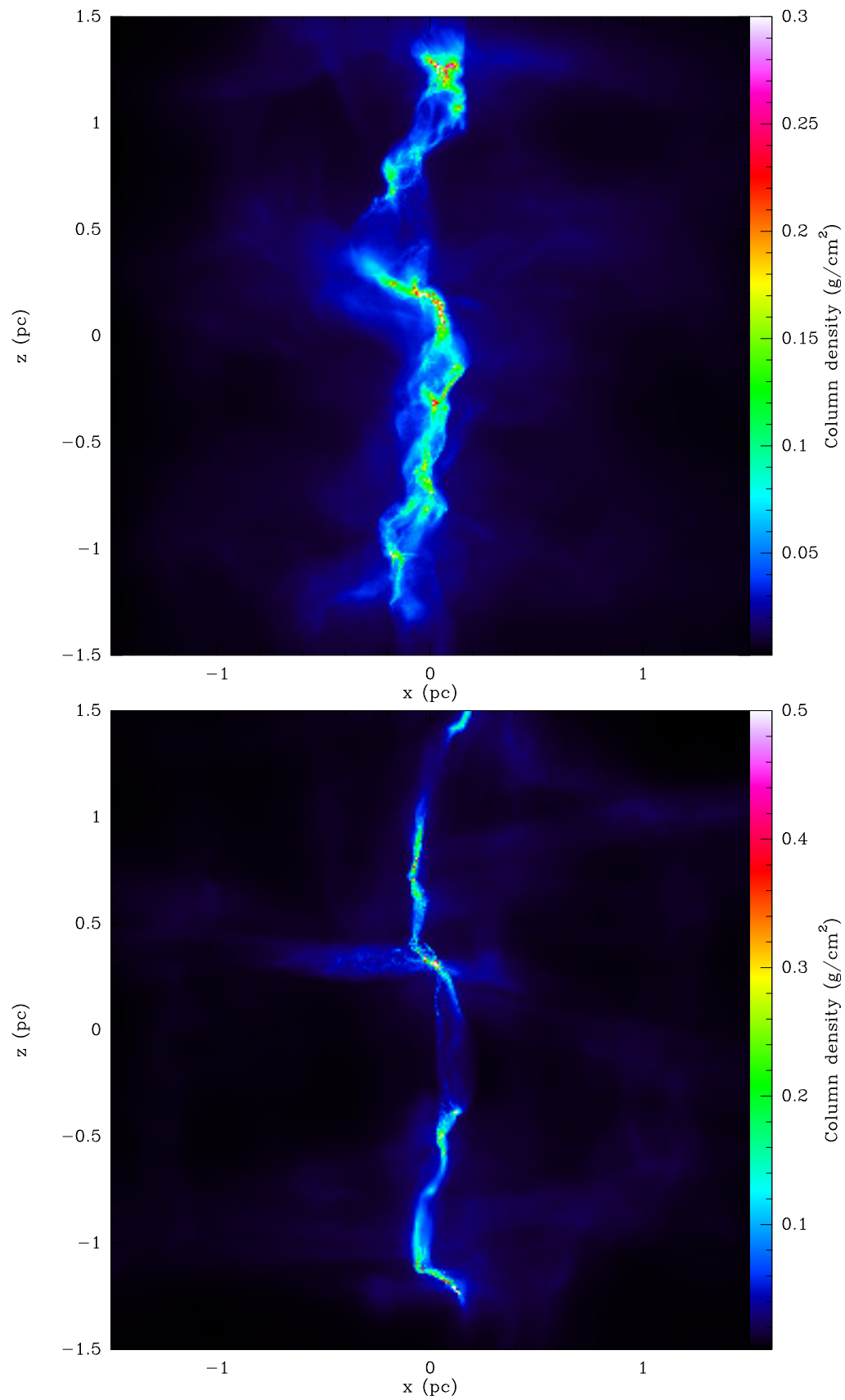


Figure 6.2. Column density map for a filament with (top) natural mix turbulence and (bottom) purely compressive turbulence. Both show sub-structure but the natural mix simulation shows numerous elongated sub-structures.

the C^{18}O rotational line $J = 1 - 0$. RADMC-3D is run assuming non-local thermodynamical equilibrium and uses the large velocity gradient approximation (Sobolev, 1957). The energy levels and excitation coefficients of C^{18}O are taken from the Leiden Atomic and Molecular Database (Schöier et al., 2005). The abundance of C^{18}O is assumed to be constant with respect to C^{16}O , the isotopologue traced in the modified NL97 chemical network, and to have a value $n_{\text{C}^{18}\text{O}} = n_{\text{C}^{16}\text{O}}/500$ (Wilson & Rood, 1994).

RADMC-3D requires a fixed/AMR grid, thus I use the in-built AREPO algorithm to map between the Voronoi mesh and a fixed grid. The grid has a resolution of 0.01 pc and covers $0.5 \text{ pc} < x, y < 3.5 \text{ pc}$ and $1 \text{ pc} < z < 4 \text{ pc}$, which includes the whole filament and the accretion flow while omitting the low density ‘filler’ gas. Micro-turbulence is usually included to estimate the unresolved velocity dispersion on scales smaller than the grid resolution. I do not include micro-turbulence as the gas inside the filament has a velocity dispersion of $\sim 0.05 \text{ km/s}$ on scales of 0.01 pc, much less than predicted from Larson’s size-linewidth relation (Larson, 1981), in agreement with recent observations showing that filaments are sub-Larson (Hacar et al., 2016). I show further on that this is also much less than the typical linewidths in the images, and so the inclusion of micro-turbulence would have very little effect on the analysis.

At high densities, CO depletion due to freeze-out on to dust grains is known to occur (Caselli et al., 1999; Redman et al., 2002; Savva et al., 2003; Christie et al., 2012; Giannetti et al., 2016). CO freeze-out is not included in the modified NL97 chemical network used. To compensate for this, I use the freeze-out approximation introduced in Hollenbach et al. (2009) which finds the instantaneous equilibrium between freeze-out and desorption. This overestimates the degree of freeze-out, it yields a depletion factor of 0.5 at a number density of $\sim 3 \times 10^4 \text{ cm}^{-3}$, whereas observations suggest that this occurs closer to 10^5 cm^{-3} (Lippok et al., 2013).

Hacar et al. (2013) achieve a velocity resolution of 0.07 km/s when using C^{18}O , $J = 1 - 0$, to map L1495 in Taurus using the 14m FCRAO telescope. Furthermore, the spatial resolution of the Hacar et al. (2013) data is $60''$, $\sim 0.04 \text{ pc}$ for Taurus, which is 140 pc away (Elias, 1978). The observations have a noise rms of $\sim 0.1 \text{ K}$ per velocity channel. The synthetic image from RADMC-3D is noiseless and has better spatial and velocity resolution than the Hacar et al. (2013) data, 0.01 pc and 0.025 km/s respectively. Thus, the image is degraded by rebinning the velocity channels, and then convolving each velocity channel map with a 2D-Gaussian with a FWHM of 0.04 pc and adding noise. For each voxel, the noise is obtained by sampling from a Gaussian distribution with a mean of zero and a standard deviation of 0.1 K.

Figure 6.3 shows the integrated C^{18}O emission map for one of the natural mix

turbulence simulations just before a sink particle forms. Only pixels with 5-sigma detections, i.e. $T_{\text{b}} > 0.5 \text{ K}$, are included. The contours show the true H_2 column density from the simulation convolved with the same 2D-Gaussian as the synthetic images, and has levels at: 0.5, 0.7, 2, 4, 5, 7, $20 \times 10^{22} \text{ cm}^{-2}$. One can see that the C^{18}O is tracing the filament morphology well; however, due to freeze-out, the CO peaks are often offset from the true H_2 column density peaks. The integrated emission map shows no obvious sign of fibres, similar to the results of Hacar et al. (2013).

Figure 6.4 shows the first moment of the C^{18}O emission map for the same image, overlaid with the same contours of true H_2 column density. The intensity-weighted mean velocity varies by $\sim 2 \text{ km/s}$, similar to the range seen in L1495 (Tafalla & Hacar, 2015). The filament shows large alternating velocity gradients in the radial directions.

Figure 6.5 shows the second moment of the C^{18}O emission map. Here one sees that the intensity-weighted velocity dispersion varies greatly over the filament, from transonic to supersonic levels. Those regions which exhibit large gradients in intensity-weighted mean velocity also show large intensity-weighted velocity dispersion. This is suggestive of multiple velocity components.

By looking at the spectrum of each pixel one can see that in the central region of the filament there are multiple velocity components (figure 6.6). This suggests that the elongated sub-structures apparent in the column density could be observed as fibres. The upper and lower regions of the filament show mainly single velocity components, with widths of $\sim 0.4 \text{ km/s}$, comparable to the average velocity dispersion calculated in the previous chapter. As mentioned above, the width of these lines is much greater than the unresolved turbulence on scales smaller than the grid size, thus adding micro-turbulence would not significantly alter the synthetic cubes.

6.4 DISCUSSION

To investigate the multiple velocity components that are apparent in the filament I use position-velocity diagrams. This allows one to distinguish between small localised regions with multiple velocity components, i.e. cores, and elongated regions which would be identified as fibres. Figure 6.7 shows longitudinal stripes of the integrated emission map seen in PV space. What appears to be a single filament in integrated emission is seen to actually be numerous elongated, velocity-coherent sub-structures, well separated in velocity, i.e. fibres. This can also be seen in figure 6.8 which shows radial stripes of the integrated emission map in PV space. Here one can see that numerous fibres can co-exist parallel to each other, separated by $\sim 1 \text{ km/s}$ in

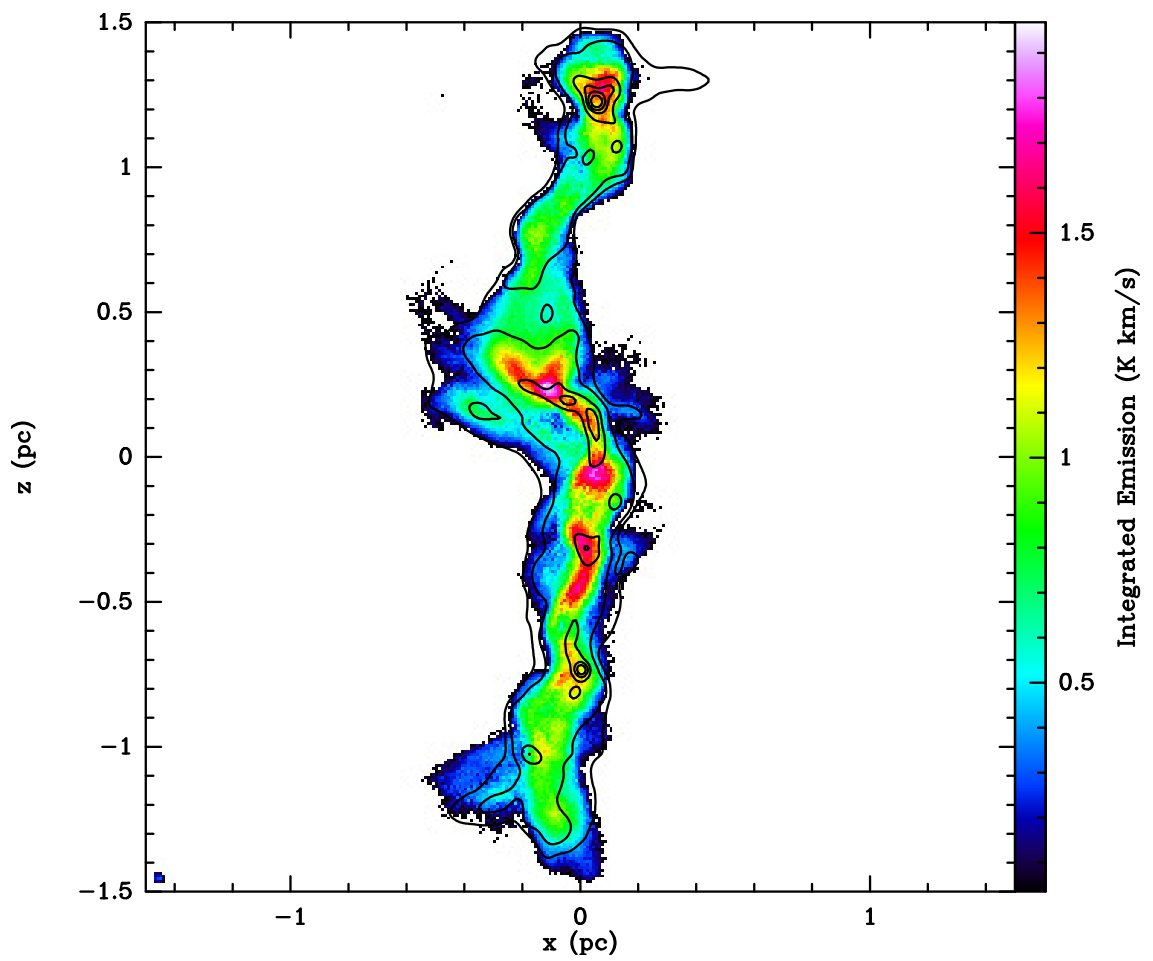


Figure 6.3. Integrated emission map of C¹⁸O for a natural mix turbulence simulation just before the first sink particle forms. The contours show the true H₂ column density from the simulation with levels: 0.5, 0.7, 2, 4, 5, 7, 20 × 10²² cm⁻².

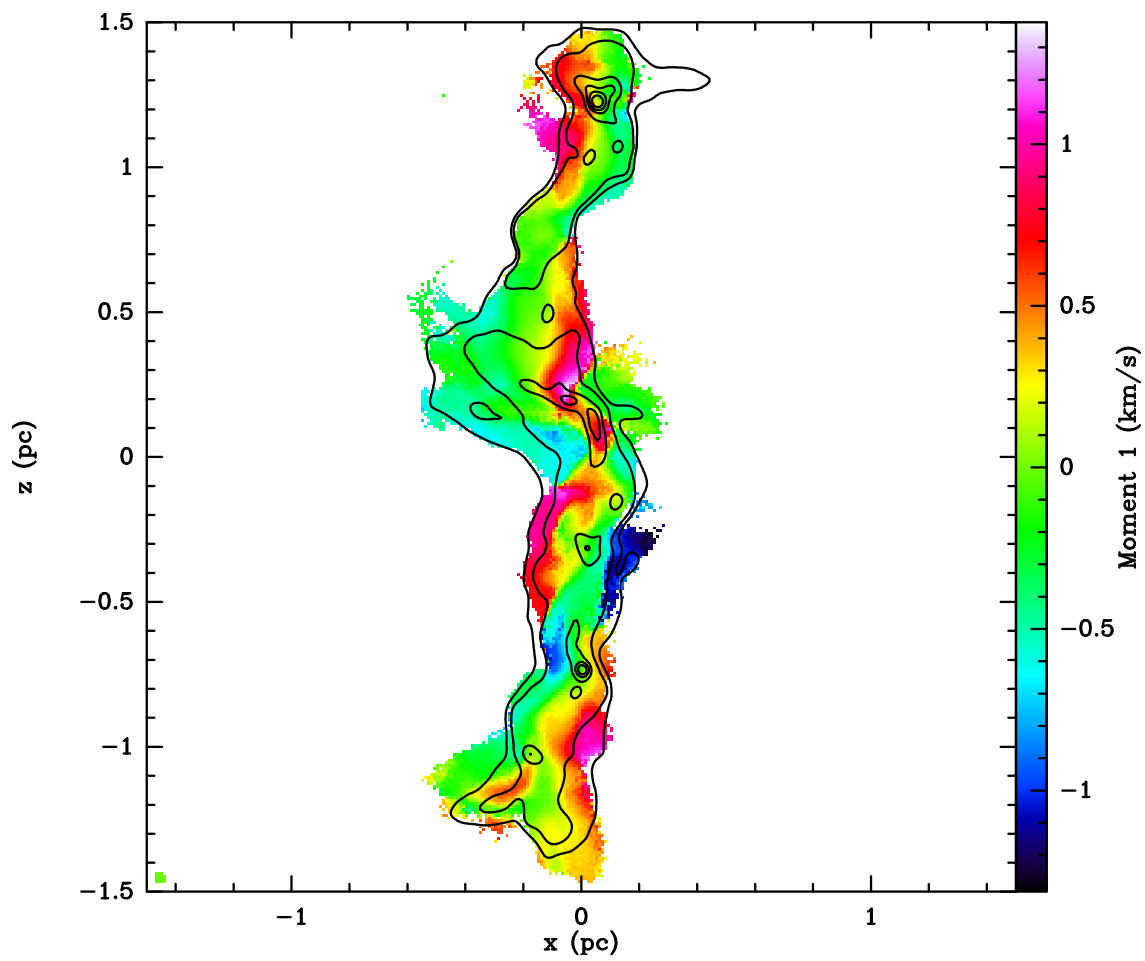


Figure 6.4. Intensity-weighted mean velocity of C^{18}O for a natural mix turbulence simulation just before the first sink particle forms. The contours show the true H_2 column density from the simulation with levels: 0.5, 0.7, 2, 4, 5, 7, $20 \times 10^{22} \text{ cm}^{-2}$.

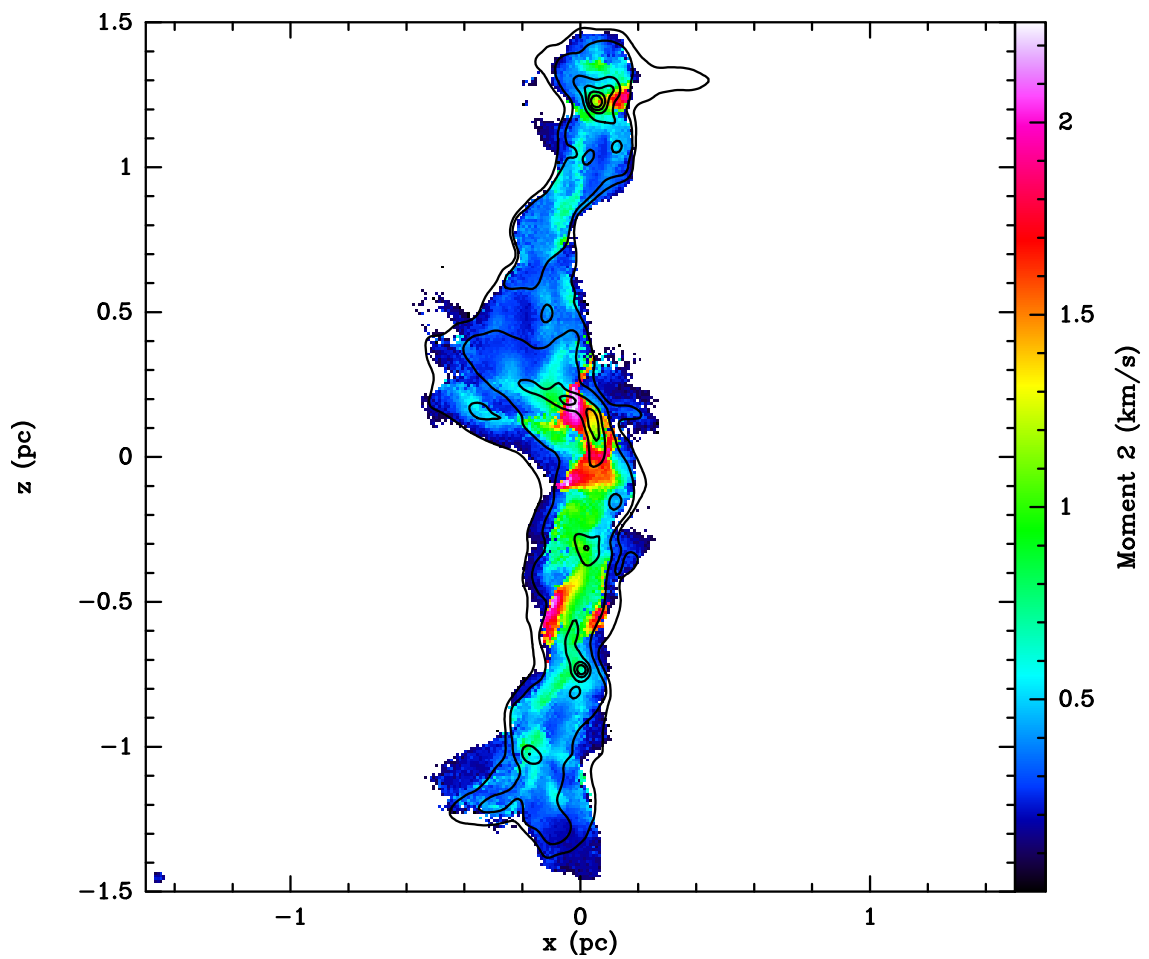


Figure 6.5. Intensity-weighted velocity dispersion of $C^{18}O$ for a natural mix turbulence simulation just before the first sink particle forms. The contours show the true H_2 column density from the simulation with levels: 0.5, 0.7, 2, 4, 5, 7, $20 \times 10^{22} \text{ cm}^{-2}$.

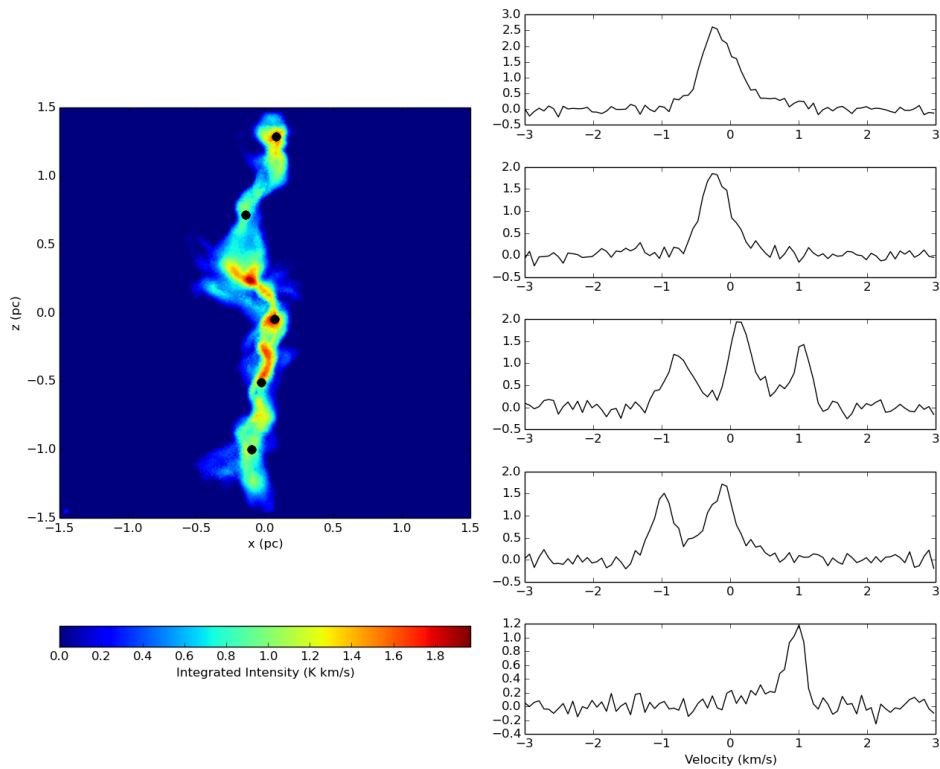


Figure 6.6. $C^{18}O$ spectra at 5 separate pixel locations. The positions of the pixels are shown with the black circles on the integrated intensity map, with the top circle showing the position of the top spectrum and so forth. One can see that there are a number of locations which have multiple velocity components along the line of sight.

velocity but only ~ 0.1 pc in the radial direction. Fitting the C^{18}O spectra for each pixel, taking into consideration the multiple velocity components, is the next obvious step and will be explored in future work.

As mentioned in the previous chapter, dendrograms are unable to differentiate large differences in PPP sub-structure when constructed using column density maps. With the additional velocity information, dendrograms constructed using PPV data may be able to. Here I use the PYTHON package ASTRODENDRO*. Dendrograms are first constructed from three dimensional volume density cubes (i.e. PPP) with a resolution of 0.01 pc at the snapshot before the first sink particle forms. The dendrograms are constructed using the parameters: $\text{min_value} = 10^{-20} \text{ g/cm}^3$, the lowest density that a data point must have to be considered when building the dendrogram; $\text{min_delta} = 5 \times 10^{-21} \text{ g/cm}^3$, the minimum density contrast between a leaf and its branch; and $\text{min_npix} = 100$, the minimum number of pixels needed for a leaf to be considered a true structure, corresponding to a sphere with a radius ~ 0.03 pc. These are the same parameters as used in the previous chapter.

The number of leaves in a dendrogram, N_{leaf} , tells one how fragmented a structure is; and the number of levels, N_{level} , from the highest leaf tells one how hierarchical the structure is. I obtain the same results as in the previous chapter, a natural mix of turbulent modes produces both a more fragmented and a more hierarchical structure than the purely compressive turbulence: $N_{\text{leaf}} = 41.8 \pm 2.7$ and $N_{\text{level}} = 26.8 \pm 1.7$ for the natural mix case, and $N_{\text{leaf}} = 27.7 \pm 1.4$ and $N_{\text{level}} = 18.3 \pm 1.5$ for the purely compressive case. Though the exact values of N_{leaf} and N_{level} change when I use different values for min_value , min_delta and min_npix to construct the dendrograms, the result that the natural mix turbulence is more fragmented and hierarchical does not change.

To construct the dendrograms from the three-dimensional position-position-velocity (PPV) emission datacube I use $\text{min_value} = 0.3 \text{ K}$, $\text{min_delta} = 0.3 \text{ K}$, and $\text{min_npix} = 48$. These values of min_value and min_delta correspond to the 3-sigma noise level. The value of min_npix roughly corresponds to the ‘beamsize’, i.e. the square of the FWHM of the Gaussian kernel used to degrade the image, multiplied by 3 velocity channels. The dendrograms constructed using the synthetic PPV cube suggest a small difference in structure between the two sets of simulations; $N_{\text{leaf}} = 50.1 \pm 3.1$ and $N_{\text{level}} = 24.5 \pm 2.0$ for the natural mix case, and $N_{\text{leaf}} = 45.5 \pm 2.1$ and $N_{\text{level}} = 20.2 \pm 1.8$ for the purely compressive case. Note that the mean values of N_{leaf} and N_{level} are lower for the purely compressive simulations, as is the case in PPP space, but they lie within 2-sigma of each other, meaning that one cannot call the

*<http://www.dendrograms.org>

difference statistically significant. This is unfortunate as observers do not have access to the volume density PPP structure of filaments and rely on line-of-sight velocities to disentangle projected structures.

The reason why dendrograms are unable to differentiate statistically between the natural and compressive turbulence may be due to line-of-sight confusion, where structures in PPP space are not well mapped to PPV space. This can be seen in figure 6.9. Line-of-sight confusion causes ‘blending’ to occur, where structures which are separated in PPP space are seen to be continuous in PPV. More worrying is that the emission from multiple, well separated peaks in PPV space can be due to single extended regions in PPP space which contain small regions with large velocity gradients. The troughs in emission at certain velocity seems to coincide with accretion shocks onto the fibres, most apparent in the third spectrum in figure 6.9. Thus, what is spatially a connected structure appears disconnected in velocity space.

6.5 CONCLUSIONS

Synthetic observations are crucial at linking simulations with observations. Filament fragmentation produces complex features in both density and velocity, making direct comparisons between simulated filaments and observed filaments difficult.

Simulations using the moving-mesh code AREPO produce the same elongated sub-structures as the simulations using the smoothed particle hydrodynamic code GANDALF presented in the previous chapter. Synthetic $C^{18}O$ observations of these filaments show numerous elongated, velocity coherent sub-filaments which are well separated in velocity, termed fibres by Hacar & Tafalla (2011). Thus, fray and fragment is a plausible formation mechanism for the fibre structures seen in Taurus.

However, the poor performance of PPV dendrograms in differentiating significantly variations in PPP sub-structure, and the common line-of-sight confusion which results in both blending and artificial separation of features in PPV space, suggests that there may be no clear mapping between the fibre-like structures in PPP space and the fibres observed in PPV space. More work must be done to investigate the connection between PPV fibres and their PPP counterparts. Additional synthetic observations of these simulations from numerous viewing angles and in different chemical tracers will help.

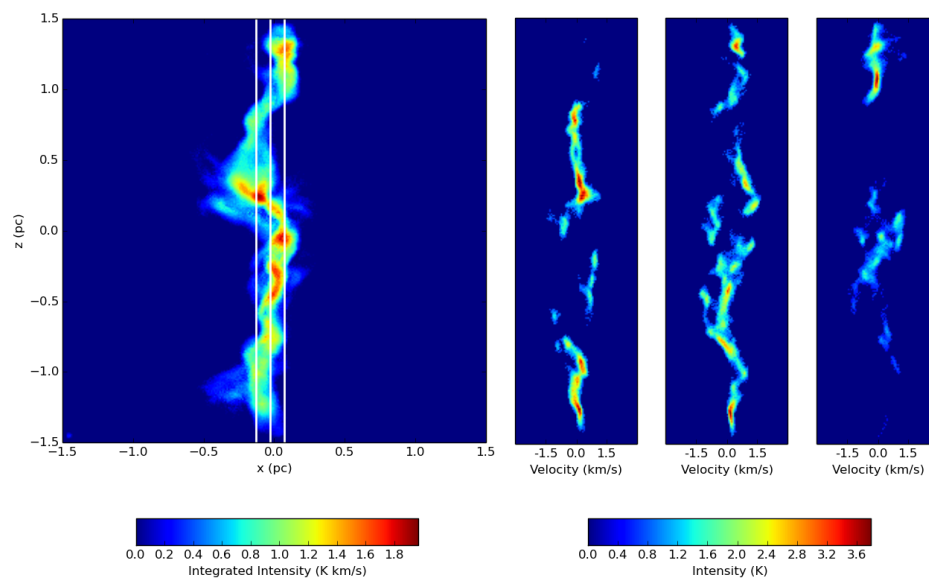


Figure 6.7. Longitudinal stripes taken from the integrated emission map and viewed in position-velocity space, where the leftmost stripe corresponds to the leftmost PV diagram and so forth. One can see what appears to be a single filament in integrated emission is found to be several smaller velocity-coherent sub-filaments which are well separated in velocity, i.e. fibres.

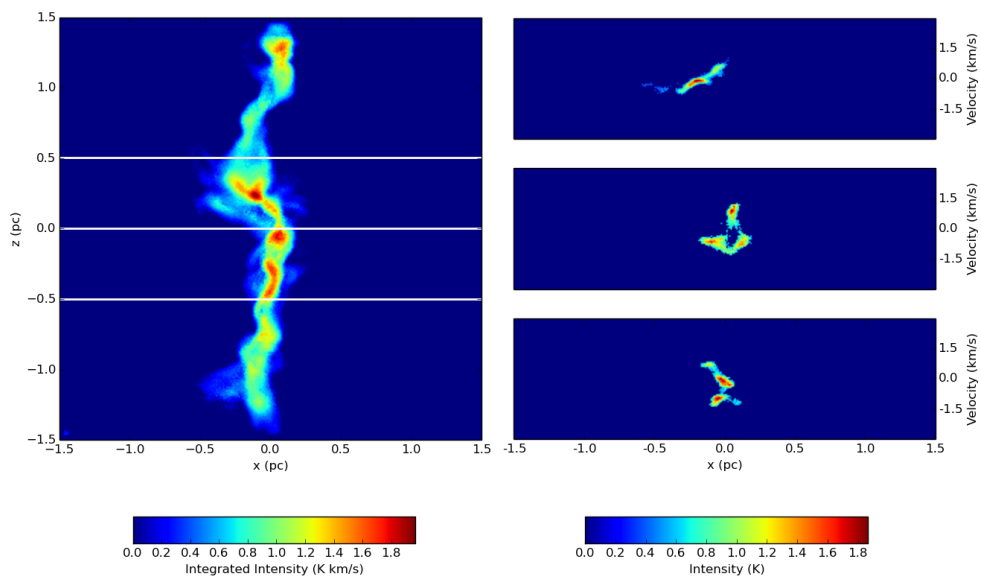


Figure 6.8. Horizontal stripes taken from the integrated emission map and viewed in position-velocity space, where the uppermost stripe corresponds to the uppermost PV diagram and so forth. The fibres are well separated in velocity space, ~ 1 km/s, even though they are only separated by ~ 0.1 pc in the radial direction.

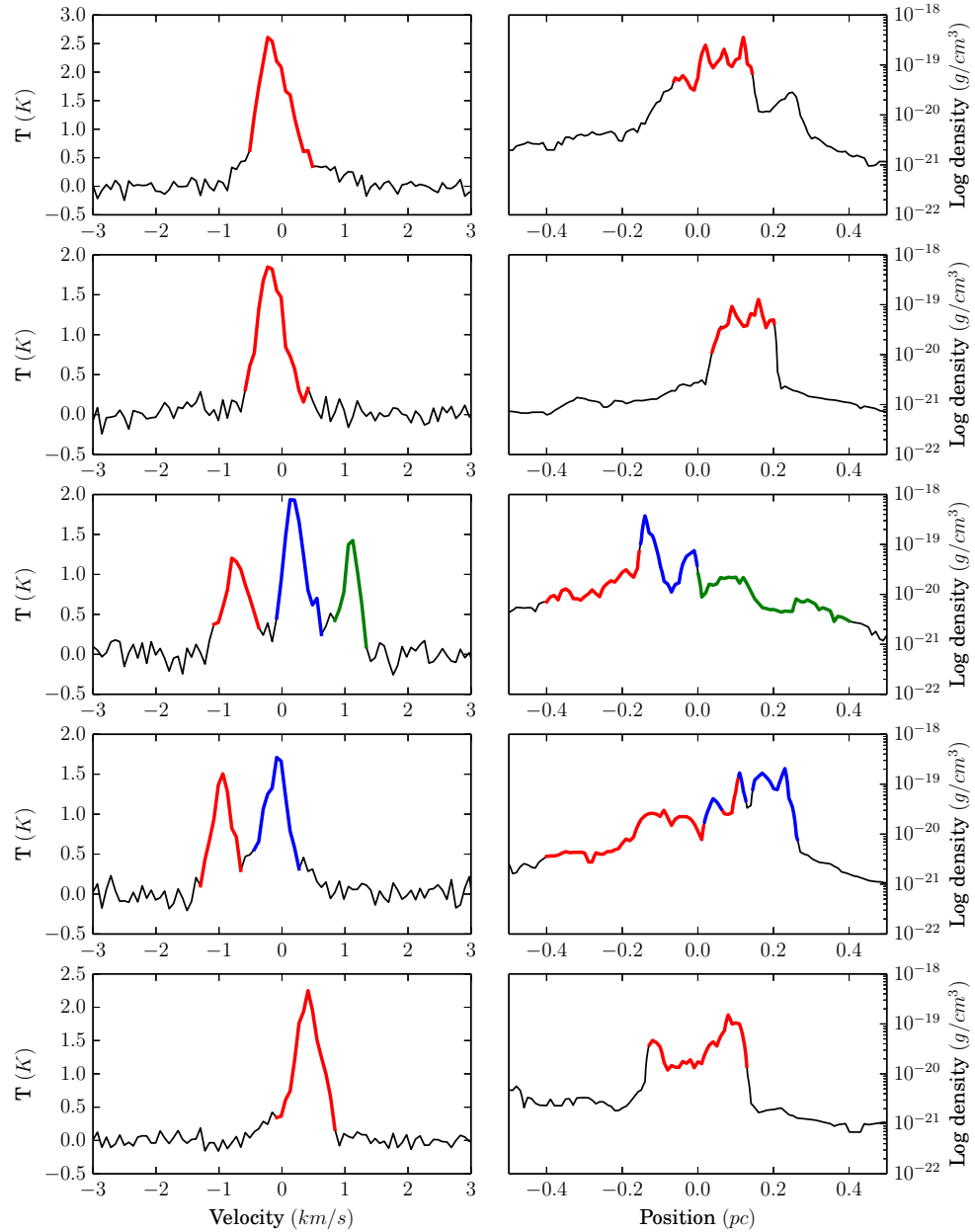


Figure 6.9. On the left are the same 5 spectra seen in figure 6.6, on the right is the density along the line of sight for those spectra. The colours show the gas that is contributing to the same colour peak in emission. Line of sight confusion is evident in a number of cases, where multiple separated peaks in density are blended into single peaks in emission, and where numerous peaks in emission are not coming from separated regions in PPP space.

CHAPTER 7

SUMMARY OF THIS THESIS

7.1 GLOBAL COLLAPSE OF FILAMENTS

In chapter 3 I present work examining the manner in which filaments collapse along their longitudinal axes. Global collapse timescales are found to differ considerably from what previous analytic work has predicted. Rather than two modes of possible global collapse, homologous and end-dominated, I find that all filaments collapse via the end-dominated mode. Moreover, the collapse timescale has a linear dependence on the initial aspect ratio of the filament, not the predicted square root dependence. The difference is due to previous work neglecting the effects of the end-clumps on the interior filament gas. The end-clumps dominate the local gravitational field as they grow more massive, causing gas in the filament to be accelerated outwards and assert a large ram pressure on the infalling end-clump. By developing a semi-analytic model of this phenomenon I show that the interplay between gravitational global collapse and accretion ram pressure leads to the end-clumps reaching a stable terminal velocity.

As the global collapse timescale for a filament is much longer than that of a sphere of the same density, filamentary structures are able to fragment into cores long before global collapse takes over. Moreover, as the global collapse produces large dense end-clumps it may mean that filaments are ideal sites for high mass star formation. Recent observations of isolated filamentary clouds show that some have massive cores at either end of the filament. I show that for such a filament, one can use the ratio of column density in the end clump and the column density in the filament to estimate the age of the filament, and apply this to IRDC 18223.

7.2 PERTURBATION GROWTH IN ACCRETING FILAMENTS

In chapter 4 I present a new numerical perturbation analysis applied to accreting infinitely long filaments and argue that previous analytic perturbation analyses of equilibrium filaments do not apply to filaments which interact with their surroundings via accretion. This is because a filament does not form in equilibrium and is unable to reach equilibrium before accretion causes it to become super-critical. The dispersion relation describing the growth of perturbations in such non-equilibrium accreting filaments is dominated by the interplay between longitudinal oscillations and radial accretion. I show that the dominant wavelength is no longer determined by the filament's diameter, but rather the temperature of the gas and the accretion rate onto the filament; and that the dominant wavelength is still the fastest growing when a filament is seeded with multi-wavelength perturbations.

These results allow one to constrain the age and accretion history of a filament which is fragmenting into quasi-periodically spaced cores. I apply this model to the fibres seen in Taurus (Tafalla & Hacar, 2015) and IRDC 18223 (Beuther et al., 2015) and derive ages and accretion rates consistent with observations. I also show that the out-of-phase density and velocity oscillations indicative of perturbation growth in filaments are seen in numerous fragmenting filaments.

7.3 FRAGMENTATION OF FILAMENTS ACCRETING FROM A TURBULENT MEDIUM

In chapter 5 I extend my fragmentation study to include the effects of turbulence in the accreting medium. I show that the addition of turbulence complicates the perturbation analysis carried out in chapter 4. The amount of turbulence, and the resulting inhomogeneities in the accretion flow, produces significant differences in filament morphology and fragmentation. Filaments which accrete from a roughly subsonic and mildly inhomogeneous flow show hierarchical two-tiered fragmentation. The filament first fragments into large scale structures with wide separations determined by a modified version of the dispersion relation derived in chapter 4. Next, these fragments proceed to further fragment into cores with separations determined by the effective Jeans length.

Increased energy in the turbulent velocity field leads to the formation of elongated fibre-like sub-structures in the main filament, similar to the fray and fragment scenario of fibre production proposed by Tafalla & Hacar (2015). The formation of these fibre-like structures is linked to the velocity field in the main filament: where

there exists a large gradient in vorticity, the velocity field gathers gas together to form dense structures. Since the filament's internal velocity dispersion is insensitive to the initial level of turbulence in the accretion flow, and tends to a sonic level due to accretion driving, the large differences in filament morphology and fragmentation are due to inhomogeneities in the accretion flow.

These simulations show that fibre-bearing filaments are able to maintain a large radial extents even when they are thermally super-critical. It is possible that significant levels of sub-structure are able to delay the onset of radial collapse, thus explaining the 0.1 pc widths seen in super-critical filaments.

7.4 SYNTHETIC IMAGES OF FRAGMENTING FILAMENTS

In chapter 6 I present the results of simulations of fragmenting filaments using the moving-mesh code AREPO. These simulations include time-dependent chemistry and coupled thermodynamics. Elongated fibre-like sub-structures form in the main filament, as in the smoothed particle hydrodynamic simulations. I present synthetic $C^{18}O$, $J = 1 - 0$, images with spatial and velocity resolution comparable to the Hacar et al. (2013) observations of the same line and tracer. Using these images I show that these filaments contain a number of elongated, velocity-coherent sub-filaments, well separated in velocity, similar to the fibres identified in Hacar et al. (2013).

Dendrograms are often constructed using position-position-velocity data to objectively quantise a structure into its component sub-structures. I show that dendrograms constructed from PPV data are unable to detect a difference in sub-structure between filaments embedded in natural and compressive turbulent conditions. This is despite there being considerable differences in sub-structures when dendrograms are constructed using PPP data.

Furthermore, I show that the mapping between PPP and PPV data is complex and subject to line-of-sight confusion. This leads to extended and sub-structured regions in PPP becoming a single monolithic feature in PPV, thus losing information about structure. Additionally, the inverse is true; regions which are extended and continuous in PPP space can become artificially separated in PPV space due to shocks caused by converging flows.

7.5 FUTURE WORK

As observations have shown the importance of filaments to the star formation process it has become clear that our theoretical understanding is lacking, it has been

confined to the ideal equilibrium case. The results of this thesis help to broaden the theoretical framework to include non-equilibrium accreting filaments, but there is still much to be done. Here I present some ideas of future work.

7.5.1 GLOBAL COLLAPSE AND DYNAMICS

- In this thesis I present results for the global longitudinal collapse of filaments. However, these simulations use an ideal setup in which there is a well defined edge to the filament. Previous analytic work suggests that such a well defined edge acts to enhance the longitudinal gravitational acceleration that the gas experiences, speeding up collapse. One could perform simulations which use different tapering lengths to investigate this phenomenon and study its effect. Column density maps from Herschel will be useful to constrain such tapering lengths.
- Most filaments are not isolated, but rather form hub-filament systems (Myers, 2009). Recent observations have shown that large scale velocity motions can exist within the filaments, suggestive of global collapse feeding material into the hub (e.g. Peretto et al., 2013). Simulations which attempt to parametrise such structures and provide a model to compare with observations are sorely needed.

7.5.2 FILAMENT FRAGMENTATION

- The simulations presented in this thesis use an ideal set-up to approximate the formation of a filament; a larger simulation, such as a turbulent cloud simulation, forms the filament in a self-consistent manner. The extraction of filaments from these simulations and a study of their evolution and fragmentation would be the next step in developing the models presented here.
- There is still additional analysis to be performed on the synthetic observation and simulations shown in chapter 6. The spectra can be fitted with Gaussian distributions to determine intensities, centroids and widths for each individual velocity component, allowing a friends-of-friends algorithm to be used to find fibres as shown in Hacar et al. (2013). A filament finding algorithm could also be used on the PPP simulation and a comparison could be made between PPP and PPV space, similar to the comparison using dendrograms in chapter 6.
- The synthetic observations presented in chapter 6 take the y -axis as the line-of-sight, additional observations using different lines-of-sight will help understand

the effects of line-of-sight confusion and the appearance of the fibrous structure in PPV space. Furthermore, observations using different tracers, such as N_2H^+ , and different lines, such as $\text{C}^{18}\text{O } J = 2 - 1$, will allow more comparisons with the observations presented in Hacar et al. (2013) and Tafalla & Hacar (2015).

- It is still unclear which mechanism is dominant in the formation of fibres: fray & fragment, or fragment & gather. Cloud-scale simulations which contain sufficient resolution within the main filament may be able to help determine the dominant mechanism. Moreover, with the use of synthetic images one could attempt to find a distinguishing feature between the two mechanisms.
- There have been no observations of fibres in thermally sub-critical filaments. This may be due to the low number of filaments so far studied; or it may be due to the fact there exists a line-density threshold for fibre formation. Neither formation mechanism would be able to explain this. A survey of nearby Gould belt filaments using a molecular tracer, i.e. C^{18}O , is needed. Such data can then be compared to the fray and fragment model presented here.
- The nature of turbulence, whether it is decaying or driven, has been seen in simulations to determine the core-core velocity dispersion in a cloud (Offner et al., 2008). Accretion onto filaments drives turbulence on much smaller length scales, of the order of the filament's radius. The effect that this has on the core-core velocity dispersion within a filament has yet to be examined. The simulations and synthetic images presented in chapter 6 are able to do this. Recent observations of the Gould belt in NH_3 by the GAS survey (Pineda, Friesen & the GBT Ammonia Survey Team, 2016) provide a wealth of kinematic data with which to compare my simulations.
- Previous analytic work investigating the fragmentation of magnetised filaments has shown that the strength and configuration of the magnetic field can significantly change the fragmentation of a filament. However, as with other previous work, this confined itself to the ideal equilibrium case. Simulations with the same set-up and initial conditions as those presented in this thesis, but including ideal-MHD, can be carried out using codes such as AREPO or FLASH to investigate the effect magnetic fields have on non-equilibrium filaments.
- As shown in chapter 5, fibrous filaments do not radially collapse when they become thermally super-critical. This may explain the numerous observations of

super-critical filaments with widths comparable to sub-critical filaments (Arzoumanian et al., 2011). An attempt must be made to understand this analytically within the context of the Ostriker (1964) stability study.

7.5.3 FILAMENTS AND FEEDBACK

- The simulations presented in this thesis have lacked feedback mechanisms. For low mass star forming regions the feedback from jets and outflows is considered to be important. The unique geometry of a filament means that the relative alignment of jets to their parent filament will significantly change the amount of energy and momentum injected into the system. Simulations which include such feedback, and importantly are able to resolve down to the disc level so as to be confident of jet alignments, are needed to study the effect that such feedback has on the filament's internal turbulence and fragmentation.
- Filaments are thought to be excellent sites for high-mass star formation due to their geometry (e.g. Peretto et al., 2013; Beuther et al., 2015). As with feedback from jets, the effect of HII regions on filamentary structures has not been explored fully. One could expect that HII regions may be able to escape in the radial direction and allow mass accretion to continue, helping to form higher mass stars. However, recent work looking at 2 dimensional sheets formed via cloud-cloud collisions has shown that lower dimensionality may actually increase the dispersal rate of the gas once a massive star forms (Balfour et al. in press.).

BIBLIOGRAPHY

- Alves J. F., Lada C. J., Lada E. A., 2001, *Nature*, 409, 159
- André P., Di Francesco J., Ward-Thompson D., Inutsuka S.-I., Pudritz R. E., Pineda J. E., 2014, *Protostars and Planets VI*, 27
- André P. et al., 2010, *A&A*, 518, L102
- André P. et al., 2016, *A&A*, 592, A54
- Arzoumanian D. et al., 2011, *A&A*, 529, L6
- Arzoumanian D., André P., Peretto N., Könyves V., 2013, *A&A*, 553, A119
- Balfour S. K., Whitworth A. P., Hubber D. A., Jaffa S. E., 2015, *MNRAS*, 453, 2471
- Ballesteros-Paredes J., 2006, *MNRAS*, 372, 443
- Ballesteros-Paredes J., Hartmann L., Vázquez-Semadeni E., 1999, *ApJ*, 527, 285
- Ballesteros-Paredes J., Klessen R. S., Vázquez-Semadeni E., 2003, *ApJ*, 592, 188
- Barnard E. E., 1910, *ApJ*, 31
- Barnes J., Hut P., 1986, *Nature*, 324, 446
- Bastien P., 1983, *A&A*, 119, 109
- Bastien P., Arcoragi J.-P., Benz W., Bonnell I., Martel H., 1991, *ApJ*, 378, 255
- Basu S., Ciolek G. E., Dapp W. B., Wurster J., 2009, *New A*, 14, 483
- Bate M. R., Bonnell I. A., Price N. M., 1995, *MNRAS*, 277, 362
- Bate M. R., Tricco T. S., Price D. J., 2014, *MNRAS*, 437, 77
- Berger M. J., Colella P., 1989, *Journal of Computational Physics*, 82, 64

- Bergin E. A., Tafalla M., 2007, *ARA&A*, 45, 339
- Beuther H., Ragan S. E., Johnston K., Henning T., Hacar A., Kainulainen J. T., 2015, *A&A*, 584, A67
- Black J. H., 1994, in *Astronomical Society of the Pacific Conference Series*, Vol. 58, *The First Symposium on the Infrared Cirrus and Diffuse Interstellar Clouds*, Cutri R. M., Latter W. B., eds., p. 355
- Blitz L., Rosolowsky E., 2005, in *Astrophysics and Space Science Library*, Vol. 327, *The Initial Mass Function 50 Years Later*, Corbelli E., Palla F., Zinnecker H., eds., p. 287
- Blitz L., Williams J. P., 1999, in *NATO Advanced Science Institutes (ASI) Series C*, Vol. 540, *NATO Advanced Science Institutes (ASI) Series C*, Lada C. J., Kylafis N. D., eds., p. 3
- Bonnell I. A., Bate M. R., Vine S. G., 2003, *MNRAS*, 343, 413
- Burkert A., Bodenheimer P., 1993, *MNRAS*, 264, 798
- Burkert A., Hartmann L., 2004, *ApJ*, 616, 288
- Caselli P., Walmsley C. M., Tafalla M., Dore L., Myers P. C., 1999, *ApJ*, 523, L165
- Christie H. et al., 2012, *MNRAS*, 422, 968
- Clark P. C., Bonnell I. A., 2004, *MNRAS*, 347, L36
- Clark P. C., Bonnell I. A., 2005, *MNRAS*, 361, 2
- Clark P. C., Bonnell I. A., Zinnecker H., Bate M. R., 2005, *MNRAS*, 359, 809
- Clark P. C., Glover S. C. O., 2015, *MNRAS*, 452, 2057
- Clark P. C., Glover S. C. O., Klessen R. S., 2012, *MNRAS*, 420, 745
- Clarke S. D., Whitworth A. P., 2015, *MNRAS*, 449, 1819
- Commerçon B., Audit E., Chabrier G., Chièze J.-P., 2011, *A&A*, 530, A13
- Contreras Y., Garay G., Rathborne J. M., Sanhueza P., 2016, *MNRAS*, 456, 2041
- Cox N. L. J. et al., 2016, *A&A*, 590, A110
- Crutcher R. M., 1999, *ApJ*, 520, 706

- Dale J. E., Bonnell I., 2011, MNRAS, 414, 321
- Dale J. E., Bonnell I. A., Clarke C. J., Bate M. R., 2005, MNRAS, 358, 291
- Dale J. E., Ercolano B., Bonnell I. A., 2013, MNRAS, 430, 234
- Dib S., Walcher C. J., Heyer M., Audit E., Loinard L., 2009, MNRAS, 398, 1201
- Dobbs C. L., 2015, MNRAS, 447, 3390
- Drabek-Maunder E., Hatchell J., Buckle J. V., Di Francesco J., Richer J., 2016, MNRAS, 457, L84
- Draine B. T., 1978, ApJS, 36, 595
- Duarte-Cabral A., Chrysostomou A., Peretto N., Fuller G. A., Matthews B., Schieven G., Davis G. R., 2012, A&A, 543, A140
- Dullemond C. P., 2012, RADMC-3D: A multi-purpose radiative transfer tool. Astrophysics Source Code Library
- Elias J. H., 1978, ApJ, 224, 857
- Elmegreen B. G., 2000, ApJ, 530, 277
- Federrath C., 2016, MNRAS, 457, 375
- Fehér O., Tóth L. V., Ward-Thompson D., Kirk J., Kraus A., Pelkonen V.-M., Pintér S., Zahorecz S., 2016, A&A, 590, A75
- Fernández-López M. et al., 2014, ApJ, 790, L19
- Fiege J. D., Pudritz R. E., 2000, MNRAS, 311, 105
- Fischera J., Martin P. G., 2012, A&A, 542, A77
- Franco J., Tenorio-Tagle G., Bodenheimer P., 1990, ApJ, 349, 126
- Freundlich J., Jog C. J., Combes F., 2014, A&A, 564, A7
- Giannetti A. et al., 2016, in EAS Publications Series, Vol. 75, EAS Publications Series, pp. 147–151
- Gingold R. A., Monaghan J. J., 1977, MNRAS, 181, 375
- Glover S. C. O., Clark P. C., 2012a, MNRAS, 421, 116

- Glover S. C. O., Clark P. C., 2012b, MNRAS, 421, 9
- Glover S. C. O., Clark P. C., 2012c, MNRAS, 426, 377
- Glover S. C. O., Clark P. C., 2014, MNRAS, 437, 9
- Glover S. C. O., Federrath C., Mac Low M.-M., Klessen R. S., 2010, MNRAS, 404, 2
- Glover S. C. O., Mac Low M.-M., 2007a, ApJS, 169, 239
- Glover S. C. O., Mac Low M.-M., 2007b, ApJ, 659, 1317
- Goldbaum N. J., Krumholz M. R., Matzner C. D., McKee C. F., 2011, ApJ, 738, 101
- Gómez G. C., Vázquez-Semadeni E., 2014, ApJ, 791, 124
- Gritschneider M., Heigl S., Burkert A., 2016, ArXiv e-prints
- Gritschneider M., Naab T., Walch S., Burkert A., Heitsch F., 2009, ApJ, 694, L26
- Habing H. J., 1968, Bull. Astron. Inst. Netherlands, 19, 421
- Hacar A., Kainulainen J., Tafalla M., Beuther H., Alves J., 2016, A&A, 587, A97
- Hacar A., Tafalla M., 2011, A&A, 533, A34
- Hacar A., Tafalla M., Kauffmann J., Kovács A., 2013, A&A, 554, A55
- Hartmann L., 2002, ApJ, 578, 914
- Heitsch F., 2013, ApJ, 769, 115
- Heitsch F., Hartmann L. W., Slyz A. D., Devriendt J. E. G., Burkert A., 2008, ApJ, 674, 316
- Heitsch F., Mac Low M.-M., Klessen R. S., 2001, ApJ, 547, 280
- Hennebelle P., 2013, A&A, 556, A153
- Hennebelle P., André P., 2013, A&A, 560, A68
- Hernquist L., Bouchet F. R., Suto Y., 1991, ApJS, 75, 231
- Hill A. S., Joung M. R., Mac Low M.-M., Benjamin R. A., Haffner L. M., Klingenberg C., Waagan K., 2012, ApJ, 750, 104
- Hollenbach D., Kaufman M. J., Bergin E. A., Melnick G. J., 2009, ApJ, 690, 1497

- Hubber D. A., Batty C. P., McLeod A., Whitworth A. P., 2011, *A&A*, 529, A27
- Hubber D. A., Walch S., Whitworth A. P., 2013, *MNRAS*, 430, 3261
- Inutsuka S.-i., 2001, *ApJ*, 559, L149
- Inutsuka S.-I., Miyama S. M., 1992, *ApJ*, 388, 392
- Inutsuka S.-i., Miyama S. M., 1997, *ApJ*, 480, 681
- Jackson J. M., Finn S. C., Chambers E. T., Rathborne J. M., Simon R., 2010, *ApJ*, 719, L185
- Jeans J. H., 1902, *Philosophical Transactions of the Royal Society of London Series A*, 199, 1
- Kainulainen J., Hacar A., Alves J., Beuther H., Bouy H., Tafalla M., 2016a, *A&A*, 586, A27
- Kainulainen J., Ragan S. E., Henning T., Stutz A., 2013, *A&A*, 557, A120
- Kainulainen J., Stutz A. M., Stanke T., Abreu-Vicente J., Beuther H., Henning T., Johnston K. G., Megeath T., 2016b, *ArXiv e-prints*
- Kirk H., Myers P. C., Bourke T. L., Gutermuth R. A., Hedden A., Wilson G. W., 2013, *ApJ*, 766, 115
- Klessen R., 1997, *MNRAS*, 292, 11
- Klessen R. S., Hennebelle P., 2010, *A&A*, 520, A17
- Könyves V. et al., 2015, *A&A*, 584, A91
- Krumholz M. R., 2006, *ApJ*, 641, L45
- Krumholz M. R. et al., 2014, *Protostars and Planets VI*, 243
- Krumholz M. R., Klein R. I., McKee C. F., 2007, *ApJ*, 656, 959
- Krumholz M. R., Matzner C. D., 2009, *ApJ*, 703, 1352
- Lada C. J., Alves J., Lada E. A., 1999, *ApJ*, 512, 250
- Larson R. B., 1969, *MNRAS*, 145, 271
- Larson R. B., 1981, *MNRAS*, 194, 809

- Larson R. B., 1985, MNRAS, 214, 379
- Leitherer C., Robert C., Drissen L., 1992, ApJ, 401, 596
- Li Z.-Y., Wang P., Abel T., Nakamura F., 2010, ApJ, 720, L26
- Lippok N. et al., 2013, A&A, 560, A41
- Lomax O., Whitworth A. P., Cartwright A., 2013, MNRAS, 436, 2680
- Lomax O., Whitworth A. P., Hubber D. A., 2015, MNRAS, 449, 662
- Lopez L. A., Krumholz M. R., Bolatto A. D., Prochaska J. X., Ramirez-Ruiz E., 2011, ApJ, 731, 91
- Lucy L. B., 1977, AJ, 82, 1013
- Marsh K. A. et al., 2016, MNRAS, 459, 342
- Masunaga H., Inutsuka S.-i., 2000, ApJ, 531, 350
- Masunaga H., Miyama S. M., Inutsuka S.-i., 1998, ApJ, 495, 346
- McKee C. F., Ostriker J. P., 1977, ApJ, 218, 148
- McKee C. F., Zweibel E. G., Goodman A. A., Heiles C., 1993, in *Protostars and Planets III*, Levy E. H., Lunine J. I., eds., p. 327
- Miyama S. M., Narita S., Hayashi C., 1987, *Progress of Theoretical Physics*, 78, 1273
- Monaghan J. J., 1997, *Journal of Computational Physics*, 136, 298
- Monaghan J. J., 2002, MNRAS, 335, 843
- Monaghan J. J., Lattanzio J. C., 1985, A&A, 149, 135
- Morris J. P., Monaghan J. J., 1997, *Journal of Computational Physics*, 136, 41
- Motte F., Andre P., Neri R., 1998, A&A, 336, 150
- Myers P. C., 2009, ApJ, 700, 1609
- Nagasawa M., 1987, *Progress of Theoretical Physics*, 77, 635
- Nelson R. P., Langer W. D., 1997, ApJ, 482, 796
- Offner S. S. R., Krumholz M. R., Klein R. I., McKee C. F., 2008, AJ, 136, 404

- Ostriker J., 1964, *ApJ*, 140, 1056
- Padoan P., Juvela M., Goodman A. A., Nordlund Å., 2001, *ApJ*, 553, 227
- Palmeirim P. et al., 2013, *A&A*, 550, A38
- Panopoulou G. V., Psaradaki I., Skalidis R., Tassis K., Andrews J. J., 2016, *ArXiv e-prints*
- Panopoulou G. V., Tassis K., Goldsmith P. F., Heyer M. H., 2014, *MNRAS*, 444, 2507
- Peñaloza C. H., Clark P. C., Glover S. C. O., Shetty R., Klessen R. S., 2016, *ArXiv e-prints*
- Peretto N. et al., 2013, *A&A*, 555, A112
- Pineda J. E., Friesen R., the GBT Ammonia Survey Team, 2016, in *American Astronomical Society Meeting Abstracts*, Vol. 227, American Astronomical Society Meeting Abstracts, p. 418.06
- Pineda J. E. et al., 2015, *Nature*, 518, 213
- Planck Collaboration et al., 2016, *A&A*, 586, A136
- Pon A., Johnstone D., Heitsch F., 2011, *ApJ*, 740, 88
- Pon A., Toalá J. A., Johnstone D., Vázquez-Semadeni E., Heitsch F., Gómez G. C., 2012, *ApJ*, 756, 145
- Porter D. H., Pouquet A., Woodward P. R., 1994, *Physics of Fluids (1994-present)*, 6, 2133
- Price D. J., 2007, *PASA*, 24, 159
- Price D. J., 2012, *Journal of Computational Physics*, 231, 759
- Price D. J., Monaghan J. J., 2004, *MNRAS*, 348, 139
- Ragan S. E., Henning T., Beuther H., Linz H., Zahorecz S., 2015, *A&A*, 573, A119
- Ragan S. E., Henning T., Tackenberg J., Beuther H., Johnston K. G., Kainulainen J., Linz H., 2014, *A&A*, 568, A73
- Redman M. P., Rawlings J. M. C., Nutter D. J., Ward-Thompson D., Williams D. A., 2002, *MNRAS*, 337, L17

- Rigby A. J. et al., 2016, MNRAS, 456, 2885
- Roman-Duval J., Heyer M., Brunt C. M., Clark P., Klessen R., Shetty R., 2016, ApJ, 818, 144
- Rosolowsky E. W., Pineda J. E., Kauffmann J., Goodman A. A., 2008, ApJ, 679, 1338
- Rosswog S., Davies M. B., Thielemann F.-K., Piran T., 2000, A&A, 360, 171
- Roy A. et al., 2015, A&A, 584, A111
- Saitoh T. R., Makino J., 2013, ApJ, 768, 44
- Savva D., Little L. T., Phillips R. R., Gibb A. G., 2003, MNRAS, 343, 259
- Scalo J., Elmegreen B. G., 2004, ARA&A, 42, 275
- Schneider S., Elmegreen B. G., 1979, ApJS, 41, 87
- Schöier F. L., van der Tak F. F. S., van Dishoeck E. F., Black J. H., 2005, A&A, 432, 369
- Seifried D., Walch S., 2015, MNRAS, 452, 2410
- Simpson R. J., Nutter D., Ward-Thompson D., 2008, MNRAS, 391, 205
- Smith R. J., Glover S. C. O., Klessen R. S., 2014, MNRAS, 445, 2900
- Sobolev V. V., 1957, Soviet Ast., 1, 678
- Springel V., 2011, in IAU Symposium, Vol. 270, Computational Star Formation, Alves J., Elmegreen B. G., Girart J. M., Trimble V., eds., pp. 203–206
- Stark A. A., Lee Y., 2005, ApJ, 619, L159
- Tafalla M., Hacar A., 2015, A&A, 574, A104
- Tafalla M., Myers P. C., Caselli P., Walmsley C. M., 2004, A&A, 416, 191
- Tavakoli M., 2012, ArXiv e-prints
- Teixeira P. S., Takahashi S., Zapata L. A., Ho P. T. P., 2016, A&A, 587, A47
- Tilley D. A., Pudritz R. E., 2004, MNRAS, 353, 769
- Toalá J. A., Vázquez-Semadeni E., Gómez G. C., 2012, ApJ, 744, 190

- Truelove J. K., Klein R. I., McKee C. F., Holliman, II J. H., Howell L. H., Greenough J. A., 1997, *ApJ*, 489, L179
- Van Loo S., Keto E., Zhang Q., 2014, *ApJ*, 789, 37
- Vazquez-Semadeni E., 1994, *ApJ*, 423, 681
- Vázquez-Semadeni E., Gómez G. C., Jappsen A. K., Ballesteros-Paredes J., González R. F., Klessen R. S., 2007, *ApJ*, 657, 870
- Vazquez-Semadeni E., Passot T., Pouquet A., 1995, in *Revista Mexicana de Astronomía y Astrofísica*, vol. 27, Vol. 3, *Revista Mexicana de Astronomía y Astrofísica Conference Series*, Pena M., Kurtz S., eds., p. 61
- Walch S., 2016, in *EAS Publications Series*, Vol. 75, *EAS Publications Series*, pp. 359–365
- Walch S., Naab T., 2015, *MNRAS*, 451, 2757
- Walch S. K., Whitworth A. P., Bisbas T., Wünsch R., Hubber D., 2012, *MNRAS*, 427, 625
- Whitworth A., 1979, *MNRAS*, 186, 59
- Whitworth A. P., 1998, *MNRAS*, 296, 442
- Whitworth A. P., 2016, *MNRAS*, 458, 1815
- Whitworth A. P., Ward-Thompson D., 2001, *ApJ*, 547, 317
- Wilson T. L., Rood R., 1994, *ARA&A*, 32, 191
- Woodall J., Agúndez M., Markwick-Kemper A. J., Millar T. J., 2007, *A&A*, 466, 1197
- Zernickel A., Schilke P., Smith R. J., 2013, *A&A*, 554, L2